EXPERIMENTAL AND COMPUTATIONAL ANALYSIS OF EVAPORATIVE SPRAY COOLING FOR GAS TURBINE EXHAUST EJECTORS

by

Nathon Begg

A thesis submitted to the Department of Mechanical and Materials Engineering

In conformity with the requirements for

the degree of Master of Applied Science

Queen's University

Kingston, Ontario, Canada

May, 2011

Abstract

This research studied the effects of evaporative spray cooling on air-air ejector performance. Experimental data was collected for the purpose of validating computational simulations. This was done by modifying an existing air-air ejector to accommodate four spray flow nozzles which were used to atomize cooling water. The only parameter that was varied throughout the study was the mass flow rate of cooling water. One single phase (air) case and four spray flow cases where performed and analyzed. The purpose of the single phase experiment was to have a baseline for the air-air ejector performance and isolate the sources of experimental error contributed by spray flow. Three specialized multiphase flow instruments were designed and fabricated by the author to measure, gas phase temperatures, spray mass flow rates, and mixture total pressures.

A computational study was performed using the collected experimental data for inlet continuous phase and spray mass flow as boundary conditions for equivalent simulations. A temperature gradient modified turbulence model was written by the author to better predict the mixing rates found experimentally which was used for the duration of this research. Secondary droplet breakup was modeled by the author using empirical correlations following preliminary simulations recognizing the deficiencies of commercially available breakup models.

Comparison of experimental and computational cases produced mixed results. It was found that the experimental gas temperature instrument performed poorly for the local droplet fluxes encountered during testing. The spray sampling probe showed more promising results with two integrated mass flows agreeing within 6% of computational simulations. The total pressure probe solved the issue of pressure port clogging, but measurements were representative of mixture density which made an inferred velocity calculation difficult. It was found that evaporation of spray flow before the nozzle exit plane caused a reduction in dynamic pressure and a reduction in back pressure.

A full scale simulation was performed to determine the effects of scaling on evaporative spray cooling performance. It was found that for the geometrically similar full scale model, the total droplet surface area and particle residence times scaled up with the model which increased cooling performance.

Acknowledgements

I would like to thank Dr. A.M. Birk for allowing me the opportunity to perform this research, and for his guidance, emphasis on critical thinking, and intellectual input.

I would like to thank my fiancé Sarah and my family for their ongoing support.

I would like to thank Queens University, W.R. Davis Engineering and the Natural Science and Engineering Research Council of Canada (NSERC) for jointly funding this research.

I would like to thank my colleagues in the Gas Turbine Laboratory for their help with experimental data collection, transportation, and brainstorming

I would like to thank Mr. James Crawford and Mr. David Poirier for the development of software used in the research.

Table of Contents

List of Figures

List of Tables

Nomenclature

A	Area
A_d	drag reference area
B	"B" factor
c_p	specific heat
C	coefficient
C_μ	turbulent viscosity model constant
D	diameter
D_v	thermal diffusivity
$f(M_\tau)$	mach number correction
F_D	force of drag
g	gravitational acceleration
h	enthalpy
h_L	latent heat of vaporization
k	thermal conductivity
k	turbulent kinetic energy
K	"K" factor
K	calibration coefficient
l	turbulent length scale
l_μ	viscosity length scale
L	hydraulic diameter
L	length
$\dot{m}$	mass flow rate
M	mass
n	Rossin-Rammler spread factor
N_{ob}	Obedience number
Nu	Nusselt number
Oh	Ohnesorge number
p	static pressure
Pr	Prandtl number
P_{total}	total pressure
q	dynamic pressure

r	radius
Re	Reynolds number
s´	fluctuating rate of deformation
S	mean rate of deformation
Sc	Schmidt number
Sh	Sherwood number
T	static temperature
T_g	non-dimensional temperature gradient
T_i	turbulence intensity
T_t	total temperature
u	x-wise velocity
u_i	flow field velocity vector
u´	x-wise fluctuating velocity
$\hat{u}$	internal energy
U	x-wise mean velocity
v	y-wise velocity
V	y-wise mean velocity
V	volume
V_0	limit volume
v´	y-wise fluctuating velocity
$\vec{v}$	velocity vector
w	z-wise velocity
W	z-wise mean velocity
w´	z-wise fluctuating velocity
x	x-wise distance
X	arbitrary variable
y	y-wise distance
y_w	wall distance
Y^+	non-dimensional wall distance
z	z-wise distance
Z	mass ratio

Greek Symbols

α	volume ratio
α	pitch
β	yaw
δ	Rossin-Rammler distribution mean
δ_{ij}	Kronecker delta
ε	turbulent dissipation rate
θ	temperature difference ratio
θ	cone
μ	dynamic viscosity
μ_t	turbulent viscosity
υ	kinematic viscosity
υ	turbulent velocity scale
ρ	density
σ	surface tension
τ	viscous stress
τ	shear stress
τ_v	momentum response time
τ_T	thermal response time
τ'	Reynolds stress
φ	roll
Φ	total pumping
Φ	mass flux
Φ	viscous dissipation function
ω	specific dissipation rate
ω	mass fraction

Subscripts

1	nozzle exit
2	secondary inlet
2Layer	viscous affected near wall region
3	mixing tube outlet
32	Sauter mean
∞	free stream
∞L	reference static pressure
%	percentile
Φ	total pumping
AR	arithmetic
AW	area weighted
bp	back pressure
BMI	bell mouth inlet
C	potential core at nozzle exit
CL	centerline upstream of nozzle
CFD	computational
d	discrete phase
D	drag
enh	enhanced wall treatment
EXP	experimental
f	frustum face
g	continuous phase
H20	water vapour
i	component
inj	injection
mM	mass median
MT	mixing tube
MW	mass weighted
n	nozzle
nM	number median
NE	nozzle exit

NI	nozzle inlet
N-MT	nozzle exit to mixing tube inlet
OL	reference total pressure
OT	outlet temperature
OTP	outlet total pressure
OV	outlet velocity
ref	reference
s	secondary
samp	sampling
S	spray
S	droplet surface
SV	secondary velocity
W	wall
WP	wall pressure
WT	wall temperature

Chapter 1

Introduction

In order to maximize efficiency, there is a requirement for gas turbine engines to operate at very high temperatures and pressures. This means that the exhaust plume temperatures can be in excess of 500ºC. For many applications it is desirable to cool this gas before it is issues from the exhaust system. Some benefits of exhaust gas cooling include: reduction of structural damage, reclamation of residual thermal energy for recuperation systems, and suppression of infrared signatures.

Ejectors are a commonly used device for this purpose due to their simple design and ease of incorporation into existing exhaust systems. A simple air-air ejector dissipates exhaust gas energy and momentum by mixing it with a passively entrained, secondary stream of ambient air. One hindrance of using air as a cooling fluid is that it has a relatively low thermal mass. This means that large secondary mass flows are required for effective cooling. In order to optimize the mixing of the two streams, one solution is to increase the interaction time by increasing the mixing length. For most applications, geometric constraints don't allow for this modification. Another solution is to increase the rate of mixing, but this generally results in total pressure loss due to flow obstruction. For gas turbine exhausts, this total pressure loss will increase the back pressure and reduce the power output which is undesirable.

When a stand alone air-air ejector system doesn't meet cooling requirements, a common solution is to incorporate evaporative spray cooling, which has several benefits. Changing waters state from liquid to vapour requires over 2000 times the amount of energy as raising the temperature of air 1K. The droplet's temperature is limited to its boiling point which keeps temperature differentials and heat transfer rates high. The process of atomizing water into droplets increases the surface area and broadens the cooled gas volume. For these reasons, relatively small mass flow rates of cooling fluid are required.

Another advantage to using water as a cooling fluid is that it is 1000 times denser than air. A pump's power requirement is proportional to its pressure differential; therefore a dense fluid requires less power to pump the same mass flow. This results in a relatively low parasitic loss for an auxiliary water pump.

The presented research is an investigation of air-air ejectors modified to incorporate spray nozzle for the purpose of evaporative cooling.

1.1 Objectives

The main objectives of this research were as follows:

- Develop a methodology for using modest RANS based computational fluid dynamics to simulate the evaporative spray cooling of air-air ejectors
- Validate computational simulations with experimental data
- Design, test, and validate cost effective multiphase flow instrumentation
- Quantify the benefits of evaporative spray cooling for gas turbine ejector cooling
- Determine the effects of scaling on evaporative spray cooling performance

1.2 Scope

The scope of this project was to collect experimental data for validation of computational simulations. An existing air-air ejector was modified to incorporate four commercially available spray nozzles. Only one ejector geometry, spray nozzle type, position and orientation were investigated in this research due to time constraints. The only varied parameter was the spray mass flow rate.

Experimental tests of this device were conducted at the Queens Hot Gas Wind Tunnel Laboratory on Grant Timmins Drive. Existing experimental instrumentation and software was used to measure gas phase properties. Three specialized instruments were designed and fabricated by the author to measure properties during spray flow testing.

The computational study was performed using the commercially available software packages Gambit 2.4.6 and Fluent 6.3.26. A combination of available physical models, analytical models, and user-defined functions were used to perform these simulations.

Chapter 2

Background and Literature Review

2.1 Ejectors

An ejector is a flow pump with no moving parts. It consists of a high momentum jet issuing from a nozzle, and a mixing tube as seen in Figure 2-1.

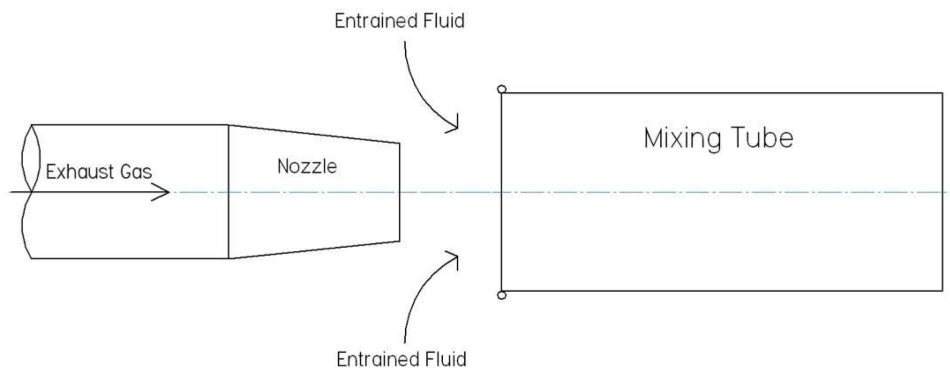

Figure 2-1 Ejector Assembly

The jet is mixed with the air in the mixing tube causing it to accelerate. Following Bernoulli's principal, this acceleration causes a static pressure drop at the entrance of the mixing tube which passively entrains the surrounding fluid. These two streams mix and reduce the average velocity and temperature of the jet which causes the static pressure to rise to atmospheric conditions at the mixing tube exit. In order for an ejector to work effectively, it requires that the flow in the nozzle be turbulent. This is because turbulent eddies increase the rate of mixing in the shear layer between the jet and the secondary flow. It was found in literature that above a Reynolds number of 2x10^4, the jet can be considered fully turbulent and the mixing rate no longer increases [1]. The downstream evolution of a turbulent jet can be seen in Figure 2-2.

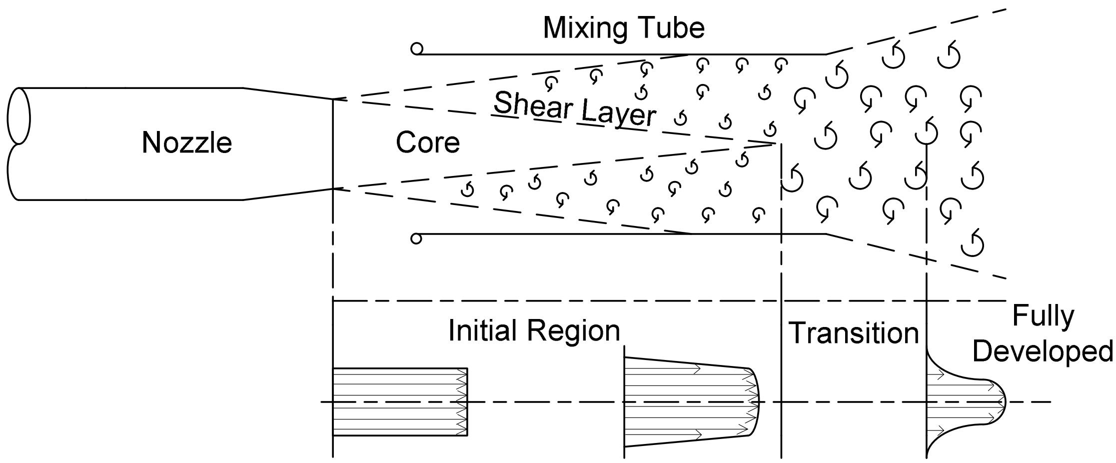

Figure 2-2 Jet Evolution

Turbulent jets are comprised of 3 regions: the initial, the transitional and the fully developed. In the initial region the flow consists of the potential core which is mostly unaffected by shear layer between it and the surrounding air. At some downstream position, the turbulent eddies in the shear layer will penetrate the jet and eliminate the core structure of the flow. The downstream flow from this point is eddy dominated and is known as the fully developed region. In the fully developed region the interface between the turbulent flow and the laminar secondary flow is called the intermittency surface.

Real ejectors encounter many complex flow features which make the prediction of their performance difficult. Laminar and transitional boundary layers generally occur in the passively entrained, unagitated secondary flow. Flow separation, reattachment and streamline curvature occurs as a result of pressure gradients. The rate of mixing in a shear layer is dependent on the magnitude of flow property gradients (more later). All of these factors must be properly resolved in order to accurately predict real ejector performance.

The introduction of spray flow further complicates the situation by adding evaporation, droplet mechanics, phase coupling, etc. (See Section 2.3). With a few assumptions, one can produce an ideal 1D analytical solution (Perfect Mixer Model) for an air-air ejector with spray flow for the control volume shown in Figure 2-3.

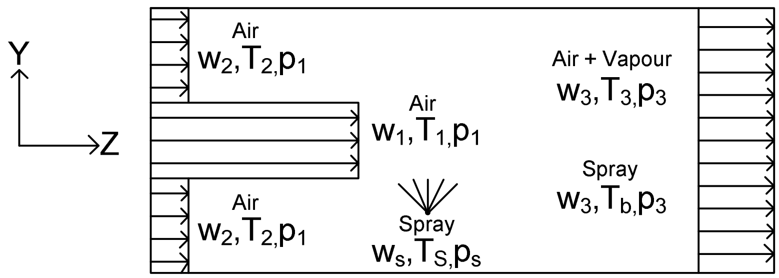

Figure 2-3 1D Ejector Control Volume

The following assumptions are required to produce this analytical solution. The radial pressure distribution at the nozzle exit / mixing tube inlet is uniform. This means that the streamlines of the secondary flow must be parallel to those of the jet. For real ejectors where the mixing tube is open to an atmospheric entrainment plenum, there will be streamline curvature at the entrance that will create a radial pressure gradient. The next assumption is that the secondary flow area is equal to the mixing tube area less the jet area. This assumption means that the perfect mixer model is invalid for ejectors where the exit plane of the flow nozzle is not coincident with the inlet plane of the mixing tube. There is an assumption made that the gas phase velocity and temperature profiles are uniform at the exit of the mixing tube. This assumption only applies if the mixing tube is infinitely long with no viscous loss. Finally, there is an assumption that the unevaporated spray flow mass crossing the mixing tube outlet plane is at its boiling temperature which eliminates the need to calculate droplet heating mechanics.

Following these assumptions, the analytical solution of an air-air ejector with spray flow is governed by conservation of mass, momentum and energy (See Equation 2-1 to Equation 2-3 respectively) [2].

$$\dot{m}_1 + \dot{m}_2 + \dot{m}_S = \dot{m}_3 \qquad \textbf{2-1}$$

$$p_1(A_1 + A_2) + \dot{m}_1 w_1 + \dot{m}_2 w_2 + \dot{m}_S w_S = p_3 A_3 + \dot{m}_3 w_3 \qquad \textbf{2-2}$$

$$\dot{m}_1\left(h_1 + \frac{w_1{}^2}{2000}\right) + \dot{m}_S\left(h_S + \frac{w_S{}^2}{2000}\right) + \dot{m}_2\left(h_2 + \frac{w_2{}^2}{2000}\right) = \dot{m}_3\left(h_3 + \frac{w_3{}^2}{2000}\right) \qquad \textbf{2-3}$$

Where: $\dot{m}$ = mass flow, p = static pressure, A = cross-sectional area, w = z-wise velocity, h = enthalpy, subscript 1 = nozzle exit, subscript 2 = secondary inlet, subscripts S = spray, subscripts 3 = mixing tube outlet.

The properties and the equations reduce to the gas phase solution when $\dot{m}_S$ goes to zero. In order to iteratively solve these codependent equations, a program was written by the author using Engineering Equation Solver (See Appendix B.9). The results of this perfect mixer program are displayed later in the results section.

2.2 Computational Fluid Dynamics

Computational fluid dynamics (CFD) is the numerical solution of governing fluid mechanics equations. The particular branch of CFD studied in this research is the finite volume method using the Navier-Stokes equations. The Navier-Stokes equations consist of a continuity equation (See Equation 2-4), a momentum equation (See Equation 2-5), and an energy equation (See Equation 2-6) [2].

$$\frac{\partial \rho}{\partial t} + \nabla(\rho u_i) = 0 \quad \textbf{2-4}$$

$$\rho \frac{du_i}{dt} = \rho g - \nabla p + \nabla \cdot \tau_{ij} \quad \textbf{2-5}$$

$$\rho \frac{d\hat{u}}{dt} + p(\nabla \cdot u_i) = \nabla \cdot (k \nabla T) + \Phi \quad \textbf{2-6}$$

Where: Divergence $\nabla \cdot = \left(\frac{\partial}{\partial x} + \frac{\partial}{\partial y} + \frac{\partial}{\partial z} \right)$

Gradient $\nabla = \left(\frac{\partial}{\partial x}, \frac{\partial}{\partial y}, \frac{\partial}{\partial z} \right)$

Viscous stress tensor $\tau_{ij} = \begin{bmatrix} \tau_{xx} & \tau_{yx} & \tau_{zx} \\ \tau_{xy} & \tau_{yy} & \tau_{zy} \\ \tau_{xz} & \tau_{yz} & \tau_{zz} \end{bmatrix}$

Total derivative $\frac{d}{dt} = \left(\frac{\partial}{\partial t} + u \frac{\partial}{\partial x} + v \frac{\partial}{\partial y} + w \frac{\partial}{\partial z} \right)$

Viscous-Dissipation Functions

$$\Phi = \mu \left[2\left(\frac{\partial u}{\partial x}\right)^2 + 2\left(\frac{\partial v}{\partial y}\right)^2 + 2\left(\frac{\partial w}{\partial z}\right)^2 + 2\left(\frac{\partial v}{\partial x} + \frac{\partial u}{\partial y}\right)^2 + 2\left(\frac{\partial w}{\partial y} + \frac{\partial v}{\partial z}\right)^2 + 2\left(\frac{\partial u}{\partial z} + \frac{\partial w}{\partial x}\right)^2 \right]$$

u_i = flow field velocity vector, g = acceleration of gravity, k = thermal conductivity, T = temperature, $\hat{u}$ = internal energy, u = x-wise velocity, v = y-wise velocity, w = z- wise velocity, and ρ = density, μ = dynamic viscosity.

In order to approximate these partial differential equations, the finite volume method divides the fluid domain into small volumes (also known as cells) that share their boundaries. The partial differential equations are then discretized into an algebraic form which can be applied to each finite volume. Because each volume shares its boundaries with neighbouring volumes, flux values through the fluid domain are conserved. Boundary conditions are used to close the algebraic equations for the volumes at the boundary of the fluid domain. These boundary conditions are constraints to which the conservation equations must be satisfied.

2.2.1 Turbulence Models

The Navier-Stokes transport equations used to describe fluid mechanics are applicable for both laminar and turbulent flows. Therefore, it is possible to directly solve turbulent flow problems but it can be costly and time consuming due to the number of equations solved per iteration. The direct solution of the Navier- Stokes equations is known as Direct Numerical Simulation (DNS). In order to simplify these problems, a turbulence model can be used to estimate turbulence quantities. A hierarchy of typical turbulence models is shown in Figure 2-4.

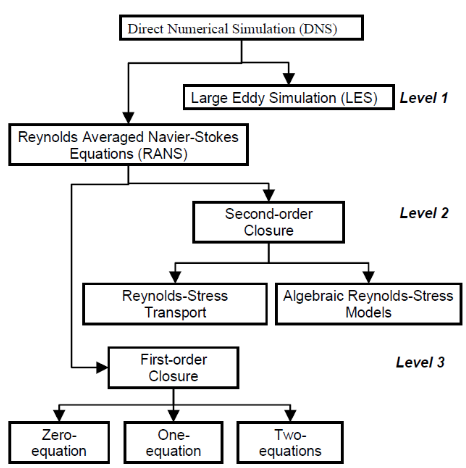

Figure 2-4 Turbulence Model Hierarchy [3]

Level 1 is divided into two groups, the first being Large Eddy Simulation (LES) and the other being Reynolds Average Navier Stokes (RANS). LES turbulence models directly solve the large scale turbulent eddies, which are the energy carrying structures. The dissipative smaller scale eddies are modeled using a simple sub-grid model. This model significantly reduces the computational cost from DNS, but is still more costly than RANS. LES requires a very fine, high quality mesh in order to produce meaningful results which may render it uneconomic for certain applications.

In this research, the objective was to determine a methodology for using RANS turbulence models. For turbulent flows, the flow variables u, v, w, and p can be represented by the sum of their mean and fluctuating components using Reynolds decomposition [4]. The form of each of these flow variables are as follows: u = U + u´, v = V + v´, w = W + w´, p = P + p´. By substituting these flow variables into the momentum equation, products of fluctuating components are encountered. By time averaging, the mean of a fluctuating component is equal to zero, but this is not the case for the product of fluctuating components. This dilemma results in six fluctuating viscous stress terms known as Reynolds stresses in the form of three normal stresses, $\tau'_{xx} = -\rho\overline{u'^2}$, $\tau'_{yy} = -\rho\overline{v'^2}$, $\tau'_{zz} = -\rho\overline{w'^2}$ and three shear stresses, $\tau'_{xy-yx} = -\rho\overline{u'v'}$, $\tau'_{xz-zx} = -\rho\overline{u'w'}$, $\tau'_{yz-zy} = -\rho\overline{v'w'}$. Since RANS turbulence models are time averaged there is a requirement for the estimation of these fluctuating components using mean flow field quantities. The RANS group of turbulence models is divided into two subgroups, second order closure and first order closure. Second order closure models calculate each Reynolds stress individually and therefore are more computationally expensive. Two common second order closure models are the Algebraic Stress Model (ASM) and the Reynolds Stress Model (RSM). For the purpose of this research, second order closure models were not investigated and their derivation will not be discussed for brevity. First order closure models make the assumption that all Reynolds stresses are proportional to the mean rates of deformation [4]. This assumption is known as the Boussinesq hypothesis where the calculation of the Reynolds stress is shown in Equation 2-7 [4].

$$\tau_{ij} = \mu_t\left(\frac{\partial U_i}{\partial x_j} + \frac{\partial U_j}{\partial x_i}\right) - \frac{2}{3}\rho k \delta_{ij} \qquad \textbf{2-7}$$

Where: turbulent kinetic energy $k = \frac{1}{2}\left(\overline{u'^2} + \overline{v'^2} + \overline{w'^2}\right)$, U is the mean velocity component, μ_t = turbulent viscosity, δ_{ij} = Kronecker delta. The Kronecker delta is used so that the same equation applies for the Reynolds shear stresses as the Reynolds normal stresses.

The two equation RANS turbulence models (See Figure 2-4) were of particular interest in this research due to their widely accepted use and validity [4]. These two equation models include the k-ε and k-ω subgroups. For these models the turbulent viscosity seen in Equation 2-7 is defined in Equation 2-8 [4].

$$\mu_t = C_\mu \rho \nu l \qquad \textbf{2-8}$$

Where: C_μ is a model constant, υ is the turbulent velocity scale, l is the turbulent length scale

All two equation models use the Boussinesq hypothesis and a turbulent viscosity term, but the derivation of their turbulence scales differs. For the k-ε subgroup the turbulent velocity scale and length scale are calculated using Equation 2-9 and Equation 2-10 respectively [4].

$$\nu = k^{1/2} \qquad \textbf{2-9}$$

$$l = \frac{k^{3/2}}{\varepsilon} \qquad \textbf{2-10}$$

Where: turbulent dissipation rate $\varepsilon = 2\mu\rho\overline{s'_{ij} \cdot s'_{ij}}$, fluctuating rate of deformation $s'_{ij} = \frac{1}{2}\left(\frac{\partial u'_i}{\partial x_j} + \frac{\partial u'_j}{\partial x_i}\right)$

By substituting Equation 2-9 and Equation 2-10 into Equation 2-8 the turbulent viscosity for the k-ε subgroup is calculated using Equation 2-11 [4].

$$\mu_t = \rho C_\mu \frac{k^2}{\varepsilon} \qquad \textbf{2-11}$$

Both turbulent kinetic energy and turbulent dissipation have their own transport equations and their boundary conditions are described as follows: $k = \frac{2}{3}\left(U_{ref} T_i\right)^2$, $\varepsilon = C_\mu{}^{3/4} \frac{k^{3/2}}{l}$, $l = 0.07L$, U_{ref} = reference velocity, T_i = turbulence intensity, L = hydraulic diameter.

For the k-ω subgroup, the turbulent velocity scale is described by specific dissipation (ω) and the calculation of the specific dissipation and turbulent length scale are shown in Equation 2-12 and Equation 2-13 respectively [4].

$$\omega = \frac{\varepsilon}{k} \qquad \textbf{2-12}$$

$$l = \frac{k^{1/2}}{\omega} \qquad \textbf{2-13}$$

By substituting Equation 2-12 and Equation 2-13 into Equation 2-8 the turbulent viscosity for the k-ω subgroup is calculated using Equation 2-14 [4].

$$\mu_t = \rho \frac{k}{\omega} \qquad \textbf{2-14}$$

At the boundaries, k and ω must be specified which becomes problematic in the free stream where k→0 and ω→0 because the turbulent viscosity is highly sensitive to these specified values [4]. This occurrence tends to make the model more dependent on the boundary definitions than the k-ε group. Some variations of the two equation turbulence models have been designed to better describe flows with high strain rates, swirl, pressure gradients, etc. These include the Renormalized Group (RNG) k-ε, Realizable k-ε, and k-ω Shear Stress Transport (SST) models.

The Standard k-ε model is the most widely used and validated turbulence model in current use. It has proven to be applicable for a wide range of confined flows, and flows with thin shear layers which are commonly found in industry [4]. The model has been found to poorly predict flows with larger strain rates, swirl, rotation, etc. For flows with large adverse pressure gradients, the Standard k-ε model over predicts turbulent shear stresses which suppresses flow separation.

The RNG k-ε model uses a modified model constant to account for the effects of local strain rate in the transport equation for the turbulent dissipation. This model has proven to be an improvement for modeling flows with large strain rates and pressure gradients.

The Realizable k-ε model uses a different formulation for the turbulent viscosity and the transport equation for turbulent dissipation. This model mathematically satisfies certain constraints on the Reynolds stresses which the Standard k-ε and RNG k-ε do not [5]. This model improves the prediction of spreading rates in round and planar jets, flows with large pressure gradients, separation, reattachment, and swirl.

The k-ω model is most commonly used in the aerospace industry for predicting the external flow around objects with complex geometries. This model has shown close agreement with experimental data when predicting the free shear flow spreading rates of far wakes, mixing layers, and jets [5].

The k-ω model SST model uses both the k-ω and k-ε models to calculate turbulence quantities. The k-ω formulation is used close to solid boundaries and the k-ε formulation is used in the free stream [6]. A blending function is used in order to smoothly transition between the two. This model has proven to have a more general applicability than the standard k-ω model and provides better predictions of boundary layers with zero pressure gradients and adverse pressure gradients [4].

It has been found through comparison of experimental and computational results that two equation turbulence models under predict the mixing rate of non-isothermal shear layers [7], [8], [9]. This is because large temperature or pressure gradients have significant effects on turbulence quantities. In experiments, it was observed that density gradients gave rise to flow instability due to the rapid rates of local flow acceleration. Abdol-Hamid et al. [7] proposed that this C_μ term in the turbulent viscosity equation could be empirically modified to better describe the decay of non-isothermal jets. This modification is shown in Equation 2-15 [7].

$$C_\mu = 0.09\left[1 + \frac{T_g{}^3}{0.041 + f(M_\tau)}\right] \qquad \textbf{2-15}$$

Where: T_g = non-dimensional term that describes the temperature gradient, normalized by the turbulent length scale as shown in Equation 2-16 [7]. The term $f(M_\tau)$ = correction for Mach number, but is set to zero for incompressible flow.

$$T_g = \frac{\nabla(T_t)\left(\frac{k^{2/3}}{\varepsilon}\right)}{T_t} \qquad \textbf{2-16}$$

Where: T_t = total temperature

The fact that the temperature correction term is proportional to the gradient of temperature means that the turbulence model will revert to its standard calculation of turbulent viscosity anywhere that the flow is isothermal.

2.2.2 Near Wall Treatment

Turbulence models are only applicable for core flows that are a sufficient distance from a wall boundary. The presence of the wall has major effects on the flow variables and turbulent quantities. For these reasons, a near wall treatment is required to accompany turbulence models. There are three wall treatment types in Fluent 6.3.26: standard wall functions, non-equilibrium wall functions, and enhanced wall treatment. Standard wall functions employ empirical boundary layer profiles to wall adjacent cells which are representative of turbulent boundary layers. This allows the flow variables and turbulent quantities to be calculated without a turbulence model. The production of turbulent kinetic energy and its dissipation rate are calculated on the basis of a local equilibrium for wall adjacent cells [5]. Standard wall functions apply well to high Reynolds number, simple flows like flat plate flow, pipe flow etc. These are the flows that satisfy the equilibrium assumptions made by the standard wall functions. As the flow deviates from these ideal situations variations on the near wall model are required. The non – equilibrium wall function is an improvement in the standard wall function. The improvements are that the velocity gradient is sensitized for pressure gradients (assumption $\delta P/\delta y = 0$ for standard wall functions) and a two layer concept is used to determine the turbulent kinetic energy, production and dissipation for the wall adjacent cells [5]. This model improves the results of wall bounded flows that vary from the fully turbulent boundary layer assumptions used in the standard wall function. In order to use standard or non-equilibrium wall functions the first cell center in the boundary layer mesh must have a Y^+ value between 30 and 300 (See Equation 2-17) [10].

$$Y^+ = \frac{y_w\sqrt{\frac{\tau_w}{\rho}}}{\nu} \qquad \textbf{2-17}$$

Where: y_w = distance from wall, τ_w = wall shear stress, v = kinematic viscosity

This is because the wall function employs empirical fits assuming that the cell is in the Log-Law Layer (See Figure 2-5).

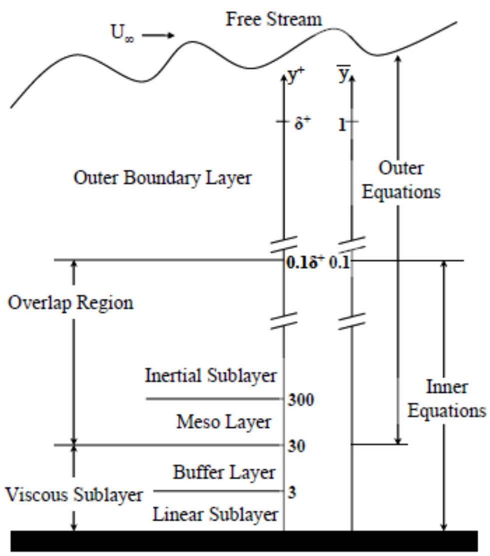

Figure 2-5 Near Wall Sub-Regions [11]

Special care should be taken to ensure that these cells do not fall in the buffer layer (Y^+ 5-30) because the empirical fits don't apply to this region [10]. The enhanced wall treatment fully resolves the viscous affected region of the turbulent boundary layer using a two-layer model. The two layer model divides the fluid domain into a fully turbulent region and a viscous affected region. The core flow turbulence model is used in the fully turbulent region and a one equation model is used of the inner region. The two regions are then blended to ensure a smooth profile. In regions where the grid isn't sufficiently resolved the enhanced wall treatment reverts to a near wall function that combines a turbulent (log-law) and laminar (Linear) profile which are combined using a blending function. This allows the user to only refine the boundary layers that require the two-layer model. In order to use enhanced wall functions the first cell in the boundary layer must be within the viscous sub-layer ($Y^+ < 5$) for the two-layer model to work. Once again, special care should be taken to ensure that the cell isn't within the buffer region. Coarse boundary layers should be in the log-law layer so that the model reverts to its enhanced wall functions which are applicable in that region (See Figure 2-5). Salim et al. [10] found that standard wall functions outperform enhanced wall treatment in predicting the velocity profile and wall shear stress for a high Re flow over a flat plate while using 71% less cells. Molochnikov et al. [12] found that the best prediction of wall shear stress in the separated region behind a rib placed normal to a wall in cross-flow was produced by the RNG k-ε turbulence model coupled with enhanced wall treatment. Most other models drastically over predicted the shear stress in the recirculation and reattached zones. Fluent Inc. [13] found that using enhanced wall treatment resulted in good agreement with experimental data in predicting the pressure coefficient distribution around a cylinder in cross-flow for Reynolds numbers ranging from $1\text{-}1\times10^6$. This study is of particular interest because pressure coefficient distributions around a cylinder for this range of Reynolds numbers rely heavily on the predicted location of flow separation. Kim et al. [14] found that using kε turbulence models with enhanced wall treatment they were able to make very good numerical predictions of the radial velocity distribution for multiple sets of experimental data for an impinging jet. Impinging jets are a good measure of a wall function's ability to model the boundary layer development in the vicinity of impingement. Soh et al. [15] compared the results of standard wall functions and enhanced wall treatment in predicting the velocity profile in a rotating pipe flow. This is a flow that encounters a radial pressure gradient and the velocity profile prediction was greatly improved with the use of enhanced wall treatment.

2.3 Multiphase Flow

Multiphase flow is defined as a flow containing components of different phases (e.g. solid, liquid, and gas). It is important to note that flows containing only one component (e.g. steam and water droplets) can be multiphase while mixtures of multiple components (e.g. air) can be considered single-phase. Multiphase flows can be separated into four categories as shown in Table 2-1.

Table 2-1 Multiphase Flow Types [16]

Multiphase Flows	
Gas-Liquid Flows	Bubbly Flows Separated Flows Gas-Droplet Flows
Gas-Solid Flows	Gas-Particle Flows Pneumatic Transport Fluidized Beds
Liquid-Solid Flows	Slurry Flows Hydrotransport Sediment transport
Three-Phase Flows	Bubbles in Slurry Flow Droplets/Particles in Gaseous Flows

Multiphase flows consist of discrete phases and a continuous phase. The distinction between the two is that one can’t move between discrete phase elements without passing through the continuous phase which is not true vice-versa [16]. Since these flows consist of multiple components with their own unique properties, it’s important to define properties that are specific to the mixture. These properties include: mixture density (See Equation 2-18), component density (See Equation 2-19), discrete phase volume fraction (See Equation 2-20), continuous phase volume fraction (See Equation 2-21), and mass ratio (See Equation 2-22) [16].

$$\rho_{mix} = \lim_{V \to V_0} \frac{\partial m}{\partial V} \tag{2-18}$$

$$\rho_i = \lim_{V \to V_0} \frac{\partial m_i}{\partial V} \quad \textbf{2-19}$$

$$\alpha_d = \lim_{V \to V_0} \frac{\partial V_d}{\partial V} \quad \textbf{2-20}$$

$$\alpha_c = 1 - \alpha_d \quad \textbf{2-21}$$

$$Z = \frac{m_d}{m_g} \quad \textbf{2-22}$$

Where: V_0 = limit for which the mixture density doesn't significantly vary with small changes in volume; m = total mass of all mixture components, V = mixture volume, m_i = component mass, V_d = discrete phase volume, m_d = discrete phase mass, m_g = continuous phase mass

In multiphase flow, the spacing between particles has a significant effect on their mechanics (I.E. mass, momentum, heat transfer). For dilute flows where the spacing in relatively large, the particle mechanics are governed by interaction with the continuous phase, while with relatively dense flows, the particle mechanics are strongly governed by interaction between neighbouring particles [16]. If gravity is neglected, and the flow is considered dilute enough for a particle to be considered isolated ($\alpha_d < 10\%$) then its motion is described by Equation 2-23 and a function of the relative Reynolds number (See Equation 2-24), the momentum response time (See Equation 2-25), and the drag coefficient (See Equation 2-26) [16].

$$\frac{\partial \vec{v}_d}{\partial t} = \frac{1}{\tau_v} \frac{C_D \operatorname{Re}_r}{24} \left| \vec{v}_g - \vec{v}_d \right| \quad \textbf{2-23}$$

$$\operatorname{Re}_r = \frac{\rho_g D_d \left| \vec{v}_g - \vec{v}_d \right|}{\mu_g} \quad \textbf{2-24}$$

$$\tau_v = \frac{\rho_d D_d^{\ 2}}{18\mu_g} \quad \textbf{2-25}$$

$$C_D = \frac{F_D}{\frac{1}{2}\rho_g \left|\vec{v}_g - \vec{v}_d\right|^2 A_d} \quad \textbf{2-26}$$

Where: $\vec{v}_d$ = discrete phase velocity vector, $\vec{v}_g$ = continuous phase velocity vector, ρ_g = continuous phase density, D_d = discrete phase diameter, μ_g = continuous phase dynamic viscosity, ρ_d = discrete phase density, F_D = drag force, A_d = drag reference area

The momentum response time (τ_v) is a measure of a particles response to applied aerodynamic forces from the continuous phase (drag and lift). It can be thought of as the ratio of particle mass to continuous phase viscous forces.

2.3.1 Droplet Drag

When a liquid particle is subjected to aerodynamic forces, its spherical shape is deformed. Depending on the orientation of the deformation, this can act to increase or decrease the drag coefficient. If particles are considered spherical, the coefficient of drag is highly dependent on the relative Reynolds number (See Figure 2-6).

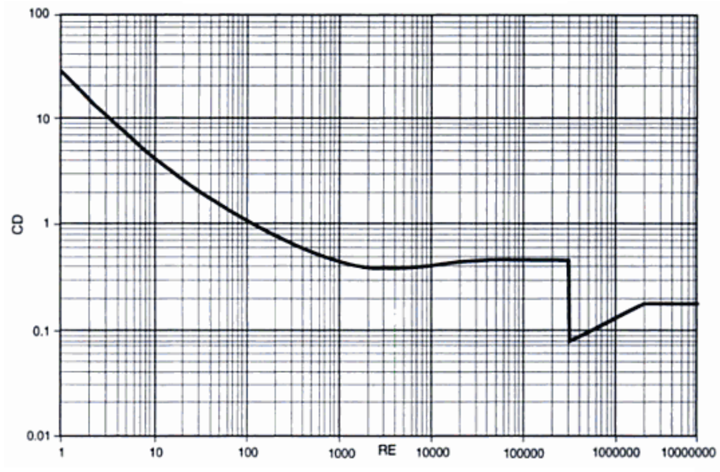

Figure 2-6 Spherical Drag Coefficient [17]

For most of the defined range, the separation line occurs approximately 80° from the stagnation point. Since the force of drag is largely a result of the pressure distribution around the sphere and not viscous forces, the drag coefficient can be approximated as 0.45, and varies only 13% over the range. This regime of drag for a spherical particle is known as the Newton's drag law regime [16]. For large relative Reynolds numbers ($Re_r > 2x10^5$) the boundary layer becomes turbulent before the separation point which mixes the free stream momentum closer to the wall. This increase in momentum allows the boundary layer to stay attached when subjected to larger adverse pressure gradients and moves the separation point back to approximately 120° from the stagnation point. This seemingly instantaneous change in separation point drastically reduces the form drag on the sphere and is commonly referred to as the "drag crisis" regime [16].

2.3.2 Droplet Breakup

For liquid multiphase particles, aerodynamic forces can lead to deformation and breakup. Two common variables are used to determine the mechanics of particle breakup. These variables are known as the Weber number and the Ohnesorge number (See Equation 2-27 & Equation 2-28 respectively) [18].

$$We = \frac{\rho_g D_d \left| \vec{v}_g - \vec{v}_d \right|^2}{\sigma_d} \quad \textbf{2-27}$$

$$Oh = \frac{\mu_d}{\sqrt{\rho_d D_d \sigma_d}} \quad \textbf{2-28}$$

Where: σ_d = droplet surface tension

The significance of the Weber number is that it can be thought of as the ratio of aerodynamic forces to surface tension forces. The significance of the Ohnesorge number is that it can be thought of as the ratio of droplet viscous forces to surface tension forces. The Weber number at which breakup first occurs is commonly known as the critical Weber Number (We_c). Many researchers have tried to determine the value of the critical Weber number experimentally with mixed results which are summarized in Table 2-2.

Table 2-2 Critical Droplet Weber Number

Author	We_c
Hsaio [19]	8
Belen'ki. [20]	10
Krzeczkowski [21]	10
Wierzba, 1985 [22]	14
Pilch, 1987 [18]	$12(1+1.077 \cdot Oh^{1.6})$

The reality is that the critical Weber number is also a function of the droplet Ohnesorge number which accounts for the droplet viscous forces. Once the particle has reached or exceeded the critical Weber Number, there are multiple breakup regimes which it can encounter. These breakup regimes are shown in Figure 2-7.

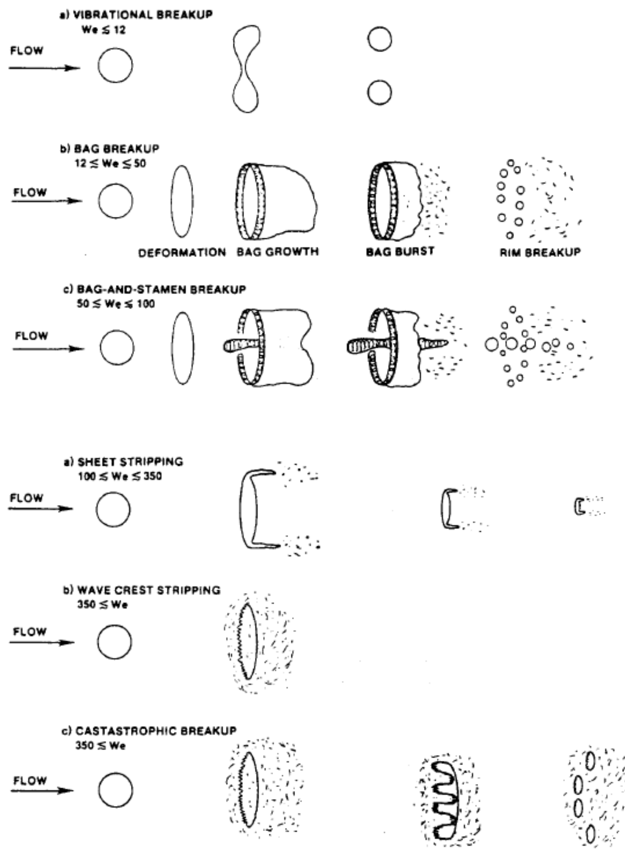

Figure 2-7 Particle Breakup Regimes [18]

When the Weber number is close to its critical value, breakup is said to be occurring in the vibrational regime [18]. As the magnitude of the aerodynamic force increases, the droplet begins to oscillate at its natural frequency. These forces act as constructive interference to increase the amplitude of particle surface oscillations until breakup occurs. In this regime, droplet breakup times are relatively slow and produce only a few child droplets upon breakup. As the Weber number is increased up to 50, the droplet transitions into the bag breakup regime [18]. In this regime, deformation at the stagnation point of the particle (point on particle face normal to the relative velocity vector) flattens the particle. This deformation exceeds the particle center point and begins to inversely deform causing the formation of a “bag”. This continues until the surface tension can no longer retain its structure and the bag bursts. This type of breakup can produce upwards of 25 smaller child droplets. As the Weber Number is increased up to 100, a central column forms at the stagnation point just before breakup occurs. This breakup regime is known as the bag and stamen regime [18]. A fundamental change in breakup kinematics occurs as the Weber Number is increased past a value of 100. The flattening seen in the bag breakup regime still occurs, but before the inverse deformation, the aerodynamic forces become so high that small droplets are stripped off of the perimeter. There are three breakup regimes that occur at these high Weber numbers, these include: Sheet stripping, Wave crest stripping, and Catastrophic breakup [18]. These regimes are very similar, but are distinguished by an increasing level of instability in the flattened particle.

After the initial breakup occurs, the child particles may still have Weber numbers that exceed the critical value. This means that the particles will continue to break up until a maximum stable diameter is reached. After each level of breakup, the relative velocity between child particles and the continuous phase will differ from that of the parent particle. For this reason it’s difficult to determine a maximum stable diameter based only on the parent droplet properties. A significant amount of research has gone into producing correlations for the Sauter Mean Diameter (droplet distribution volume divided by surface area), maximum stable diameter, and other distribution characteristics [23], [24], [26] with the later being used in Section 4.4.3.

There are two breakup models available with Fluent 6.3.26, these include: the Taylor Analogy Breakup (TAB) Model and the WAVE breakup model. The TAB model, which was derived by

Taylor [25] uses the analogy that the particle is a spring mass system where the externally applied force is the aerodynamic forces, the spring force is the surface tension, and the damping force is the droplet viscosity. This system oscillates until a critical limit is met and the particle breaks up into a number of child droplets that is defined by the user (Fluent default = 2). This model works very well for the vibrational breakup regime but loses applicability at higher Weber numbers. The WAVE breakup model was produced by Reitz [27] and models the unstable wave formation on the surface of a round liquid jet. As the magnitude of these waves increase, particles are shed from the jet surface. This model was designed to capture the breakup phenomenon occurring at Weber numbers higher than that of the sheet stripping regime (We>100).

2.3.3 Droplet Evaporation

Droplet evaporation / condensation are driven by a temperature difference between the droplet and continuous phase. The energy balance for a droplet control volume is described by a modified lumped capacitance equation (See Equation 2-29), and a function of the thermal time constant (See Equation 2-30), Nusselt number (See Equation 2-31), Sherwood number (See Equation 2-32), Schmidt number (See Equation 2-33), and Prandtl Number (See Equation 2-34) [16].

$$\frac{dT_d}{dt} = \frac{Nu}{2\tau_T}(T_g - T_d) + \frac{Sh\rho_g \pi D_d D_v (\omega_{H2O,\infty} - \omega_{H2O,S})h_L}{\left(c_{p,d}\rho_d \pi D_d{}^2\right)/6} \qquad \textbf{2-29}$$

$$\tau_T = \frac{\rho_d c_{p,d} D_d{}^2}{12 k_d} \qquad \textbf{2-30}$$

$$Nu = 2 + 0.6\,\mathrm{Re}^{1/2}\,\mathrm{Pr}^{1/3} \qquad \textbf{2-31}$$

$$Sh = 2 + 0.6\,\mathrm{Re}^{1/2}\,Sc^{1/3} \qquad \textbf{2-32}$$

$$Sc = \frac{\nu_g}{D_v} \qquad \textbf{2-33}$$

$$\mathrm{Pr} = \frac{c_{p,g}\mu_g}{k_g} \qquad \textbf{2-34}$$

Where: T_d = droplet temperature, T_g = continuous phase temperature, D_v = thermal diffusivity, $\omega_{H2O,\infty}$ = water vapour mass fraction of free stream, $\omega_{H2O,S}$ = water vapour mass fraction at droplet surface, h_L = latent heat of vaporization, $c_{p,d}$ = droplet specific heat, $c_{p,g}$ = continuous phase specific heat, k_d = droplet thermal conductivity, k_g = continuous phase thermal conductivity

To the right of the equals sign in the Equation 2-29, the left term represents the heat transferred into the control volume, and the right term represents the heat carried out of the system through water vapour mass transfer. The energy balance for the droplet control volume is shown in Figure 2-8.

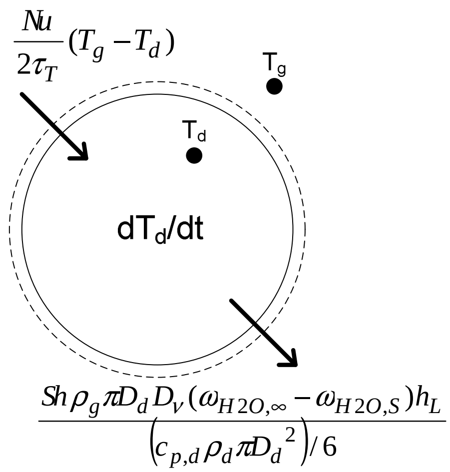

Figure 2-8 Evaporating Droplet Energy Balance

As the temperature of the droplet increases, the temperature differential between it and the continuous phase decreases, causing the heat transfer into the control volume to decrease. Conversely, a rise in droplet temperature raises the water vapour mass fraction at the surface of the droplet ($\omega_{H20,S}$) which increases the energy transfer out of the control volume. If dT_d/dt is set to zero (steady state) one can solve for the temperature at which the droplet will evaporate. This temperature is known as the pseudo wet-bulb temperature [28], [16]. If the temperature differential is large enough, this equilibrium temperature is never met and the droplet temperature will rise to its boiling point. At this point the mass transfer is no longer driven by the gradient in water vapor, but rather, by the water vapour pressure exceeding the free stream pressure. Upon boiling, the temperature of the droplet surface remains at the boiling point. It has been found in literature [29] that there can be significant temperature gradients inside the droplet because only a small film on its surface is exchanging heat with the continuous phase. This means that most of the energy transferred into the droplet is used for evaporation and not to internal heating. Furthermore, the evaporation process helps to cool the liquid at the center of the droplet.

The model used by Fluent 6.3.26 is a simplified model that doesn't account for droplet temperature gradients. Rather, it considers the entire droplet to be at the boiling point. Since the ratio of specific heat to the latent heat is fairly small for water, this assumption is thought to have negligible effects on the continuous phase solution.

2.3.4 Size Distributions

Two commonly used size distributions that are used for multiphase flows are the log-normal distribution and the Rossin-Rammler distribution. The log-normal distribution is a modified Gaussian distribution that is governed by the number frequency distribution shown in Equation 2-35 [16].

$$F(D_d) = \frac{1}{\sqrt{2\pi \ln \frac{D_{m,84\%}}{D_M}}} \exp\left[-\frac{1}{2} \left(\frac{\ln D_d - \ln D_{nM}}{\ln \frac{D_{m,84\%}}{D_M}} \right)^2 \right] \frac{1}{D_d} \qquad \textbf{2-35}$$

The way in which this distribution deviates from a normal Gaussian distribution is that it isn't symmetrical about the mean value. The log-normal distribution is biased towards the lower tail. This distribution has shown the most applicability in correlating the size distribution of solid particles.

The Rossin-Rammler distribution is typically used for correlating the droplet sizes for spray flow applications. The distribution is expressed as a cumulative mass distribution by Equation 2-36 [30].

$$F(D_d) = \exp\left[-\left(\frac{D_d}{\delta}\right)^n\right] \quad \textbf{2-36}$$

Where n and δ are the spread factor (See Equation 2-37) and distribution mean respectively.

$$\delta = \frac{D_{mM}}{0.693^{\frac{1}{n}}} \quad \textbf{2-37}$$

There are a few statistical parameters that are used to describe these distributions of particles. These include: Mass Median Diameter (D_{mM}), Number Median Diameter (D_{nM}), Sauter Mean Diameter (D_{32}), and Percentile Diameter ($D_{\%}$). The Mass Median Diameter is the diameter at which half of the total distribution mass is particles of smaller and larger diameter. The Number Median Diameter is the diameter at which the half the total number of particles are of smaller and larger diameters. The Sauter Mean Diameter is calculated as the total volume of the distribution particles divided by the total surface area. This statistical parameter is of particular interest in research where the surface area of particles directly affects their mechanics (I.E. evaporating spray flow). The percentile diameter can be used to describe the diameter at which a certain number, or mass percentage, is of a smaller diameter. For example, in Equation 2-35, the variable $D_{m,84\%}$ is the diameter at which 84% of the total distribution mass is of a smaller diameter.

2.4 Instrumentation

This section reviews the literature pertaining to the multiphase flow measurements performed in this research.

2.4.1 Gas Temperature Measurement

One instrument used for multiphase temperature measurement is a thermo needle probe [31], [32]. These probes incorporate a micro thermocouple in a ceramic sheath (~150 μm diameter) which can be used to measure the temperature of both liquid and gas phases (See Figure 2-9).

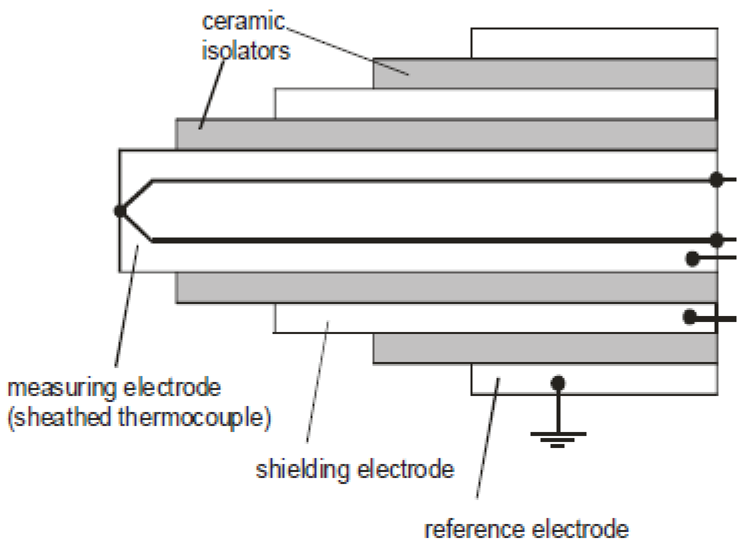

Figure 2-9 Thermo Needle Probe [32]

The drawback is that these probes are limited by their response time and require relatively large inter-phase residence times to obtain accurate phase temperature segregation (~0.5s). The applicability of these probes is generally limited to slow moving multiphase flows such as bubbling, slurry flow, and settling flow. Wang et al. [33] and Buchanan [34] both proposed an analytical model to calculate gas phase temperatures from an unshielded thermocouple in dilute multiphase flow. They agree that a time average measurement will be representative of a phase average temperature. These models require a discrete phase mass flux in order to calculate a contact probability with the thermocouple. Knowing the contact probability, and temperature of the discrete phase (pseudo wet-bulb temperature), one can use the lumped capacitance method to infer a gas temperature from the phase averaged measurement. These models showed promising results in measuring general temperature trends in the flow, but due to the error associated with the analytical models (estimated heat transfer coefficients, discrete phase mass flux, etc.) there was large errors in the actual gas temperature measurements. Another problem with this type of model is that it requires a very dilute discrete phase. This is because if the contact probability is too high the discrete phase temperature will saturate the measurement. Wang et al. [35] and Li et al. [36] designed probes that separate the phases before a temperature measurement is taken, very similar to the probe used in this research (See Section 3.9). They used a thermocouple placed behind an adiabatic shield, with a fine copper screen to filter any recirculating discrete phase (See Figure 2-10).

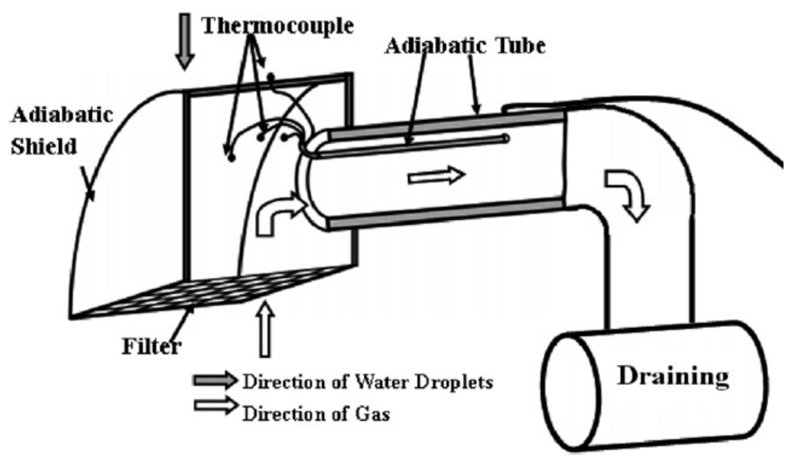

Figure 2-10 Shielded Temperature Probe [36]

Both sources describe the design challenges for these probes which include: screen size selection, increased residence time, and response time. The selection of screen size can have a large effect on the gas temperature measurement. If the mesh is too coarse, the small droplets will recirculate around the obstruction with the continuous phase through the mesh and contact the thermocouple, giving an erroneous measurement. If the mesh is too fine, the recirculating droplets will build up, evaporate, and cool the gas, giving an erroneous measurement. The introduction of a separating shield increases the interaction time between phases. This means that the measured gas temperature is more representative of a downstream measurement than the desired local measurement. Depending on the refresh rate of the gas phase passing through the filter, the probe may require a long settling time when moved to a new location to reach steady state. Failure to provide this settling time will give rise to transient error between measured points. These types of gas temperature probes are generally used in low temperature differential flows in order to determine psychrometric properties [35].

2.4.2 Droplet Flux Measurement

The measurement of droplet spray characteristics (diameter, velocity, local flux, etc) can be separated into two categories, non-intrusive and intrusive. Non-intrusive methods include: Laser Doppler Anemometry (LDA) in which the frequency of scattered radiation is compared to monochromatic radiation source. The attenuation of radiation is known as the Doppler shift and is a function of the object velocity and geometry. From this data droplet diameter and velocity vector can be inferred [37]. Particle Image Velocimetry (PIV) in which the particles are illuminated twice in quick succession with a laser sheet source. During these illuminations, two simultaneous images are taken of the particles. In order to obtain accurate measurements of droplet diameter, the image must be taken of a very small region of the flow known as the interrogation zone (generally only a few square centimeters [38]). If the time between the successive images is known then the in-plane velocities can be inferred. In order to calculate three dimensional velocity vectors, there is a requirement for two images from different angles (stereo PIV) [38]. The drawbacks of these methods are that they require: optical access to the flow field, selective illumination, small interrogation areas, and costly apparatus. For these reasons, many efforts have been made to expand the accuracy and applicability of intrusive mechanical sampling instrumentation. One method of lowering the intrusive nature of the probe is to create an isokinetic sampling environment which requires equilibrium of static pressure between the free stream and the probe sampling tube. This condition is very important for applications where the probe is being used to sample combustion gas with very small droplets to determine constituent concentrations [39], [40]. An isokinetic environment ensures that the sampling rate is unaffected by the presence of the probe. If the sampling environment is anisokinetic (static pressure differs from the free stream), there will be an error associated with very small droplets diverting or being sucked into the sampling area. However, if the pressure differential is fairly small and the probe sampling area has a sharp leading edge, the streamline curvature will occur very close to the probe tip. This means that for high inertia particles, the trajectories will be unchanged and the anisokinetic condition will induce negligible error [41]. Dussourd et al. [42] proposed a dimensionless variable called the Obedience number to describe the collection efficiency of mechanical sampling probes in liquid gas flows (See Equation 2-38).

$$N_{ob} = \frac{3\rho_g D_{samp}}{4\rho_d D_d} \qquad \textbf{2-38}$$

$$\mathrm{Re}_d = \frac{\rho_g D_d \vec{v}_d}{\mu_g} \qquad \textbf{2-39}$$

Where: D_{samp} = sampling tube diameter

For an Obedience number less than 0.1 and a droplet Reynolds number (See Equation 2-39) greater than 100, the collection efficiency is generally very high (>99% [42]). Mizutani et al. [43] used a water cooled sampling probe for measuring droplet flux values in a combustion flame. In fact, the probe geometry and sampling procedure were very similar to those used in this study.

The combustion gas and discrete phase were sampled together and separated in the collection area. Although this author didn't perform an error analysis of their collection process, contours of particle flux from a burning and non-burning case were presented in their results (See Figure 2-11)

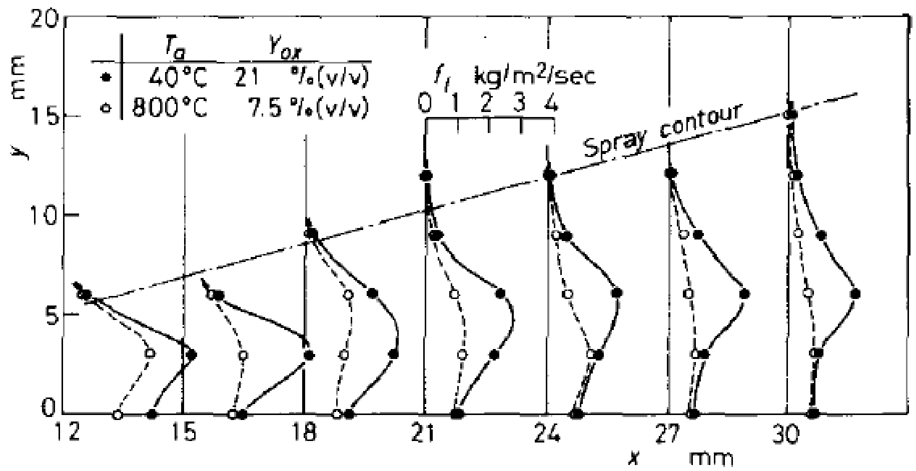

Figure 2-11 Radial Particle Flux Contour [43]

Lee et al. [44] performed traverses of a premixed flat flame burner with a water cooled sampling probe to measure local mass flux values of falling n-octane droplets. In their results, they reported that evaporation error on their collected samples was approximately 1%.

2.5 Performance Parameters

This section will define some performance parameters that were used when analyzing experimental and computational results.

2.5.1 Averaging Methods

The choice of averaging method is important when calculating the average value of a set of data. For all averaging, it is required that each sample is given a weighting factor which is representative of its significance [45]. For a set of data where every sample is equally important, the weighting is constant and an arithmetic average is used (See Equation 2-40) [45].

$$\overline{X}_{AR} = \frac{\sum_{i=1}^{n} X_i}{n} \qquad \textbf{2-40}$$

When the importance of individual samples varies, an appropriate weighting metric must be selected. In fluid dynamics, two commonly used weighting metrics are mass flow and area. The formation of mass flow and area weighted averages for an arbitrary variable “X” are shown in Equation 2-41 and Equation 2-42 respectively [45].

$$\overline{X}_{MW} = \frac{\int X\rho w dA}{\int \rho w dA} \qquad \textbf{2-41}$$

$$\overline{X}_{AW} = \frac{\int X dA}{\int dA} \qquad \textbf{2-42}$$

The choice between these two averaging types depends on the average’s representation. For example, when averaging an isothermal velocity profile, an area weighted average would be used to calculate an average velocity based on mass flow, while a mass flow weighted average would be used to calculate an average velocity based on momentum. This is because, coincidentally, a mass weighted average velocity is the same as the integral of momentum divided by the total mass flow. The only situation in which these two values are the same is when the profile is uniform. This is why the same velocity can be used in the conservation of mass and momentum for the perfect mixer solution in Section 2.1 (Equation 2-1 and Equation 2-2). There are many flow properties that can be used to weight an average, but for the purpose of this research only mass flow and area weightings were used.

2.5.2 Root Mean Squared Error

A common method used determine the difference between a set of experimental and computational data is a Root Mean Squared Error (RSME) The RSME formulation for an arbitrary variable "X" is shown in Equation 2-43 [45].

$$RMSE(X) = \sum \sqrt{\left(X_{i,CFD} - X_{i,EXP}\right)^2} \qquad \textbf{2-43}$$

Where: subscript CFD = computational, EXP = experimental

In this basic form, the error is taken to be an arithmetic mean. In this research, RSME is modified to incorporate mass and area weighting as previously described.

2.5.3 Temperature Difference Ratio

One common method of displaying temperature results for a system is a temperature ratio (See Equation 2-44) [46].

$$\theta = \frac{T - T_S}{T_{CL} - T_S} \qquad \textbf{2-44}$$

Where: T_S = secondary flow temperature, T_{CL} = centerline temperature upstream of nozzle

Displaying temperatures using this formulation has many benefits. For example, in this research there are streams of fluid mixing that are initially at their own respective uniform temperatures. At the exit of the mixing tube, these streams will have deviated from their original temperatures depending on the level of mixing. This phenomenon is difficult to see graphically if the raw temperatures are displayed because the observer needs to know the jet and secondary flow temperatures. With the temperature difference, the value can be thought of as a percentage of the range between these two temperatures.

2.5.4 Back Pressure Coefficient

A performance parameter which is commonly used to quantify the pressure at the entrance of the nozzle is the back pressure coefficient (See Equation 2-45)

$$C_{bp} = \left(\frac{P_{CL}}{q_C} \right) \qquad \textbf{2-45}$$

Where: P_{CL} = static pressure upstream of nozzle, q_C = dynamic pressure of potential core at nozzle exit

This parameter is used for quantifying the static pressure required to drive a flow. This encompasses total pressure losses and changes in dynamic pressure caused by the device.

2.5.5 Total Pumping

In order to quantify the amount of passively entrained secondary fluid, a parameter which is commonly used is the total pumping (See Equation 2-46)

$$\Phi = \left(\frac{\dot{m}_3}{\dot{m}_1} \right) \qquad \textbf{2-46}$$

This parameter is used when describing ejector performance when comparing scale models or other dimensionless parameters.

Chapter 3

Experimental Apparatus

3.1 Wind Tunnel

For this research, the Queen's Hot Gas Wind Tunnel (HGWT) off campus testing facility on Grant Timmins Drive was used. The HGWT is a research wind tunnel which can produce high temperature (up to 600ºC), high velocity (in excess of 100 m/s) air flow for various flow testing applications (See Figure 3-1).

Figure 3-1 Queens Hot Gas Wind Tunnel

A New York type 2512A centrifugal blower supplies a maximum volumetric flow rate of 1.65 m^3/s at a static pressure of 12.6 kPa and a power of 24.6 kW. The maximum operational static pressure is 13.2 kPa at a volumetric flow rate of 1.18 m^3/s and a power of 26.1 kW. The air exits the blower, passes through turning vanes, and is diffused into a settling chamber (See Figure 3-2) where an Eclipse I natural gas burner type 440 TAH-O heats the air to the desired testing temperature [47].

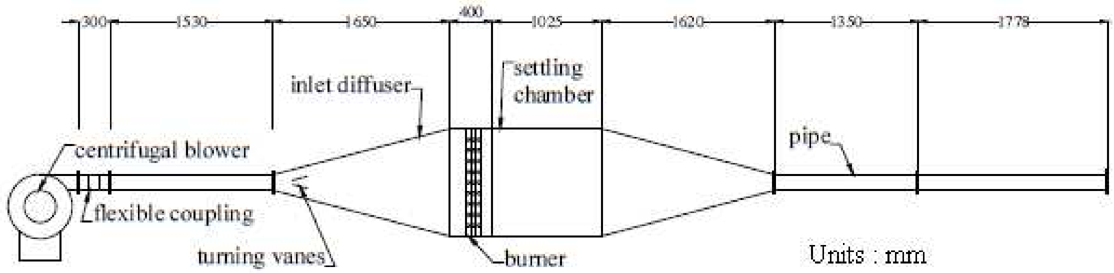

Figure 3-2 Hot Gas Wind Tunnel Dimensions [48]

The purpose of the diffusing section is to slow the airflow down to an acceptable velocity to ensure that the flame is not blown out. The required pressure drop over the burner is between 87 and 299 Pa for safe operation. As the air is heated, the dynamic pressure is increased which requires a higher combustion chamber static pressure. The estimated wind tunnel performance when supplied ambient air at 25ºC is shown in Table 3-1.

Table 3-1 Wind Tunnel Performance [47]

Temperature (ºC)	Mass Flow (kg/s)	Fan ΔP (kPa)	Combustion Chamber P (Pa)	Thermal Power (kW)
100	2.5	11.52	6.06	202
200	2.4	11.87	6.93	433
300	2.3	12.14	7.64	648
400	2.2	12.35	8.23	850
450	2.1	12.44	8.48	947
500	2.1	12.51	8.72	1041
550	2.0	12.58	8.93	1134
600	2.0	12.64	9.12	1224
650	2.0	12.70	9.31	1313

After the burner section, the heated air is accelerated into an outlet pipe (See Figure 3-2) with a diameter of 0.2032 m. The air then flows through this constant area pipe and exits out of the back of the testing facility where the auxiliary components are tested. In this research, the HGWT was modified to represent a 1/8th scale geometric model of a GE LM2500 gas turbine engine exhaust.

3.2 Device Geometry

The device used for this research is a modified air-air ejector. This device includes a flow nozzle which has been modified to incorporate four spray flow nozzles, and a simple mixing tube. All device components where made out of stainless steel in order to endure the high operational temperatures and reduce rusting or degradation.

3.2.1 Nozzle Geometry

The purpose of using an area reducing nozzle on an ejector is to increase the secondary entrainment area while retaining the same mixing tube diameter. This modification does however come with a back pressure penalty due to the increased dynamic pressure of the jet. The existing flow nozzle that was modified for this research is shown in Figure 3-3 & Figure 3-4.

Figure 3-3 Flow Nozzle

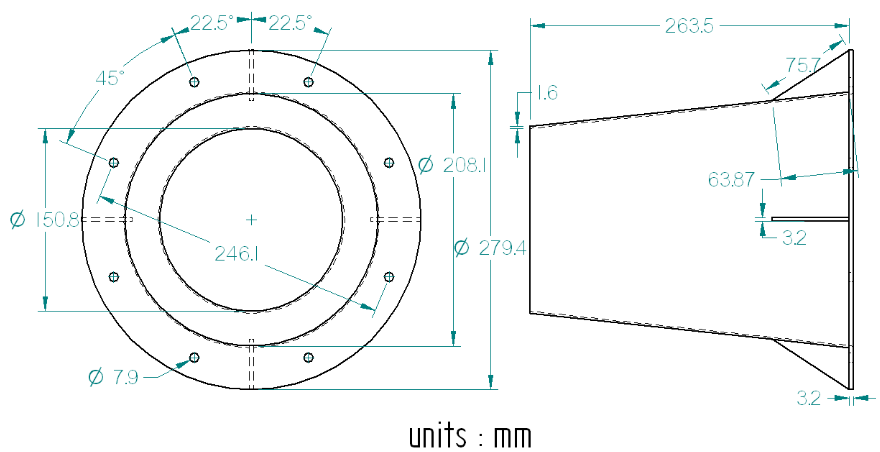

Figure 3-4 Flow Nozzle Dimensions

The dimensionless geometric parameters for the flow nozzle are summarized in Table 3-2.

Table 3-2 Flow Nozzle Dimensionless Geometric Parameters

Nozzle Diameter Ratio $\left(\dfrac{D_{NI}}{D_{NE}}\right)$	1.38
Nozzle Length Ratio $\left(\dfrac{L_{N}}{D_{NE}}\right)$	1.75

Where: D_{NI} = nozzle inlet diameter, D_{NE} = nozzle exit diameter, L_N = nozzle length

Four BETE P66 spray nozzles were used for this research to provide the primary droplet breakup (See Figure 3-5).

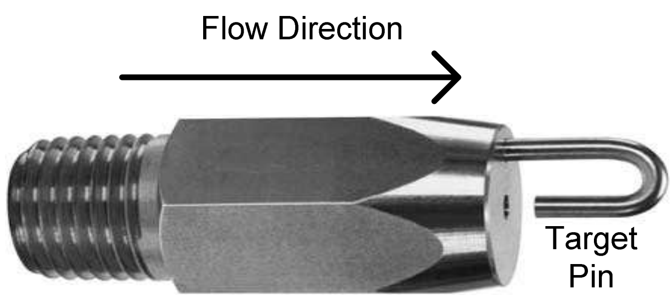

Figure 3-5 BETE P66 Spray Nozzle [49]

This spray nozzle is 46.5 mm long, 16 mm wide, has an orifice diameter of 1.7 mm, and produces a very fine mist of droplets (25-400 μm) by impinging a jet of water onto the target pin [49]. The body is a one piece stainless steel construction with a 6.35 mm NPT male pipe fitting at the base. One spray nozzle was placed every ninety degrees, normal to the flow nozzle's inner walls, and half way down its conical face (See Figure 3-6 and Figure 3-7).

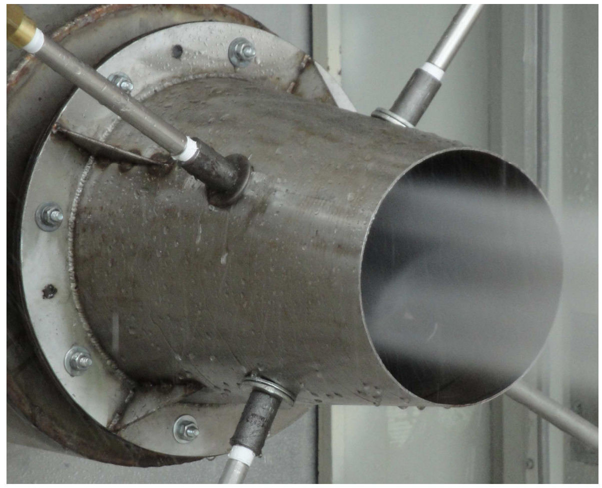

Figure 3-6 Modified Flow Nozzle

Figure 3-7 Spray Nozzle Placement

Each spray nozzle was held in place by tightening it against the flow nozzles inner wall with a 6.35 mm NPT coupling on the outer face. In order to calculate an accurate mass flow rate, individual pressure gauges were placed just upstream of the 152 mm stainless steel nipples seen in Figure 3-6. Each nozzle was supplied with 414 kPa municipal driving pressure which could be finely adjusted with a pressure regulator. It was found in preliminary experiments that the mass flow curve provided in the BETE P66 specification sheet quoted values approximately 15% smaller than actual output. For this reason, the author calibrated all four spray nozzles (See Appendix 9.5A.3. The results of these calibrations are shown in Figure 3-8.

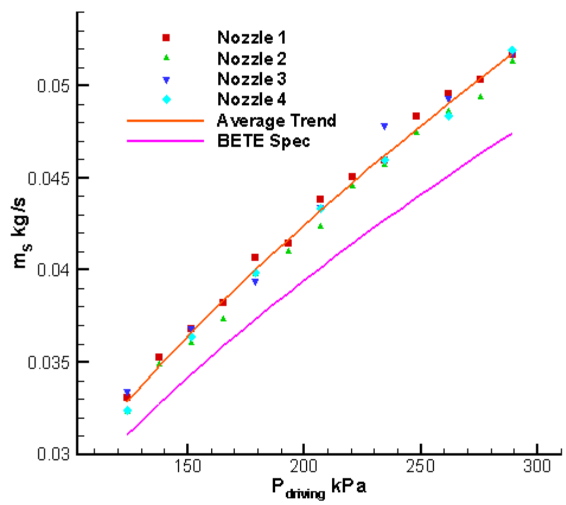

Figure 3-8 P66 Spray Nozzle Mass Flow

The polynomial fit represented by the average trend in Figure 3-8 was used to calculate the spray mass flow rate for the duration of this research.

3.2.2 Mixing Tube Geometry

The mixing tube used for this research was of constant area, with a small bell mouth inlet to reduce flow separation (See Figure 3-9).

Figure 3-9 Mixing Tube Inlet

The dimensions of this simple mixing tube are shown in Figure 3-10.

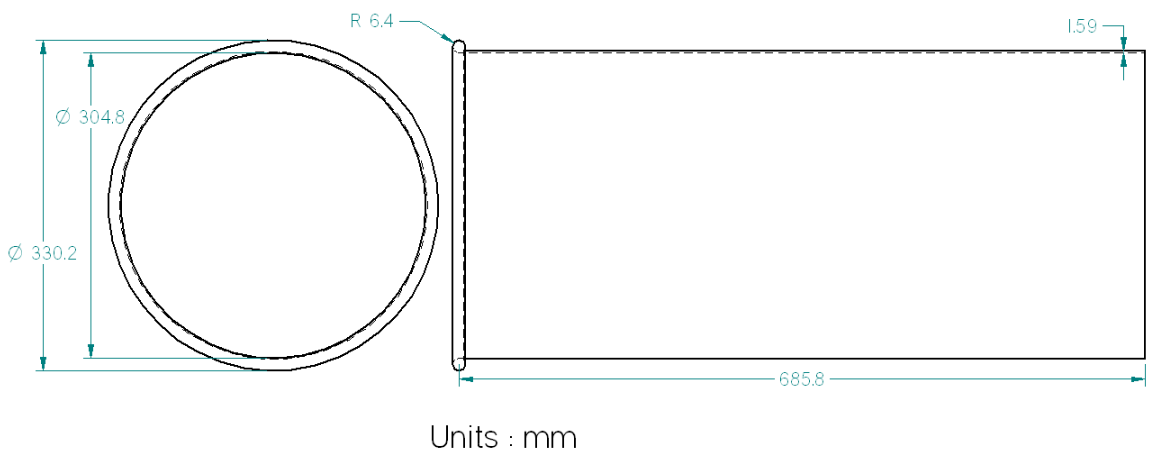

Figure 3-10 Mixing Tube Dimensions

The dimensionless geometric parameters of the mixing tube are summarized in Table 3-3.

Table 3-3 Mixing Tube Dimensionless Geometric Parameters

Ejector Diameter Ratio $\left(\frac{D_{MT}}{D_{NE}}\right)$	2
Length Ratio $\left(\frac{L_{MT}}{D_{MT}}\right)$	2.25
Inlet Radius Ratio $\left(\frac{r_{BMI}}{r_{MT}}\right)$	$2.1\text{x}10^{-2}$
Standoff $\left(\frac{z_{N-MT}}{D_{NE}}\right)$	0.88

Where: L_{MT} = mixing tube length, D_{MT} = mixing tube diameter, r_{BMI} = bell mouth inlet radius, r_{MT} = mixing tube radius, $z_{NE\text{-}MT}$ = axial distance from nozzle exit plane to mixing tube inlet plane

3.2.3 Device Alignment

Mixing tube alignment with the wind tunnel axis was crucial in this research for many reasons. The main reason was to satisfy axisymmetrical assumptions. If the jet core wasn't properly located in the center of the mixing tube these assumptions were violated. An alignment rig using lasers to represent the wind tunnel axis was used to ensure alignment within +/-1º solid angle (See Appendix A.1).

3.3 Data Acquisition and General Instrumentation

This section describes the hardware and software used to obtain experimental measurements. A schematic of the instrumentation setup used in this research is shown in Figure 3-11.

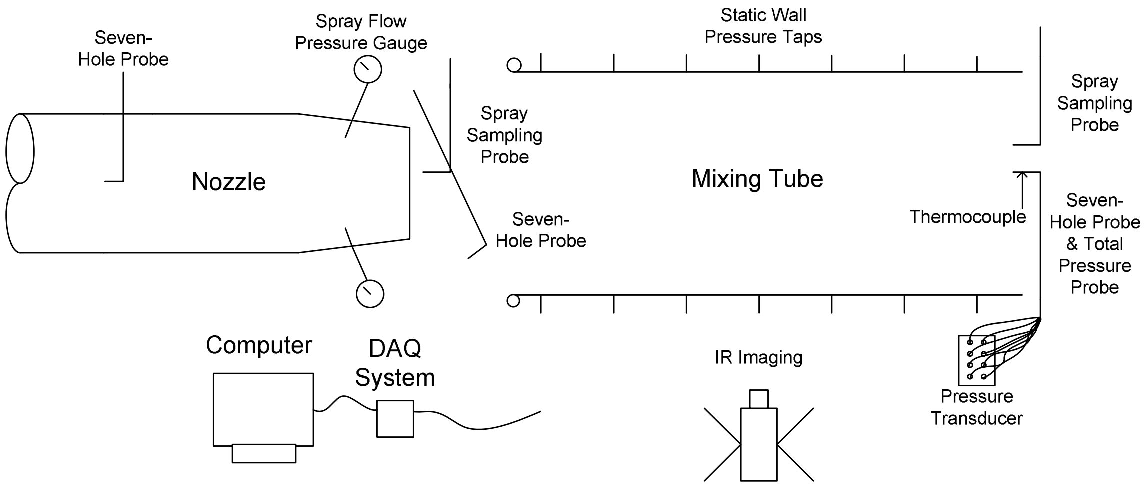

Figure 3-11 Instrumentation Schematic

The following sections will describe all experimental instrumentation shown in Figure 3-11.

3.3.1 Software

The program used to interpret the digital signals from the acquisition system was Labview 5.1. A modified version of pre-existing software written by David Poirier was used for this research. This software allowed for stepper motor control, temperature and pressure measurements, and pressure transducer calibration.

3.3.2 Digital Acquisition System

The digital acquisition system used for this research was a Data Translation DT 3003 Multifunction Card with 64 analogue channels.

3.3.3 Thermocouples

Flow temperature measurements were obtained using K-type thermocouples which are good for a temperature range of -200 °C to +1350 °C with a measurement uncertainty of 2.2°C or 2% (larger of the two) [50]. A hardware compensate circuit was utilized in order to eliminate the need for an ice bath reference junction. This circuit was wired to the DAQ card described in Section 3.3.2 and temperature measurements were recorded at a scan rate of 900 samples/sec. These measurements were then averaged over a sampling time of 1.5 seconds using the software described in Section 3.3.1.

3.3.4 Pressure Transducers

Two different pressure transducers types were used for this research. The first type was a 7 kPa Omega PX139 and the second was a 17 kPa Omega PX143. Both transducers report repeatability error as 0.3% of their full scale range [51] so it's desirable to match their range with the measurement being taken. The 7 kPa transducers were used for the smaller pressure readings such as mixing tube wall pressures and secondary inlet flow pressures, while the 17 kPa transducers were used for the larger pressure readings such as pressure upstream of the nozzle and mixing tube outlet flow pressures. Each pressure transducer used a sampling rate of 900 scans/sec and measurements were averaged over a sampling time of two seconds (See Appendix A.7). The procedure for calibrating the pressure transducers is described in Appendix A.5.

3.3.5 Pressure Gauges

Four Omega PGC-20L-100 pressure gauges were used in this research to measure the spray nozzle driving pressure. These gauges had a measurement range of 689 kPa with a readability of 14 kPa (Uncertainty = 7 kPa) [52].

3.3.6 Digital Scales

Two digital scales were used in this research and were selected for their capacity and accuracy. The first was a Kilotech KLE-2000 with a capacity of 2 kg and a readability of 0.1 g (uncertainty +/-0.05 g) [53]. This scale was used when weighing spray probe samples (max sample size = 50 g). The second was a Kilotech KWS-301 with a capacity of 30 kg and a readability of 1g (uncertainty +/-0.5 g) [54]. This scale was used for measuring spray nozzle calibration samples (max sample size = 5 kg).

3.4 Seven Hole Probe

In order to determine the velocity magnitude, directionality, dynamic pressure and static pressure of an arbitrary flow field, a seven-hole probe was used. Seven-hole probes have the advantage of being able to accurately measure higher angle flows (up to 60° off axis) than other multi-hole probes (I.E. three-hole, five-hole) without having to null the probe (orient into the flow). This is because at any angle less than 60°, there are at least four pressure readings that can be used to calculating the previously mentioned flow variables, which is required [55]. Seven-hole probe theory and calibration procedure are discussed in Appendix A.6. In order to establish an appropriate sampling time to minimize the error associated with averaging transient readings, a pressure sampling sensitivity study was performed (See Appendix A.7). The results of this study indicated that an appropriate sampling time to get an invariant average was around two seconds (1800 samples). The measurement uncertainties resulting from the calibration procedure discussed in Appendix A.6 are as follows: 1.2° yaw angle, 0.63° pitch angle, 1.7% P_{total}, 2.3% q, 2.7% P [56].

3.4.1 Alignment

Alignment of the seven-hole probe was done using a carpenter’s square. One edge of the square was placed against the reference plane and the other was used as a normal reference vector. The seven-hole probe was then rotated until its stem orientation matched that of the square edge. At this point the orientation of the probe was locked by tightening the clam shell clamp. This procedure was estimated to have an alignment uncertainty of approximately 2°. This estimate was based on a probe tip displacement of approximately 3 mm.

3.4.2 Data Analysis

Data analysis for the seven-hole probe involved converting a file of seven pressures and a temperature into three velocity components, a total pressure, a static pressure, and a density. This was done using the calibration coefficients derived in Appendix A.6 and a FORTRAN 90 program created by James Crawford [56].

3.4.3 Multiphase Considerations

In this research, the applicability of using a seven-hole probe in low flux spray flow was tested. Without access to more sophisticated, non-intrusive velocity field measurement methods such as particle image velocimetry or laser doppler anemometry, seven-hole pressure probe data was the only method available for obtaining these measurements during spray flow. After preliminary testing it was observed that as the probe moved in and out of spray flow, the variation in thermal expansion/contraction due to spray impingement caused its tip to deflect up to 15° which produced invalid flow measurements. A proposed solution to this problem was to surround the probe with a heat exchanger which was fed cool water that regulated the thermal expansion (See Figure 3-12).

Figure 3-12 Seven Hole Probe with Heat Exchanger

This method of cooling the seven-hole probe proved to eliminate any deflection caused by the introduction of spray flow.

3.5 Experimental Plane Traverse Robot

In order to collect flow field data for a plane, an experimental plane traverse robot was used (See Figure 3-13).

Figure 3-13 Experimental Plane Traverse Setup

This setup consisted of an Arrick Robotics XY positioner which was vertically mounted to a rolling frame. Stepper motors produced the linear motion, via belts, to allow the positioner to move in the x and y direction. This allowed the operator to move the clam shell clamp to any position on the plane. The plane traverse was designed to accommodate measurements using the seven-hole probe, spray sampling probe, or the total pressure probe.

3.5.1 Stepper Motor Calibration

Stepper motor calibration was performed to ensure that each angular step was producing a desired linear motion. This was done by moving the motors 1000 steps and measuring the distance traveled with a tape measure. Three separate measurements were taken and calibration constants were then calculated by dividing the total distance traveled by the number of steps. This procedure was performed for both stepper motors because the gear reduction was more significant for the Y-axis.

3.5.2 Alignment

Alignment of the XY Positioner with a reference plane (E.G. mixing tube outlet plane) was done using a measuring tape and a carpenter's level. Initially the carpenter's level was used to determine the tilt of the reference plane about its two horizontal axes. Steel plates were then placed on the concrete floor under the traverse robot's casters in order to match the reference plane. A measuring tape was then used to measure the axial distance between four points on the positioner base plate and the reference plane. This last adjustment matched the rotational orientation about the vertical axis. This procedure was estimated to align the XY positioner base plate within 2° of the reference plane.

3.5.3 Measurement Procedure

The use of software described in Section 3.3.1 allowed for the plane traverse measurement procedure to be automated. This required the operator to produce a set of x, y coordinates that defined the desired traverse plane (See Appendix A.8). The software read the first coordinate, moved the stepper motors accordingly, acquired the flow field measurements and repeated the process until the end of the grid file was reached. The grids used for the nozzle exit traverses had an incremental step of 5 mm which resulted in 900 sampled points. The grids used for the mixing tube outlet traverses had an incremental step of 7.5 mm which resulted in 1500 sampled points.

3.6 Experimental Inlet Traverse

In order to determine the inlet flow conditions during spray testing, an upstream test section was designed to be placed between the exit of the wind tunnel and the flow nozzle (See Figure 3-14).

Figure 3-14 Upstream Test Section

The dimensions of the upstream test section before the addition of sliding post mounts are shown in Figure 3-15.

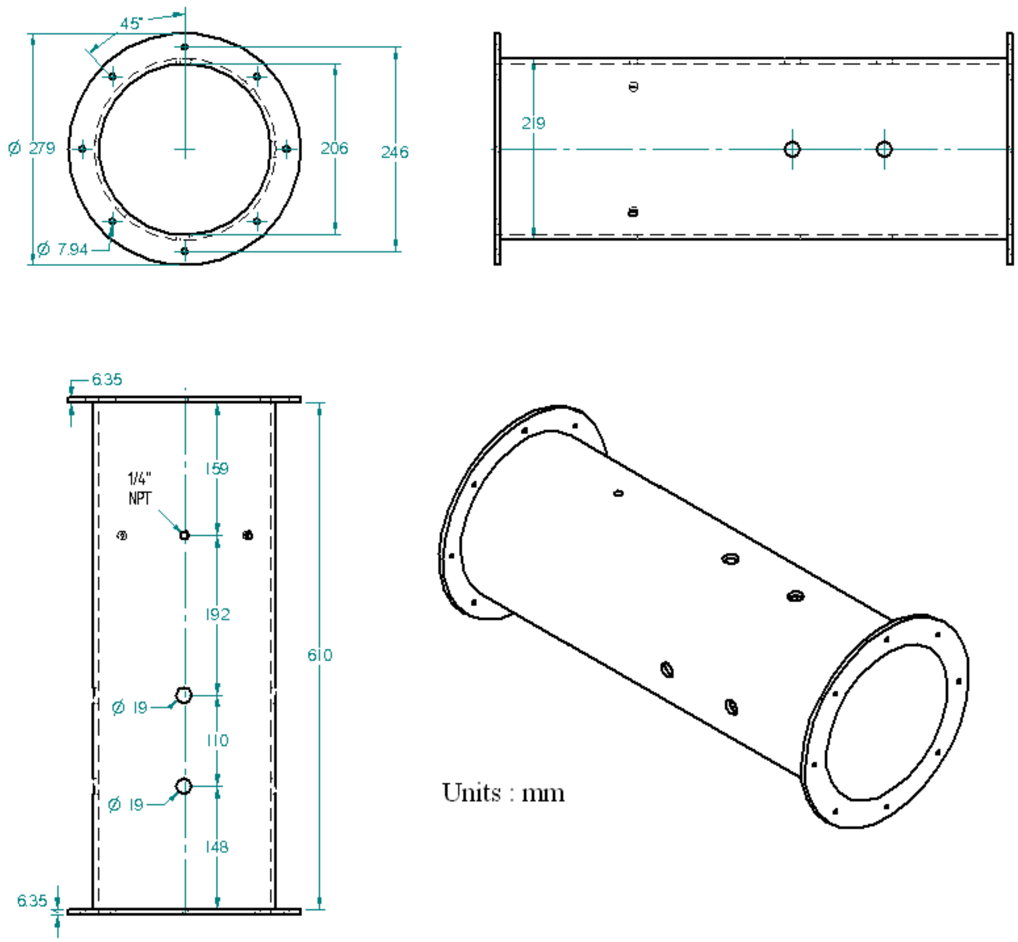

Figure 3-15 Upstream Test Section Dimensions

A sliding post was bolted to the sliding post mount to create a perpendicular face to the test section axis. The seven-hole probe was then placed into a clam shell sliding mount that was face milled to ensure that the probe slid smoothly through a compression fitting that was tapped into the test section wall (See Figure 3-16).

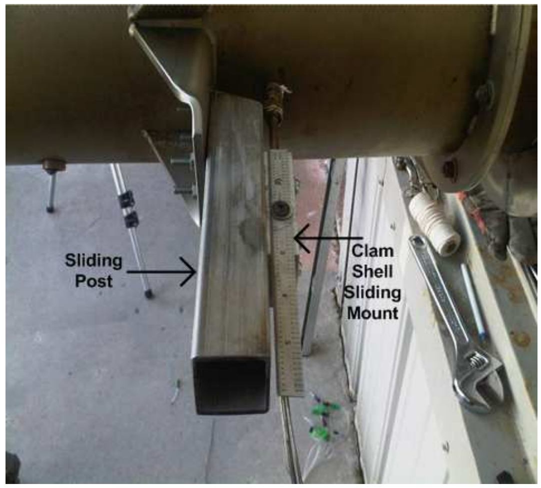

Figure 3-16 Inlet Traverse Setup

This inlet traverse setup allowed for a safe method of manually traversing the pipe radially while ensuring that the seven-hole probe tip was aligned with the axis of the test section.

3.6.1 Alignment

Alignment of the seven-hole probe was done with the test section removed from the wind tunnel. A laser pointer was placed in the alignment plate discussed in Appendix A.1 and once the centerline was established and the seven-hole probe was moved through the compression fitting until the tip reached the laser line. The probe was then rotated until its tip axis was aligned with the laser line axis. At this point the clam shell sliding mount was tightened. This procedure was estimated to have an alignment uncertainty of 2°. This estimate is based on a probe tip displacement uncertainty of 3 mm.

3.6.2 Measurement Procedure

After the seven-hole pressure probe was aligned and placed into the test section the wind tunnel was brought up to the desired testing conditions. Starting from the centerline, flow field measurements were taken in 5 mm radial increments until the probe was approximately 1.5 cm from the pipe wall. Aspects of the probes geometry such as bend radius and tip diameter made it impossible to get measurements any closer to the wall.

3.6.3 Data Analysis

The purpose of taking flow field measurements upstream of the spray nozzle injection points is to be able to calculate an accurate mass flow during spray testing. In order to do so, the following assumptions regarding the inlet flow were made: isothermal temperature profile, radial static pressure equilibrium and an axisymmetric velocity profile. The purpose of the first two assumptions is that they resulted in a uniform density profile. This was required because only one upstream temperature measurement was used to calculate density. The last assumption allowed for a velocity profile to be inferred from a single line of data. For the calculation of mass flow, the pipe cross-sectional area was split into annular strips for which each velocity measurement was applicable (See Figure 3-17).

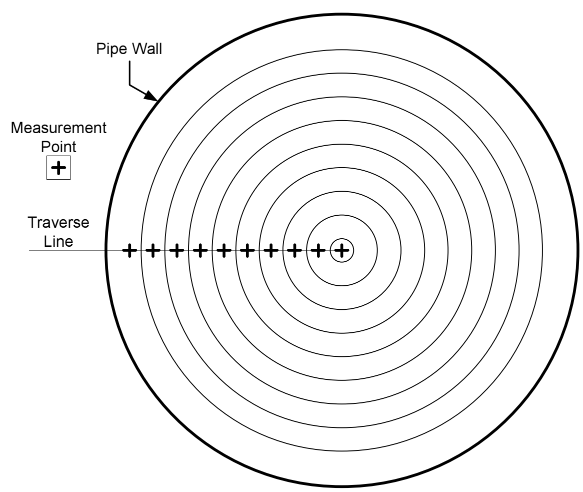

Figure 3-17 Inlet Traverse Area

The total mass flow through the cross-section was calculated using Equation 3-1.

$$\dot{m} = \sum_{i=1}^{n} \rho A_i w_i \qquad \textbf{3-1}$$

3.7 Secondary Inlet Traverse

In order to determine the velocity field and mass flow entering the secondary inlet, a secondary inlet traverse was used. This traverse was designed to take a single line of flow field data between the horizontal quadrant of the nozzle exit plane and its corresponding quadrant on the mixing tube's bell mouth inlet. An axisymmetric velocity assumption was made in order to integrate the mass flow crossing the frustum plane (See Figure 3-18).

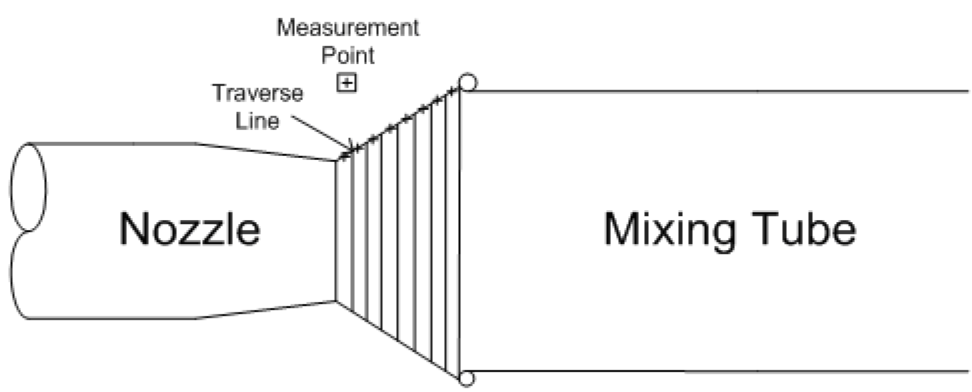

Figure 3-18 Secondary Inlet Area

The secondary inlet traverse setup included a sliding rail with a vertically mounted seven-hole probe. Each end of the sliding rail was bolted to a tripod for ease of alignment with the traverse line.

3.7.1 Alignment

Alignment of the sliding rail was done manually after the wind tunnel heated up because thermal expansion significantly changed the location of the traverse line. Once the wind tunnel heated up, the tripod closest to the nozzle was adjusted in location and height until the seven-hole probe tip touched the nozzle wall's horizontal quadrant. The next step was to slide the seven-hole probe to the other end of the rail and repeat the process for the tripod closest to the mixing tube inlet. This process generally took a couple iterations to properly align the sliding rail and the traverse line. Two sources of misalignment uncertainty were associated with this procedure. The first was uncertainty in traverse line orientation and the second was uncertainty in seven-hole probe alignment with the traverse line. The total alignment uncertainty was estimated to be 2° which caused a small percentage of the total uncertainty associated with secondary inlet measurements (See Appendix A.2.3).

3.7.2 Measurement Procedure

Starting at the nozzle wall, flow field measurements were taken in 5 mm increments by manually sliding the rail assembly and referencing a fixed measuring tape. These measurements continued until the seven-hole probe tip touched the bell mouth inlet on the mixing tube.

3.7.3 Data Analysis

Data analysis for the secondary inlet traverse is identical to that of the inlet traverse discussed previously in Section 3.6.3 with one exception; the assumption of static pressure equilibrium is not made.

3.8 Spray Sampling Probe

In order to measure the mass flux of liquid droplets crossing a plane, a mechanical spray sampling probe was designed and fabricated by the author. A small stainless steel tube was bent ninety degrees in order to create a sampling area which was aligned with the flow, and a collection area which was gravity assisted (See Figure 3-19 & Figure 3-20).

Figure 3-19 Spray Sampling Probe

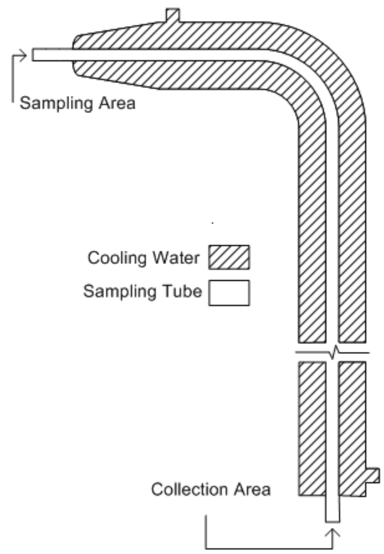

Figure 3-20 Spray Sampling Probe Schematic

A cutaway view of the sampling probe tip dimensions is shown in Figure 3-21.

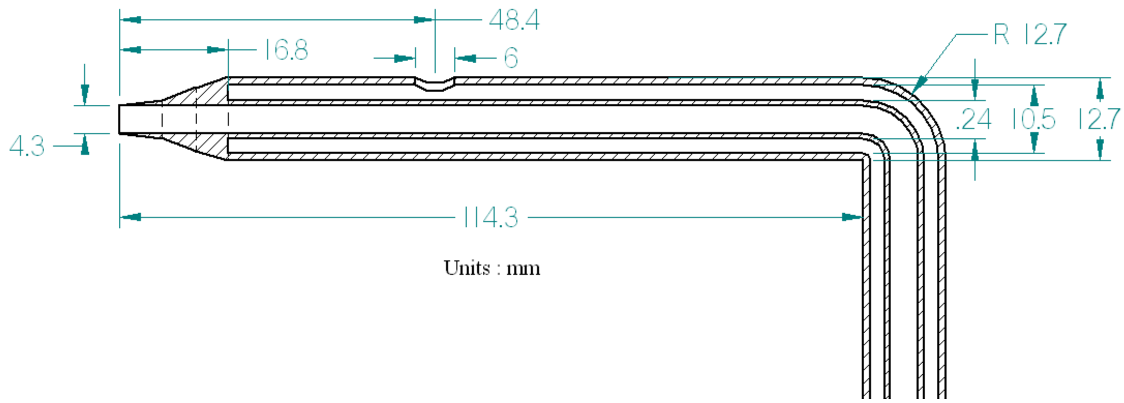

Figure 3-21 Cutaway Spray Sampling Probe Tip Dimensions

As the probe is aligned with the flow the static pressure will rise in the sampling tube due to major losses from wall friction and minor losses in the bend radius [2]. This pressure gradient causes some continuous phase streamlines to curve and divert around the probe, as discussed in Section 2.4.2. It was hypothesized that any droplets upstream of the sampling area would have enough inertia that their trajectories would be unaffected by this streamline curvature and would be collected in the sampling tube. In order to further reduce the diversion of droplets around the probe, the sampling tube wall was knife edged to a point from outside to inside. Using the droplet distribution described in Section 4.4.3, an obedience number and droplet Reynolds number were calculated to determine collection efficiency. For this distribution, the Obedience Number varied between 0.02 and 0.1and the droplet Reynolds number varied between 60 and 300. Using the collection criteria efficiency proposed by Dussourd et al. [42] shown in Section 2.4.2 the author cannot definitively state that the collection efficiency is greater than 99%. It is likely that some of the smaller droplets in the distribution will produce collection error due to the anisokinetic sampling environment.

During sampling, a large portion of the sampling probe can potentially reside in the hot continuous phase. In order to reduce the experimental error caused by evaporation of droplets flowing between the sampling area and collection area, a water cooled heat exchanger was fabricated. It was anticipated that there would still be small amounts of continuous phase flow through the sampling tube. The presence of a cooled wall would inevitably lead to condensation of water vapour present in this flow. The magnitude of this error would increase coincidently with water vapour mass fraction in the continuous phase. This was considered when making conclusions about the spray sampling probe performance.

3.8.1 Alignment

Alignment of the spray sampling probe with respect to the desired sampling plane was done following the same procedure as described in Section 3.4.1.

3.8.2 Measurement Procedure

The spray sampling procedure involved a slight modification to the measurement procedure described in Section 3.5.3. The sampling probe utilized the plane traverse setup to move it through a set of x, y coordinates on the desired sampling plane. The modification was that, after a coordinate was reached, the operator stopped the traverse and manually sampled the spray. A 50 ml beaker was used to collect the spray flow from the collection area of the sampling tube. A collection time of two minutes was chosen in order to get a significant sample (approximately 30 ml in some of the high flux regions). After the sampling was complete, the traverse was moved to the next coordinate and the sample was weighed. The reasoning behind moving the traverse before weighing the sample was that the probe would be given sufficient time to reach a steady state condition before the next sample was taken. This would eliminate any transient effects caused by moving the probe to a new position. A digital scale with a readability of +/- 0.1g (< 0.5% sample size) was used to weigh each sample. Because each sample weight was manually recorded the measurement procedure was very time consuming. This led the author to make a spray flux symmetry assumption for all sampled planes which reduced the procedure time fourfold. Another method of reducing procedure time was to use a non-uniform grid. Because the spray flux contours in this research were highly non-uniform, there were regions that were more significant than others. First, a coarse grid (2 cm increment) was used to locate the regions of high spray flux. Once the region was located, the grid was locally refined and the sampling process was repeated. This was done until the change in integrated spray mass flow was insignificant (5 mm increment). A propagation of the quantifiable uncertainties associated with this sampling procedure is presented in Appendix A.2.6.

3.8.3 Data analysis

Data analysis for the spray sampling data involved converting the sample weight for each coordinate into a spray flux value. The weighed mass was divided by the sampling time in order to get a mass flow. A mass flux was calculated for the coordinate by dividing the collected mass flow by the sampling area. For this probe the sampling area was calculated to be $1.447\text{x}10^{-5}$ m^2. This was calculated using a sampling diameter of $4.29\text{x}10^{-3}$ m which was measured using a Vernier caliper. An accurate measurement of this diameter is critical because any error is squared when calculating the sampling area. The uncertainty in diameter was taken to be +/-0.1 mm to account for measurement uncertainty and non-circularity. This value is twice that of the Venier caliper’s measurement uncertainty and was used as an estimate in lieu of information regarding sampling tube circularity. After a spray flux value was defined for each coordinate, a spray mass flow was calculated by performing a scalar integration of the contour.

3.9 Gas Temperature Probe

One of the experimental challenges with multiphase flow is accurately measuring the temperature of the continuous phase when the discrete phase is at a different temperature. This is particularly challenging with the large temperature differential between the phases. For this reason, there is a requirement for the phases to be separated before a temperature measurement is taken. The author proposed an inertial separating probe to fulfill this requirement (See Figure 3-22)

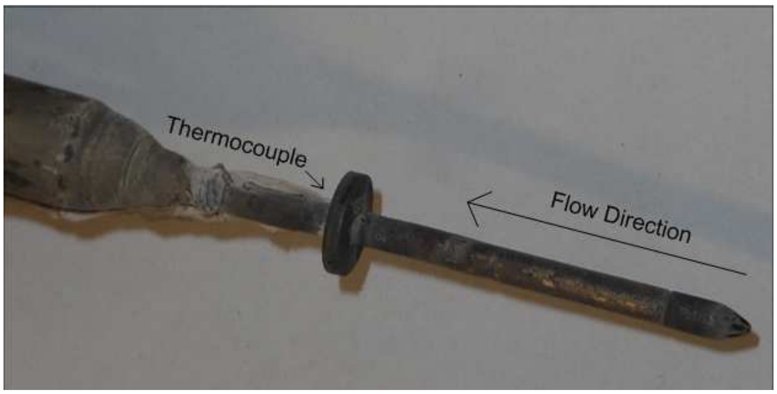

Figure 3-22 Gas Temperature Probe

This inertial separating probe incorporates a simple modification to an existing seven-hole probe so that temperature and pressure measurements could be taken simultaneously. A separating disc (1.5 cm diameter, 3 mm wide) was silver soldered approximately 6 cm back from the probe tip as to reduce the affects on its performance. As the flow stagnates on the circular disc, it would cause a static pressure rise above that of the free stream. It was hypothesized that this pressure gradient would cause both phases to be diverted around the disc. After passing the disc the high inertia droplets would continue on their trajectory downstream, but some of the continuous phase would recirculate behind the disc. This region behind the disc is where a thermocouple was placed in order to measure the isolated continuous phase. Flow visualization of the probe during testing is shown in Figure 3-23.

Figure 3-23 Gas Temperature Probe Flow Visualization

It can be seen from the flow visualization that the probe appears to have operated as anticipated. Some observations are that the front of the disc appears to be in contact with the discrete phase which means it will be cooler than the continuous phase. This will cause the recirculated flow to be cooled by the back of the disc and produce measurement error. Also, any secondary breakup of the discrete phase caused by the presence of the probe and separating disc will act to cool the continuous phase before it reaches the recirculated zone. These sources of experimental error were considered when analyzing the sampled results.

3.10 Total Pressure Probe

It was discovered in preliminary experiments that even very small amounts of spray flow resulted in the plugging of the seven-hole probe pressure ports which caused unacceptable measurement error. A proposed solution was to fabricate a total pressure probe that was large enough to eliminate pressure port plugging (See Figure 3-24).

Figure 3-24 Total Pressure Probe

The total pressure probe consisted of a 19 mm ID stainless steel tube that was bent ninety degrees. This probe allowed the droplets to enter, run down the walls and collect at the probe base. Meanwhile, a pressure port was located in the center of the downpipe to eliminate plugging. It should be noted that if all of the droplet momentum is transferred to the continuous phase before coming in contact with the wall, the total pressure will be representative of the mixture density. If the droplets come in contact with the wall before they transfers any of their momentum, then the total pressure will be representative of the continuous phase density (air & water vapour). The actual situation was found to be somewhere in between these two extremes (See Section 7.4).

3.11 Mixing Tube Wall Pressure

A relatively non-intrusive method of measuring the mixing tube wall pressure is to use surface pressure taps. This involves drilling a small hole in the mixing tube wall, silver soldering a stainless steel tubule into the hole, and grinding the tubule flush to the inner wall. It is important that the tubule be flush with the inner wall because any flow separation over its face will lead to measurement error. Wall pressure data is valuable in determining features of the flow that would otherwise be difficult to measure (pressure recovery and inlet flow separation). A line of nine tubules were placed every 76 mm down the mixing tube wall at four quadrants (See Figure 3-25)

Figure 3-25 Mixing Tube Wall Pressure Taps

Four separate pressure transducers were used to acquire wall pressure data. This allowed almost every measurement to be taken simultaneously.

3.12 Mixing Tube Wall Temperature

Infrared imaging was used in this research to measure mixing tube wall temperatures. This is a completely non-intrusive measurement technique that provides insight into flow features inside the mixing tube (I.E. rate of energy transfer to the secondary flow). The experimental setup of the IR camera is shown in Figure 3-26.

Figure 3-26 Infrared Mixing Tube Wall Temperature Measurement

3.12.1 Measurement Technique

An Inframetrics Thermacam SC1000 IR camera was used to acquire thermal images that were post processed with a Thermacam Researcher 2001 software package. For this camera, the measurement range was from -10°C to 1500°C with an uncertainty of 2°C or 2% (larger of the two) [57] . The mixing tube walls were painted flat black in order to bring their emissivity close to unity and reduce reflections. The actual emissivity was calibrated experimentally by matching the apparent wall temperature reported by the camera to a wall thermocouple measurement. The assumption of a negligible temperature gradient through the mixing tube wall was used when comparing to computational data. This assumption is valid if the rate of internal conduction in mixing tube wall is much larger than the rate of heat loss to the surrounding air at the mixing tubes outer walls.

3.13 Instrumentation Summary

A summary of the instrumentation discussed in Chapter 3 along with respective measurement ranges and uncertainties are shown in Table 3-4.

Table 3-4 Instrumentation Summary

Instrument	Measurement Range	Measurement Uncertainty
K-Type Thermocouple	-200 °C to +1350 °C	Larger of 2.2°C or 2%
Omega PX139 Pressure Transducer	7 kPa	0.3% Range
Omega PX143 Pressure Transducer	17 kPa	0.3% range
Omega PGC-20L-100 Pressure Gauge	689 kPa	7 kPa
Kilotech KLE-2000 Digital Scale	2 kg	0.05 g
Kilotech KWS-301 Digital Scale	30 kg	0.5 g
Seven-Hole Probe	17 kPa	1.2° yaw 0.63° pitch 1.7% P_{total} 2.3% q 2.7% P_{static}
Inframetrics Thermacam SC1000 IR Camera	-10 °C to 1500°C	Larger of 2°C or 2%

Chapter 4

Computational Procedure

4.1 Mesh Generation

This section describes the methodology used for creating the geometry and mesh used for the CFD analysis in this research.

4.1.1 Geometry Generation

The software package Gambit 2.4.6 was used to create the fluid domain geometry for the computational analysis in this research. A journal file was used to parameterize all of the important geometrical constants to ensure repeatability and ease the process of geometry modifications. Journal files are Gambit's command scripts that can be written to eliminate the need for the program's graphic interface. Journal files also facilitate the declaration of variables, use of mathematical expression, and conditional statements like most common programming languages. The first step in writing the journal files was to create all of the nodes that define the geometry and define parameterized relationships between these nodes. In doing this, the geometry could be later altered by simply changing the parameter values. After the nodes were defined the geometry was built in a bottom up approach by connecting the nodes with lines, creating faces with connected lines, and creating volumes with stitched faces. The journal file used in this research is in Appendix B.6.

4.1.2 Meshing Methodology

The main objectives of the meshing methodology were to create an entirely structured mesh with low cell skew and modest volume changes between neighbouring cells. The first step was to create a boundary layer mesh on the mixing tube walls and bell mouth inlet. The boundary layer function creates a structured mesh that grows at a specified rate from the wall. This function is used to meet the grid refinement requirements discussed in Section 2.2.2 while enforcing conformity with the core flow mesh. It was found in preliminary meshing attempts that terminating a boundary layer inside the fluid domain was undesirable. This is because in order to satisfy conformity, a highly refined, unstructured mesh was required to grow the terminated boundary layer to the core flow cell size. A simple solution to this problem was to terminate all boundary layer meshes at a fluid domain boundary, thus eliminating the requirement to conform to the core flow. This was done by rounding the mixing tube wall at its exit, and wrapping the boundary layer around the outer wall (See Figure 4-1 and Figure 4-2).

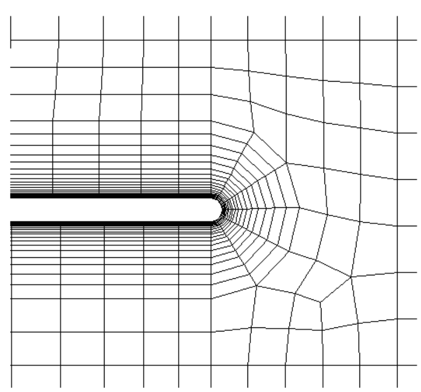

Figure 4-1 Mixing Tube Outlet Mesh

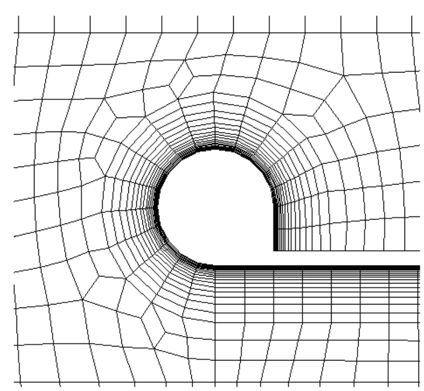

Figure 4-2 Mixing Tube Inlet Mesh

This modification resulted in a cell count reduction of approximately 10% for the entire fluid domain and reduced the maximum cell skew from 0.97 to 0.5. After the boundary layer mesh was defined, the core flow mesh was created. This was done by axially sweeping structured face meshes through the entire fluid domain. In order to satisfy mesh conformity, every volume was given the same tangential node count (See Figure 4-3).

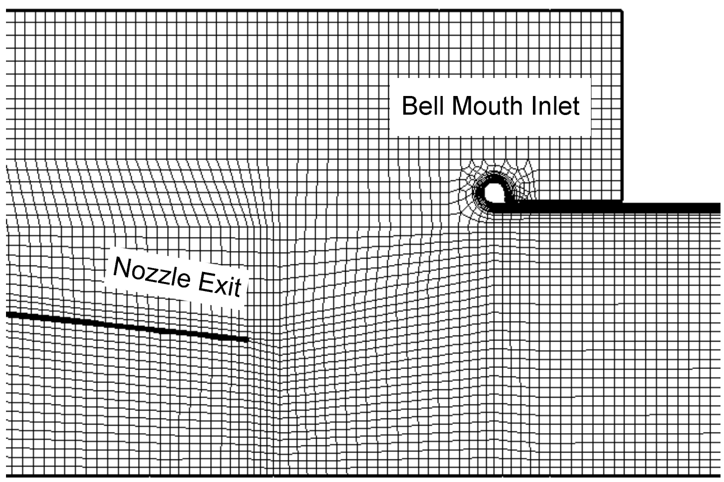

Figure 4-3 Symmetry Plane Mesh

The only regions that couldn't use axially swept meshes were at the bell mouth inlet, and the mixing tube outlet round. This is because any mesh projection onto a curved surface creates highly skewed cell. Instead, these volumes utilized a tangentially swept face mesh (See Figure 4-4) with only a few unstructured cells (See Figure 4-2).

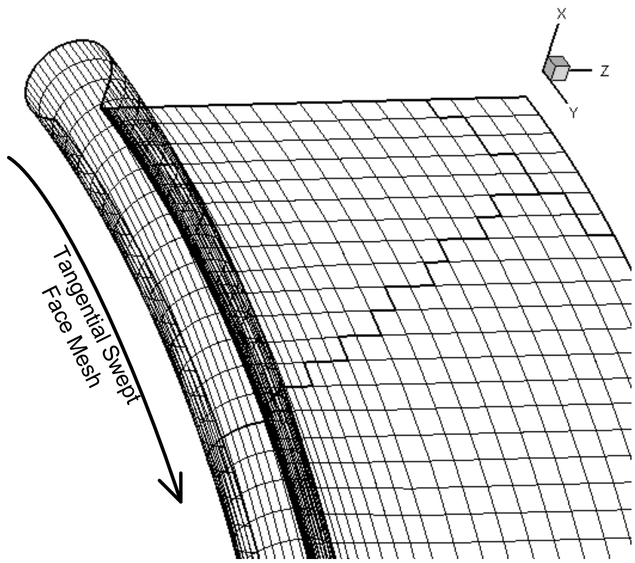

Figure 4-4 Bell Mouth Inlet Face Mesh

These cells were required in order to transition from the curved boundary layer cells to the axially aligned cells of the core flow. In order to determine the effects of modeling the spray nozzle presence, a separate mesh was made. This incorporated a simplified geometric representation of the spray nozzle (cylinder) which was meshed with an unstructured grid. Convergence was found to be an issue with preliminary simulations so the original mesh was used for subsequent simulations.

4.2 Boundary Conditions

Figure 4-5 shows the boundary conditions that were applied to all boundary faces of the fluid domain.

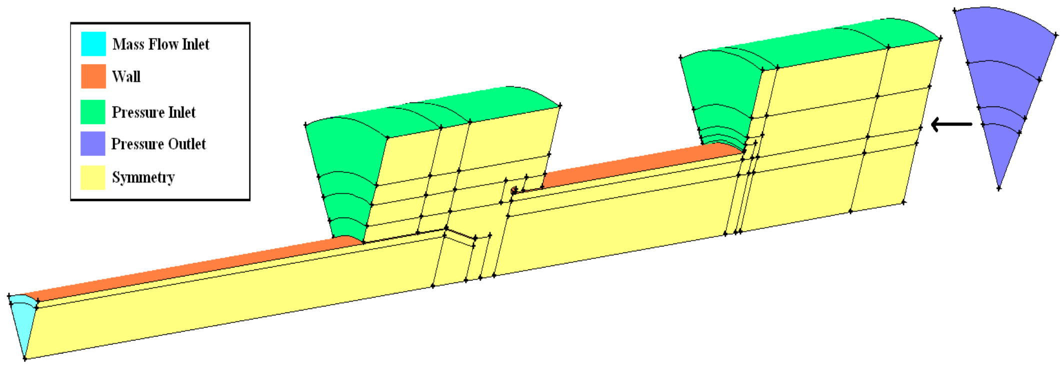

Figure 4-5 Boundary Conditions

4.2.1 Mass Flow Inlet

A mass flow inlet was used for the nozzle inlet boundary condition because it allows for the use of the ideal gas law when calculating density. The velocity inlet condition doesn't account for the effects of static pressure on density which resulted in approximately 5% inlet velocity error. This causes an error in the calculation of backpressure and for this reason the velocity inlet condition wasn't chosen. The user inputs for the boundary condition include mass flow, total temperature, and turbulence intensity. The only input that was unknown was the turbulence intensity which was estimated as 5% from a previous study by Qi Chen using the same wind tunnel [48]. The static pressure for the boundary is implicitly calculated by the numerical solution. The input conditions used for this research are summarized in Table 4-1 where the inlet velocity is considered uniform.

Table 4-1 Mass Flow Inlet Conditions

Mass Flow (kg/s)	1.3
Total Temperature (°C)	470
Turbulence Intensity (%)	5

The constituents of the combustion were not accounted for in this study in order to simplify the boundary definition. This choice was made following a calculation using a combustion constituent calculator written by the author and is shown in Appendix B.5. The mass fraction of water vapour was found to be less than 3 % and wasn't accounted for during the computational study. It was also found in research performed by Qi Chen [48] that with similar operating conditions, the combustion process occurred in a very lean mixture with a large amount of excess air. It was found that the fluid properties (I.E. thermal conductivity, density, etc.) changed by less than 3% when accounting for combustion constituents.

4.2.2 Wall

An adiabatic, no-slip wall condition was used for the inner and outer faces of the nozzle and mixing tube. This allowed the solid to be modeled as negative space. The assumption of an adiabatic wall is validated through an energy balance shown in Table 5-3. The discrete phase interaction with the wall boundary was set to reflect, which is representative of a completely elastic collision. It was found in this research that the discrete phase never came in contact with the wall so this interaction definition had no effect on the solution. The wall roughness was modeled as smooth (lowest turbulent line on the Moody diagram [2]) and all other inputs were left as default.

4.2.3 Pressure Inlet

In order to create an atmospheric condition from which the entrained fluid is drawn and the mixing tube outlet flow issues, two plenums were created. Pressure inlet boundary conditions were applied to all inlet plenum faces and many of the exit plenum faces. This boundary condition allows the user to define the total pressure of the fluid passing through its face. The one stipulation is that the flow is forced normal to the boundary, or to a user specified vector. This means that the plenum boundary must be placed far enough away that it doesn't affect any streamline curvature or flow structures. Following temperature measurement taken experimentally from the secondary inlet, the air temperature entering the boundary was set to 25°C with a turbulence intensity of 1%. This turbulence intensity was chosen under the assumption that the secondary flow originated from stagnant air which is inherently unagitated.

4.2.4 Pressure Outlet

This boundary condition is similar to the pressure inlet with a few exceptions. The pressure specified by the user is the static pressure which is uniform over the boundary. There are two main situations where these boundary conditions don't apply and can affect the solutions results. The first is the situation of streamline curvature through the boundary. Streamline curvature occurs from the presence of a pressure gradient that this boundary doesn't properly simulate. This means that the pressure outlet boundary must be placed far enough downstream of the mixing tube exit that it doesn't affect any potential streamline curvature. The second situation where the pressure outlet doesn't apply is if there is reversed flow. The reason is because reversed flow is forced normal to the boundary as a default. There is an option to have the layer of cells adjacent to the boundary dictate the flow orientation, but the same issue with streamline curvature that was previously described applies. As long as the boundary is sufficiently downstream of the mixing tube exit reversed flow should not affect the solution. For the same reasons as discussed in the Section 4.2.3, the temperature of air crossing the boundary was set to 25°C with a turbulence intensity of 1%.

4.2.5 Symmetry

This boundary condition was applied to all faces that represented a cut plane through the fluid domain. The use of a symmetry plane reduces the cell count but must only be used when applicable. The boundary condition assumes that there is no flow or gradients of any variables, on average, normal to the face. This applies to the situation at hand because there is no flow swirl and the entire geometry is axisymmetrical. For the spray flow cases, there were two separate meshes created. For the cases where two spray nozzles were operational, the symmetry planes were defined at 180°. For the cases where four spray nozzles were operational, the symmetry planes were defined at 90°. These symmetry planes apply under the assumption that gravitational effects on the particles are negligible. Because the particle velocities are so high and the residence time is so short, it was calculated that particle trajectories would experience negligible effects and that the assumption was valid.

4.3 Solution

This section describes the definition of the schemes used to discretize, couple, and solve the Navier Stokes equations.

4.3.1 Discretization Scheme

When using a finite volume method to solve a differential equation, a discretization scheme is required to produce equivalent algebraic equations that apply to each volume. In order to produce finite algebraic equations for each volume, flow variable values are assigned to their faces and centers. The job of the discretization scheme is to approximate the derivative of flow variables using only these face and center values. For this research, a second order discretization scheme was used for pressure and a second order upwind scheme was used for all other flow variables.

These schemes are suggested for situations where the flow is highly convective and not aligned with the grid [5]. Higher order schemes are generally used in lieu of refining the mesh, but the results of the grid independence study (Appendix B.1.1) show that such discretization schemes weren't required.

4.3.2 Solver

The job of the solver is defining the order in which the governing equations are solved. A segregated pressure based solver calculates each equation sequentially and adjusts the flow properties accordingly. This method produces shorter iteration times, but is only suitable for flows where pressure and density aren't strongly coupled (I.E. Incompressible Flow). A coupled density based solver calculates each equation simultaneously, ensuring that the flow properties satisfy all equations. This method slows down the convergence process, but is more suitable for compressible flow [5]. For this research, a segregated pressure based solver was used based on a preliminary calculation of the nozzle Mach number which was approximately 0.28. At this Mach number the flow can be considered incompressible [58].

4.3.3 Pressure Velocity Coupling

The use of a segregated solver requires a pressure–velocity coupling scheme. The reason for this is that pressure only appears in the momentum equation. Since each equation is solved separately the solution of pressure tends to oscillate. The job of the pressure-velocity coupling scheme is to ensure that the velocities used in the momentum equation also satisfy the continuity equation. This is done by correcting the calculated pressure and as a result the oscillation is damped [5]. The pressure velocity scheme used for this research is the SIMPLE scheme. This scheme is suggested for steady state, complex flows where convergence may be an issue [5]. This scheme was chosen over the SIMPLEC scheme which hastens convergence, but is better suited for simple flows.

4.4 Physical Models

This section describes the models used to describe the physical phenomenon occurring in the experimental flow that can't be resolved due to computational limitations.

4.4.1 Turbulence Model

The turbulence model used in this research was a modified RNG k-ε model. The justification for choosing this model is described in Chapter 7. It was found in literature that for non-isothermal shear layers, the effect of density gradients on the turbulent viscosity term is not accounted for using commercial RANS turbulence models [7]. A modification to the RNG k-ε turbulence model was written by the author following an empirical modification described by Abdol-Hamid et al. [7] (See Equation 2-7 to Equation 2-16). This model was chosen following a comprehensive turbulence model comparison shown in Section 7.1. The user defined function used to modify the turbulent viscosity in the RNG k-ε model is shown in Appendix B.7. C+ programming language was used for compatibility with Fluent's UDF compiler. Because the user is required to model the turbulent viscosity for the entire domain, the effects of the wall must be accounted for. This required the author to include the enhanced wall treatment method of calculating the turbulent viscosity in the near wall region [5]. The enhanced wall treatment model was chosen after a wall treatment sensitivity study performed in Appendix B.2. This study found that in order to model the flow separation at the mixing tube bell mouth inlet, the near wall viscous sub layer needed to be resolved as discussed in Section 2.2.2.

The first step was to define the intersection of the viscous affected wall region and the fully turbulent core flow. This was done using a wall Reynolds number shown in Equation 4-1 [5].

$$\mathrm{Re}_y = \left(\frac{\rho y_w \sqrt{k}}{\mu} \right) \tag{4-1}$$

Where: y_w = distance from wall to cell center

At a Re_y value of 200 the flow is considered fully turbulent and the turbulent viscosity is calculated using the core turbulence model. Under a value of 200 the turbulent viscosity is calculated using Equation 4-2 [5].

$$\mu_{t,2Layer} = \rho C_\mu l_\mu \sqrt{k} \tag{4-2}$$

Where the viscosity length scale is calculated using Equation 4-3 [5].

$$l_\mu = 0.0658 y_w \left(1 - e^{\frac{-\mathrm{Re}_y}{70}} \right) \tag{4-3}$$

The final step was to blend the turbulent viscosity of the core flow with that of the near wall. This is done using the turbulent viscosity blending function shown in Equation 4-4 [5].

$$\mu_{t,enh} = \lambda_\varepsilon \mu_t + (1 - \lambda_\varepsilon)\mu_{t,2Layer} \tag{4-4}$$

Where the blending factor is described by Equation 4-5 [5].

$$\lambda_\varepsilon = \frac{1}{2}\left[1 + \tanh\left(\frac{\mathrm{Re}_y - 200}{0.675} \right) \right] \tag{4-5}$$

This blending function produces a smooth transition of turbulent viscosity from the wall to the core flow which promotes solution convergence. The affect of the modified turbulent viscosity constant can be seen in Figure 4-6.

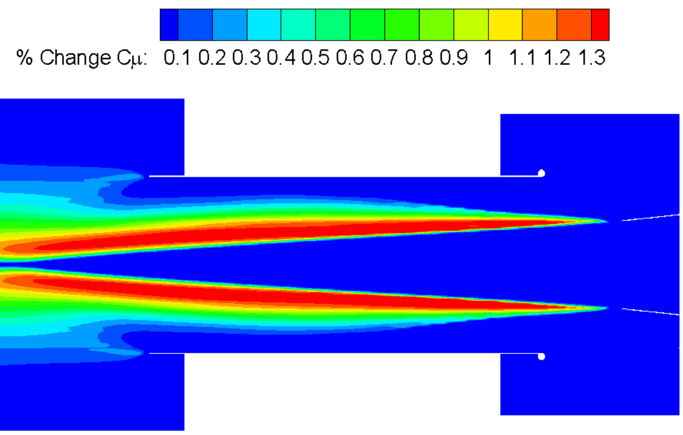

Figure 4-6 Modified C_μ Contour

From this contour it's apparent that the modified RNG k-ε turbulence model localizes the change in turbulent viscosity in the shear layer where the magnitude of the temperature gradient is the largest, as desired (See Appendix 9.5B.7). The effect of this localized increase in turbulent viscosity is best displayed in Figure 7-2 as a reduction in potential core length.

4.4.2 Discrete Phase Model

In general, there are two ways to model multiphase spray flow. The first is to treat the flow as a continuum moving through a control volume which is known as the Eulerian method. This method is generally only chosen when the discrete phase volume fraction is more than 10% [5]. For the cases in this research, the maximum discrete phase volume fraction never exceeded 0.1%. For this reason, the Lagrangian method was chosen. This method tracks clusters of identical particles, known as parcels, through the fluid domain and is better suited for discrete phase volume fractions less than 10%. Since the volume fraction is small, the parcels volume is not considered when calculating the continuous phase equations. Rather, the discrete phase's interaction with the continuous phase is calculated solely through the cell's source terms [16]. The simulation is considered transient until the parcels exit the domain. At this point each subsequent time step is the same as the last and the solution becomes steady state.

4.4.3 Breakup Model

It was discovered in preliminary simulations that the commercial breakup models available for Fluent 6.3.26 were under predicting the secondary droplet breakup after being injected. This may be because the two models that are available (TAB and WAVE) are designed for different Weber Number regimes as discussed in Section 2.3.2. For this reason, the author modeled the secondary breakup based on the findings of Varga et al. [26]. Calculating the Weber number of the particles directly after injection using the primary breakup Sauter mean diameter provided in 9.5A.4, the Sauter mean diameter was found graphically using Figure 4-7.

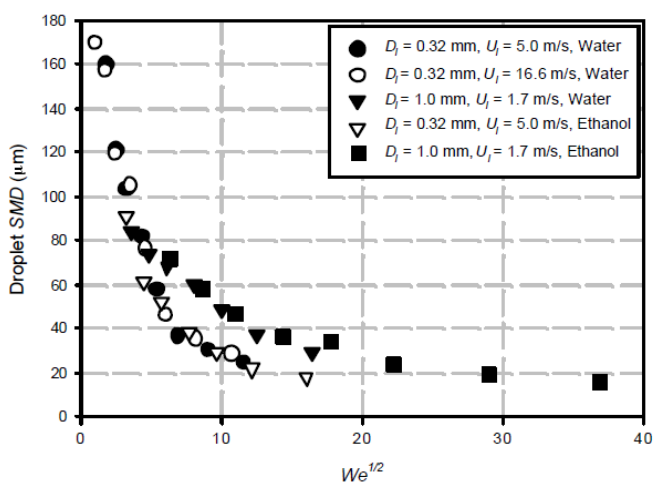

Figure 4-7 Weber Number Effect on Sauter Mean Diameter [26]

Using a calculated $We^{1/2}$ of five, the Sauter mean diameter was found to be 65 μm. This is a significant level of secondary breakup when comparing to a primary breakup Sauter mean diameter (160 μm) as quoted from the BETE P66 specification sheet (See Appendix A.4). The distribution of particles was modeled using a Rosin-Rammler distribution, as previously discussed in Section 2.3.4, which is described by Equation 2-36. With little known about the actual distribution of particles, the average size factor (δ) was taken to be the Sauter Mean Diameter. Using a spread factor of 3.5 (default), twenty particle diameters, a maximum diameter representing the 98th mass fraction percentile, and a minimum diameter representing the 2nd mass fraction percentile, a mass fraction histogram is shown in Figure 4-8.

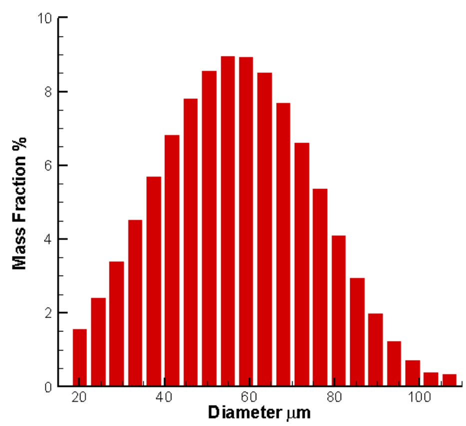

Figure 4-8 Computational Particle Distribution

This particle distribution was used for all spray cases because the changes in injection velocity contributed a small fraction of the relative velocity (I.E. Weber number was constant).

4.4.4 Injection Model

The injection type used for this research was a 90° hollow cone. The injection position was placed half way down the flow nozzle face, and 22mm into the flow, and the orientation was set normal to the wall in order to match the experimental setup.

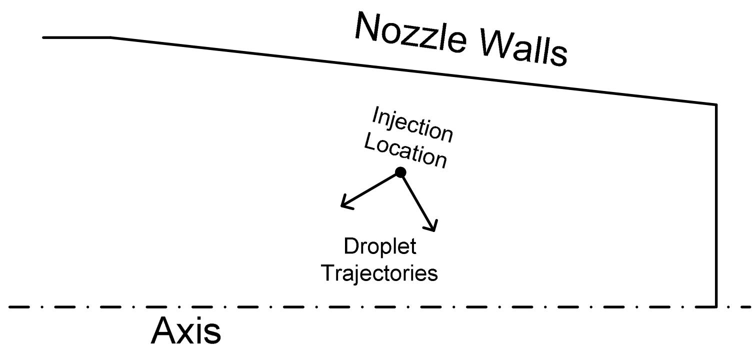

Figure 4-9 Spray Nozzle Injection Location and Orientation

Depending on the spray mass flow, the velocity of particles being injected was defined using Equation 4-6.

$$V_{spray} = \frac{\dot{m}_S}{A_{inj}\rho_d} \qquad \textbf{4-6}$$

4.5 Convergence Criteria

The procedure for judging convergence was as follows: the scaled residuals for all equations were monitored until they reached a magnitude at which they begin to oscillate. These values were generally found to be 10^{-4} for the continuity equation, and 10^{-6} for the remaining equations. Since these residuals are scaled by the initial guess, the value at which they oscillate may mislead the user to think the solution is converged [5]. A better method of defining convergence is to begin monitoring flow features once the residuals appear to have converged. For the continuous phase, the flow features that the author chose to monitor included: standard deviation in mixing tube wall shear stress, standard deviation in mixing tube outlet velocity and temperature, and back pressure coefficient. These statistics were chosen because their values are representative of many different possible changes in the flow field, which makes them a better choice than relatively static values like centerline temperature and velocity. For the discrete phase, the flow feature that the author chose to monitor was the mixing tube outlet water vapour mass fraction standard deviation. As a rule, these values were considered converged when their change over 100 iterations was below 0.1%

Chapter 5

Experimental Results

5.1 Continuous Phase

The first task in gaining confidence in the collection of experimental data was to perform a conservation of mass, momentum and energy for the control volume shown in Figure 5-1.

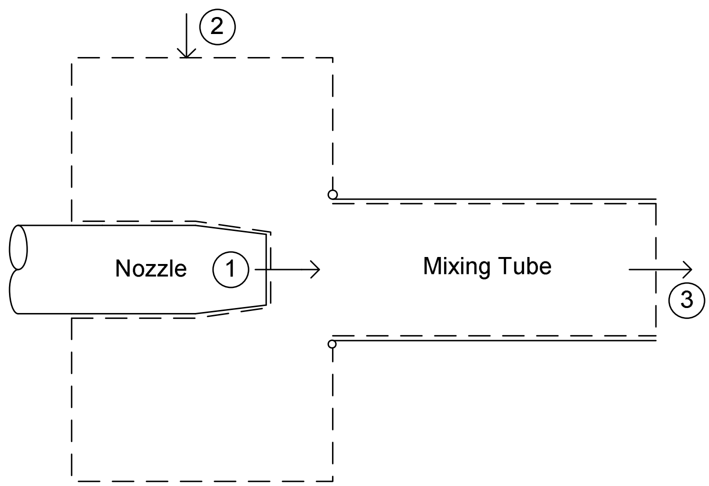

Figure 5-1 Experimental Control Volume

The conservation equations for continuity, momentum, and energy that must be satisfied for the control volume are shown below (Equation 5-1 to Equation 5-3 respectively)

$$\dot{m}_1 + \dot{m}_2 = \dot{m}_3 \quad \textbf{5-1}$$

$$p_1 A_1 + \dot{m}_1 w_1 + p_2 A_2 + \dot{m}_2 w_2 = p_3 A_3 + \dot{m}_3 w_3 \quad \textbf{5-2}$$

$$\dot{m}_1\left(h_1 + \frac{{w_1}^2}{2000}\right) + \dot{m}_2\left(h_2 + \frac{{w_2}^2}{2000}\right) = \dot{m}_3\left(h_3 + \frac{{w_3}^2}{2000}\right) \quad \textbf{5-3}$$

All velocities in this analysis were taken as mass weighted averages

Following the outlet plane traverse procedure discussed in Section 3.5 and the inlet traverse procedure discussed in Section 3.6, contours of velocity are shown in Figure 5-2 and Figure 5-3 respectively.

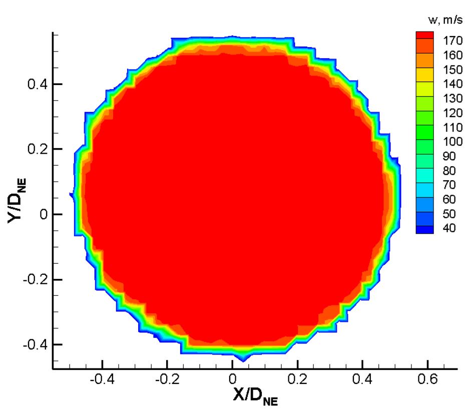

Figure 5-2 Nozzle Exit Velocity Contour

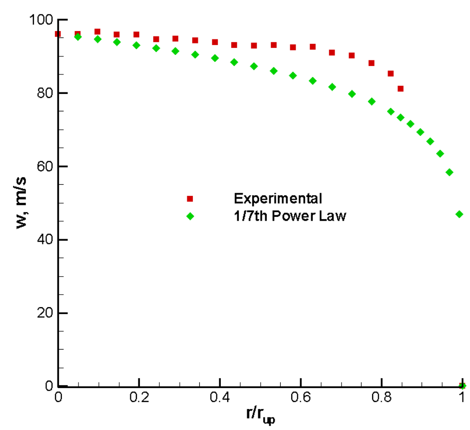

Figure 5-3 Inlet Linear Velocity Contour

A 1/7th power law comparison was shown in Figure 5-3 to compare the inlet velocity profile to a fully developed turbulent pipe flow. Since the inlet traverse is located 15 nozzle inlet diameters downstream of the settling chamber exit (See Figure 3-2) the velocity profile is still developing (fully developed $50 < x/D_{NI} < 70$ [59]) . A conservation of mass was performed on the two nozzle contours presented in Figure 5-2 and Figure 5-3 and summarized in (See Table 5-1).

Table 5-1 Nozzle Mass Flow

Method	Mass Flow (kg/s)
Nozzle Inlet Traverse	1.49 +/- 0.02
Nozzle Outlet Traverse	1.32 +/- 0.03

The first observation is that the inlet traverse mass flow is about 10% larger than that of the outlet traverse. For the inlet traverse there is a large velocity gradient close to the wall caused by the boundary layer. Since the near wall measurement doesn't apply for the entirety of the area as discussed in Section 3.6.3, there is a requirement to model the boundary layer in order to match these mass flows. The author proposed an empirical factor which produces the correct nozzle mass flow from a single inlet centerline velocity measurement (See Equation 5-4).

$$K = \frac{\dot{m}_1}{\rho_{CL} w_{CL} A_{in}} \qquad \textbf{5-4}$$

Where: $\dot{m}_1$ = nozzle exit mass flow, ρ_{CL} = centerline density upstream of nozzle, w_{CL} = centerline velocity upstream of nozzle, A_{in} = cross-sectional area upstream of nozzle

This equation is valid under the assumption that the outlet mass flow has been correctly calculated. Using experimental data, the K factor value was found to be 0.90 and it is assumed that the flow development upstream of the nozzle will not be affected by the introduction of spray flow (K factor is constant).

Following the secondary inlet plane traverse procedure discussed in Section 3.7 the velocity contour is shown in Figure 5-4.

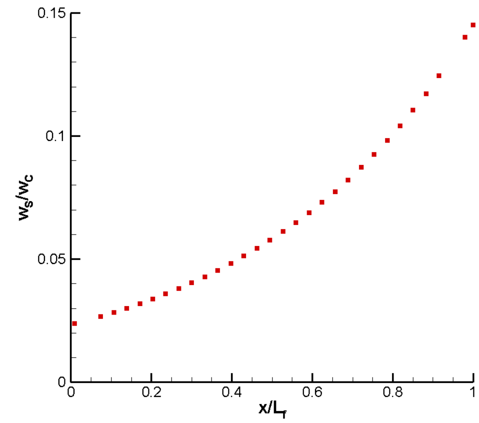

Figure 5-4 Secondary Inlet Velocity Contour

In Figure 5-4 the variable L_f = length of the frustum face between nozzle exit and mixing tube inlet

Following outlet plane traverse procedure discussed in Section 3.5 the velocity and temperature contours are shown in Figure 5-5 and Figure 5-6 respectively.

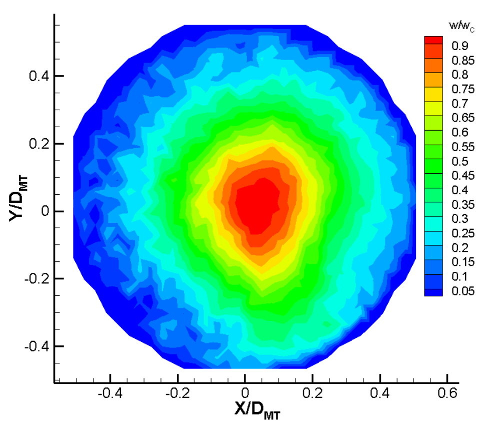

Figure 5-5 Mixing Tube Outlet Velocity Contour

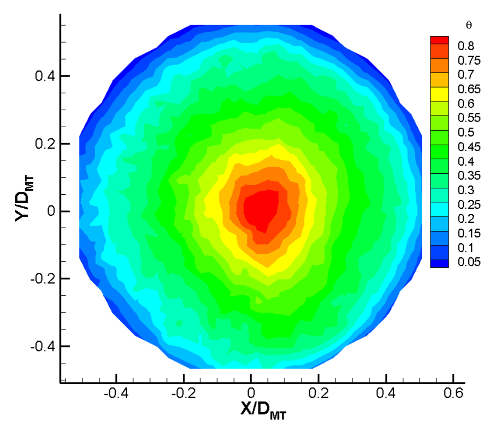

Figure 5-6 Mixing Tube Outlet Temperature Contour

The integrated mass flow for the secondary inlet traverse and mixing tube outlet traverse are shown in Table 5-2.

Table 5-2 Secondary and Mixing Tube Outlet Mass Flows

Method	Mass Flow (kg / s)
Secondary Inlet Traverse	1.56 +/- 0.20
Mixing Tube Outlet Traverse	2.99 +/- 0.05

In performing a conservation of mass for the entire control volume, there is a discrepancy of 0.9 kg/s when comparing the summation of the of the inlet and secondary mass flow to the mixing tube outlet mass flow. This discrepancy is thought to be a result of invalid assumptions required to integrate the secondary mass flow (Axisymmetric velocity contour, appropriate traverse grid resolution), and the calculated experimental uncertainty (See Appendix A.2.3). Taking the secondary mass flow to be the difference between the mixing tube outlet mass flow and the inlet mass flow, a conservation of momentum and energy was performed on the control volume (See Table 5-3).

Table 5-3 Conservation of Mass, Momentum & Energy

	Boundary				
	1	2	1 + 2	3	% Difference
Mass $\left(\frac{kg}{s}\right)$	1.34	1.65	2.99	2.99	0
Momentum + PA $\left(\frac{kg \cdot m}{s^2}\right)$	224	0	224	229	2.4
Energy $\left(\frac{kJ}{s}\right)$	986	497	1483	1498	1.0

From the percent difference results shown in Table 5-3 the author concludes that the assumption stating that the discrepancy in mass flow is a result of an erroneous secondary inlet traverse is valid. Furthermore, the fact that both momentum and energy are conserved within 2.5% shows that the experimental procedure for acquiring the continuous phase results is valid.

In order to determine the applicability of using the perfect mixer model solution shown in Section 2.1 to predict real ejector performance, a comparison with experimental results was summarized in Table 5-4.

Table 5-4 Perfect Mixer Model Total Pumping Comparison

Method	Total Pumping Φ
Perfect Mixer Model	2.66
Experimental	2.23

It is seen in Table 5-4 that the perfect mixer model over predicts total pumping by approximately 20%. One critical factor that affects the performance of real ejectors is inlet flow separation. The recirculating region caused by flow separation on the bell mouth inlet reduces the entrainment area and pumping performance. From these results it is apparent that in order to determine the pumping performance of real ejectors of this geometry, a more sophisticated method must be used than a 1D ideal analytical solution.

5.2 Spray Flow

Four separate spray flow cases were considered in this research. The parameter that was varied between cases was the input mass flow of the cooling water. Because of the type of spray nozzles used and the limitation of using municipal water pressure to drive them, a combination of two and four nozzles were used between cases in order to vary the mass flow to the desired mass ratios (See Table 5-5). The mass ratio for each case was found graphically from a spray nozzle calibration curve shown in Figure 3-8.

Table 5-5 Spray Flow Test Cases

Case Name	Mass Ratio Z (%)	Number of Nozzle
2L	5	2
2H	7	2
4L	11	4
4H	15	4

The following sections describe the experimental data collected on these spray flow test cases.

5.2.1 Sampling Probe Validation

In order to validate the droplet sampling procedure discussed in Section 3.8, a mass balance between the input spray mass flow and a sampling plane just downstream of the nozzle exit was performed. Although this test was conducted in hot flow, an assumption of negligible evaporation between the injection point and the sampling plane was made in order to balance mass. The nozzle outlet spray flux contour is shown in Figure 5-7.

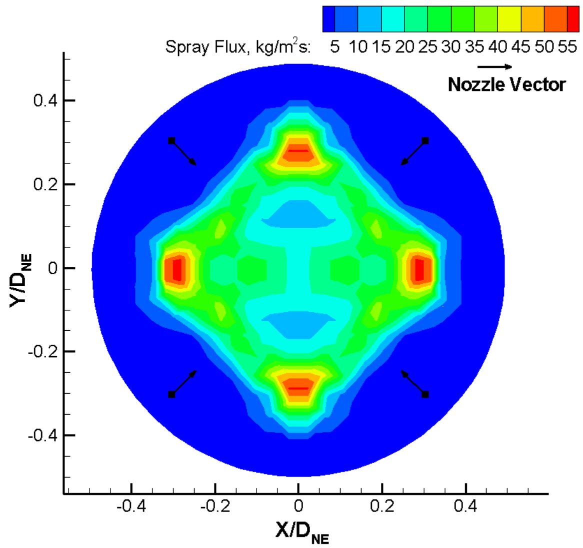

Figure 5-7 4H Nozzle Exit Spray Flux Contour

The spray mass flow was integrated over the sampled area and compared to the inlet spray mass flow in Table 5-6.

Table 5-6 Spray Probe Validation Mass Balance

Input Mass Flow (kg/s)	Collected Mass Flow (kg/s)	Error (%)
0.198 +/- 0.001 (0.5%)	0.208 +/- 0.010 (4.8%)	4.6

An over prediction in collected mass flow is likely indicative of an inadequate grid resolution, incorrectly located symmetry planes, and experimental uncertainty. Because a large portion of the spray flux resided on the symmetry planes (horizontal and vertical line through the contour center) the location and resolution of these regions caused large changes in the integrated mass flow. Even after using the iterative grid method discussed in Section 3.8 these regions were only defined by a couple of sample points. The integrated mass flow did however balance within the estimated experimental uncertainty and was thought to warrant subsequent data collection.

Chapter 6
Computational Results

6.1 Perfect Mixer Model Comparison

The perfect mixer model solution presented in Section 2.1 was used for comparison with computational results (See Table 6-1) to determine the effects spray flow on ejector performance.

Table 6-1 Perfect Mixer Model Performance Comparison

Case	Mass Ratio Z (%)	Perfect Mixer Model			Computational		
		Φ_{air}	T_{MW} (ºC)	w_{MW} (m/s)	Φ_{air}	T_{MW} (ºC)	w_{MW} (m/s)
No Spray	0	2.66	187	70	2.28	212	74
2L	5	2.71	176	68	2.31	193	70
2H	7	2.71	169	67	2.31	186	69
4L	11	2.72	160	66	2.21	182	70
4H	15	2.74	150	65	2.22	172	68

In order to make these comparisons, the percent evaporated spray mass flow for the perfect mixer model was defined to match what was found in the computational results. As seen previously in Table 5-4, the perfect mixer model consistently over predicts the pumping performance due to assumptions that aren't satisfied experimentally (no inlet flow separation). One interesting observation is that for the perfect mixer model, the entrainment of secondary air appears to be proportional to the mass ratio. For the computational results, the entrainment appears to be mostly dependent on the configuration of operating spray nozzles. For the cases with two nozzles operating (2L and 2H) the pumping increased whereas the pumping decreased for the cases with four nozzles operating (4L and 4H). This occurrence is likely a result of changes in inlet flow separation between nozzle configurations which isn't captured in the perfect mixer model. For all cases the pumping is over predicted by approximately 20% which again proves that a 1D analytical solution provides poor predictions of real ejector performance for this geometry.

6.2 Full Scale Comparison

One of the objectives in this research was to determine the effects of scaling on evaporative spray cooling performance. In order to do this, a full scale geometric model was created. It was hypothesized by the author that the cooling performance would increase with a full scale model for a number of reasons. Because the injected droplets experience the same Weber number for both the full scale and 1/8th scale models, the droplet size distribution should be the same. This means that the total droplet surface area affectively scales up with the model. The second reason is that for a similar jet velocity, the increase in ejector length will increase the particle residence time. The mixing tube outlet spray flux contours for both the full scale and 1/8th scale model are shown in Figure 6-1 and Figure 6-2 respectively.

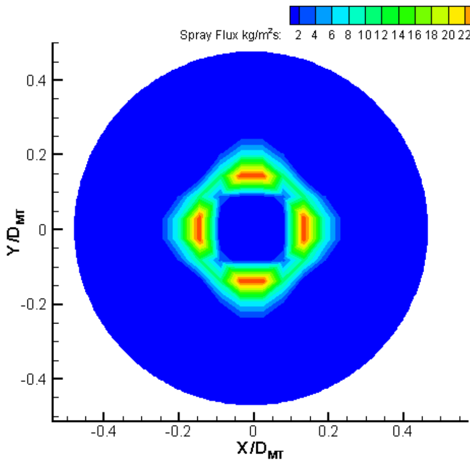

Figure 6-1 Full Scale Mixing Tube Outlet Spray Flux Contour

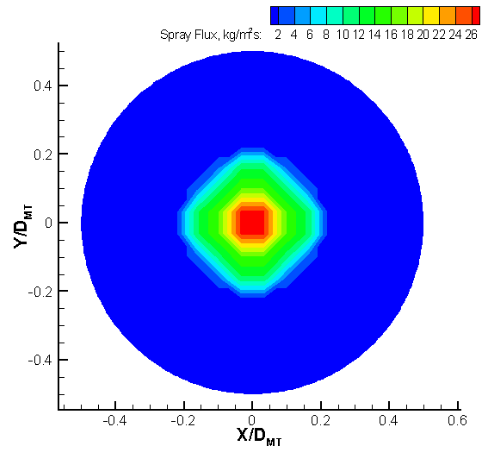

Figure 6-2 1/8th Scale Mixing Tube Outlet Spray Flux Contour

Looking at these spray flux contours it is apparent the droplets in the full scale model have less core penetration than for the 1/8th scale model. This is because, for the same driving pressure, the injection velocity calculated by Equation 4-6 is the same for both cases. By increasing the flow nozzle diameter, the in-plane velocity component of the spray flow becomes less significant. For this reason, the droplets weren't residing in the hottest part of the core for the duration of their residence time. The mixing tube outlet temperature contours for both the full scale and 1/8th scale case are shown in Figure 6-3 and Figure 6-4 respectively.

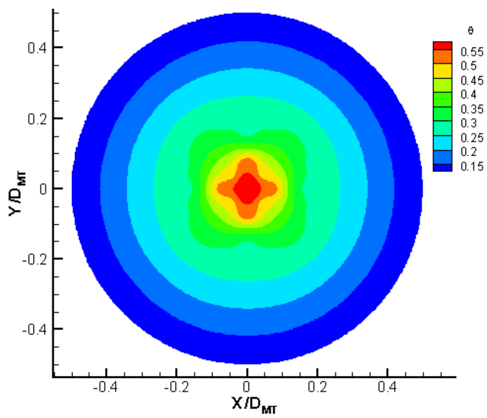

Figure 6-3 Full Scale Mixing Tube Outlet Temperature Contour

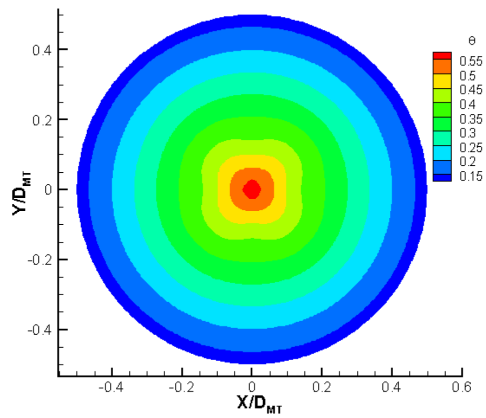

Figure 6-4 1/8th Scale Mixing Tube Outlet Temperature Contour

As seen from these contours the highest core temperature is around the same for both the full scale and 1/8th scale models. This is thought to be largely caused by the lack of droplets in the core of flow for the full scale model as seen in Figure 6-1. The region where the droplets do reside is however cooler in the full scale model. A quantitative comparison of the performance of both these cases is summarized in Table 6-2.

Table 6-2 Full Scale Performance Comparison

Case	Total Pumping Φ_{air}	T_{MW} (°C)	w_{MW} (m/s)	Evaporated Spray Mass Flow %
Full Scale	2.21	142	70	25
1/8th Scale	2.22	172	68	20

As anticipated, the full scale model proved to have better cooling performance than the 1/8th scale model even though the droplets resided in a cooler part of the flow. The evaporated spray mass flow was increased by 5% resulting in a 17% reduction in mass weighted average outlet temperature. This increased performance was entirely provided by an increase in droplet evaporation because the total pumping changed by less than 1%. It is anticipated that by moving the spray nozzle injection position further into the core, or by increasing the number of injection points, the cooling performance could be greatly improved for the full scale case. These simulations were not however conducted for this research.

Chapter 7

Experimental & Computational Results

7.1 Turbulence Model Study

In this section a comprehensive analysis comparing the performance of RANS based turbulence models to experimental data for a no spray case was performed. The objective of this analysis was to select a turbulence model which produced the best agreement for a number of performance criterion. These include a comparison of entrainment ratio, and contours of: outlet velocity, outlet temperature, secondary inlet velocity, mixing tube wall pressure and temperature.

7.1.1 Mixing Tube Outlet Contours

The first investigation was of the mixing tube outlet velocity and temperature contours (See Figure 7-1 & Figure 7-2).

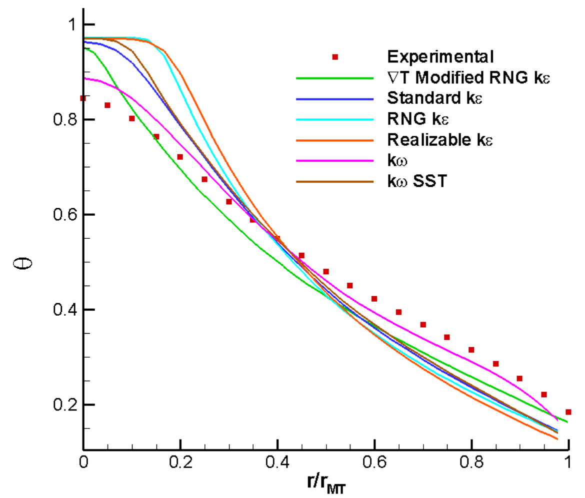

Figure 7-1 Mixing Tube Outlet Velocity Comparison (Air Only)

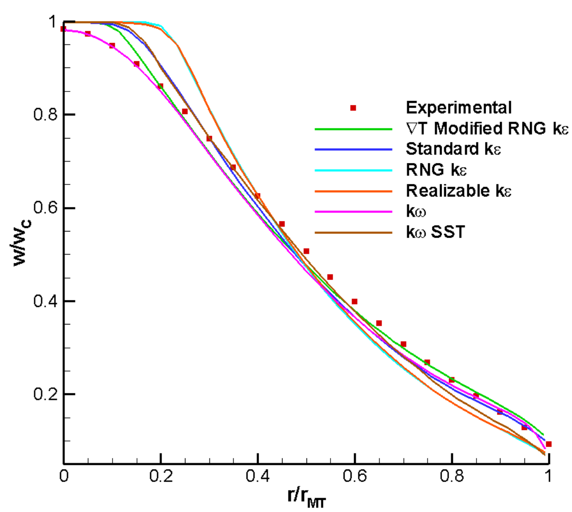

Figure 7-2 Mixing Tube Outlet Temperature Comparison (Air Only)

Through qualitative comparison it is apparent that most of the commercial RANS turbulence models under predict decay of the centerline velocity and temperature. This is likely a result of the under prediction of turbulent viscosity in a non-isothermal shear layer as discussed in Section

2.2.1. It appears from these figures that the kω model produces the best agreement with experimental data. Further analysis will show that this is not in fact the case.

Changing the recommended empirical constant [7] in the modified RNG k-ε model to better predict the centerline decay resulted in an over prediction in entrainment ratio which dropped the temperature at the outer extents of the profile. For this reason the recommended empirical constant was used for subsequent simulations. The discrepancies between experimental and numerical results are more apparent in the temperature contour than the velocity contour because density is less temperature sensitive at the high core temperature range. Literature shows that directly after the end of the potential core (approximately $5D_{NE}$ downstream of nozzle exit [26]) the centerline velocity drops by approximately 32% in the first downstream nozzle diameter [7]. Since the experimental data suggests that the sampling plane was located in this region, the magnitude of error in centerline temperature with respect to axial position is the largest. This could also explain the discrepancies between experimental and computational results. Based on a qualitative temperature contour comparison, one would conclude that the k-ω turbulence model predicts the most accurate outlet profile followed by the modified RNG k-ε model.

7.1.2 Secondary Inlet Velocity Contour

The second comparison investigated was of the secondary inlet velocity contour (See Figure 7-3).

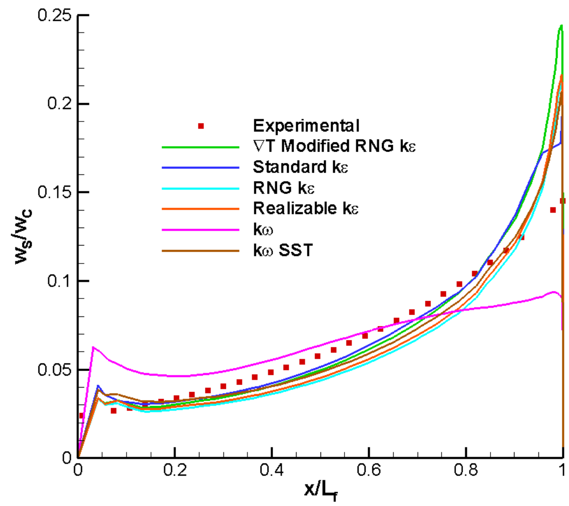

Figure 7-3 Secondary Inlet Velocity Contour (Air Only)

In Figure 7-3 the variable L_f = length of frustum face between nozzle exit and mixing tube inlet

It was previously shown in Section 5.1 that the secondary mass flow was under predicted using the data collected from the secondary inlet traverse. This is likely a result of error in the velocity measurements closest to the mixing tube's rounded inlet ($x/L_f = 1$) where the velocity gradient is the largest. Because of the physical size of the seven-hole pressure probe tip, the velocity difference between its peripheral holes is large enough to violate the isokinetic assumption that is required for calibration [55]. This causes the probe to bias the flow vector away from the traverse planes normal vector causing its axial magnitude to be under predicted. For all computational cases, there is an unphysical velocity spike at the exit of the nozzle ($x/L_f = 0$). This is a result of the coarse mesh used in this region trying to simulate the large velocity gradient. Although the gird sensitivity study found that this phenomenon doesn't affect other flow features (See Appendix 9.5B.1.1) it is clearly visible in this contour. Qualitatively, the contours of secondary inlet velocity produced by the RANS turbulence models, with exception to the k-ω model, are very close to experimental data. The large discrepancies between the k-ω model and experimental data in Figure 7-3 lead the author to believe that the prediction of velocity and temperature contours shown in Section 7.1.1 may have been coincidental for the specific outlet plane sampled.

7.1.3 Mixing Tube Wall Pressure Contour

The third comparison investigated was of the mixing tube wall pressure contours (See Figure 7-4). In Figure 7-4 the variable L_{MT} = mixing tube length, not including bell mouth inlet

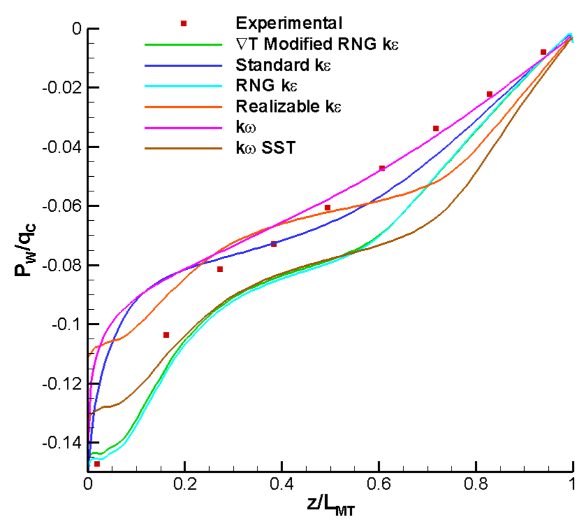

Figure 7-4 Mixing Tube Wall Pressure Contour (Air Only)

The purpose of investigating the mixing tube wall pressure contour is that it is a relatively non intrusive way of collecting evidence of inlet separation and mixing tube pressure recovery. For the cases with little to no separation, the pressure gradient at the rounded inlet ($z/L_{MT} = 0$) is very large which is representative of the flow rapidly decelerating after the apex of the corner. This can be seen for the k-ω and standard k-ε when looking at the z-wise shear stress contours (See Figure 7-5).

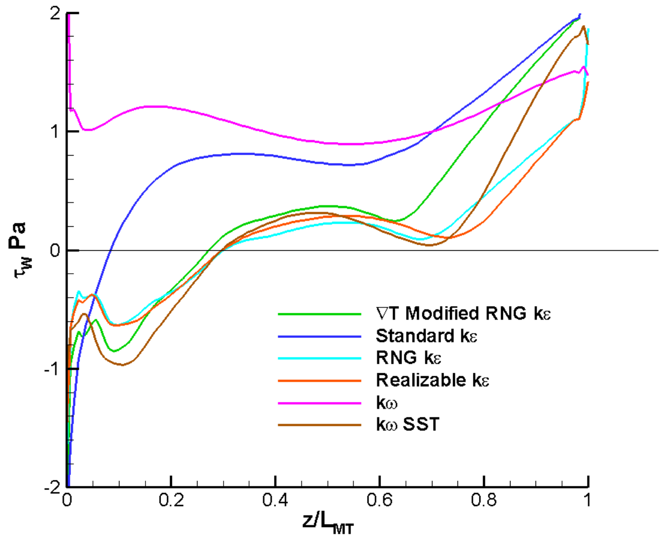

Figure 7-5 Mixing Tube Z-Wise Wall Shear Stress (Air Only)

For the cases with larger recirculation regions, the contours display a shallower pressure gradient close to the inlet because the radius of streamline curvature is increased following separation. This can be seen for the RNG k-ε, modified RNG k-ε and k-ω SST models when looking at the z-wise shear stress contours (See Figure 7-5). One observation is that the models with larger recirculation regions display lower wall pressures for almost the entire length of the mixing tube. This phenomenon occurs as a result of the effective reduction in entrainment area caused by the recirculation region. For the secondary flow to pass through a smaller area, the velocity must be higher, and ergo, the static pressure will be lower. This conclusion is supported by the average z-wise secondary flow velocities that were calculated for the mixing tube inlet plane and summarized in Table 7-1.

Table 7-1 Average Z-Wise Secondary Flow Velocity

Turbulence Model	Average Z-Wise Secondary Flow Velocity $w_{S,MW}$ (m/s)
∇ T Modified RNG kε	26
Standard kε	25
RNG kε	23
Realizable kε	27
kω	20
kω SST	25

Through qualitative comparison, the modified RNG k-ε displays the closest wall pressure comparison to experimental data for the region close to the rounded inlet ($z/L_{MT} < 20\%$) while the kω model appears to display the closest comparison for the latter half of the mixing tube length.

7.1.4 Mixing Tube Wall Temperature Contour

The final comparison investigated was of the mixing tube wall temperature contour (See Figure 7-6)

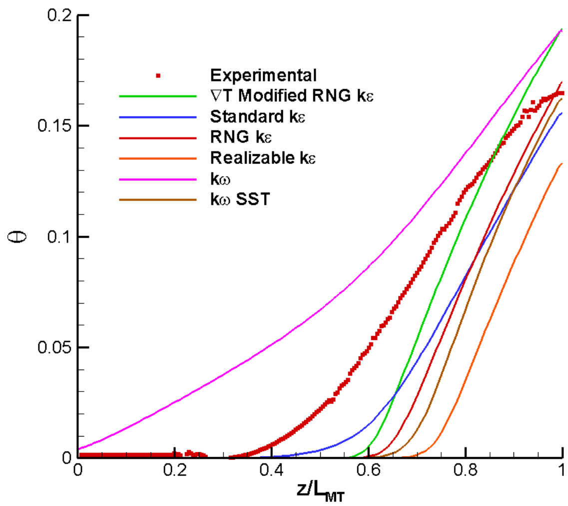

Figure 7-6 Mixing Tube Wall Temperature Comparison (Air Only)

Sample wall temperature contours from the experimental results and the computational ∇ T modified RNG kε results are shown in Figure 7-7 and Figure 7-8 respectively.

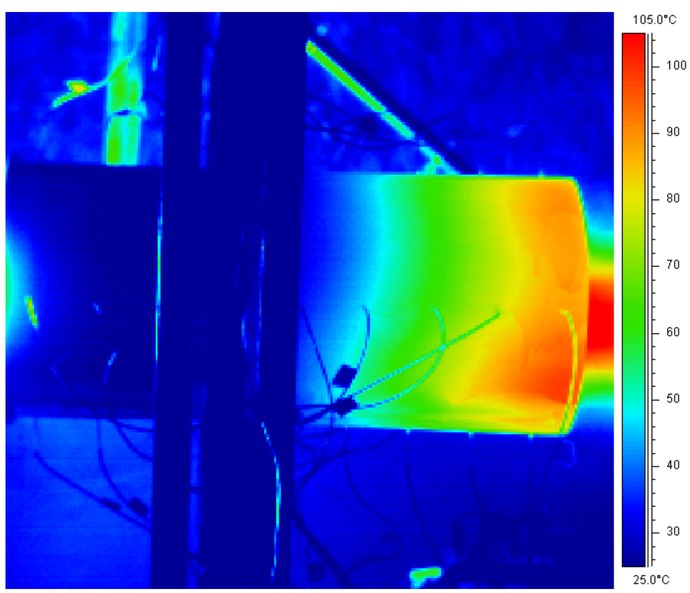

Figure 7-7 Experimental IR Mixing Tube Wall Temperature Contour

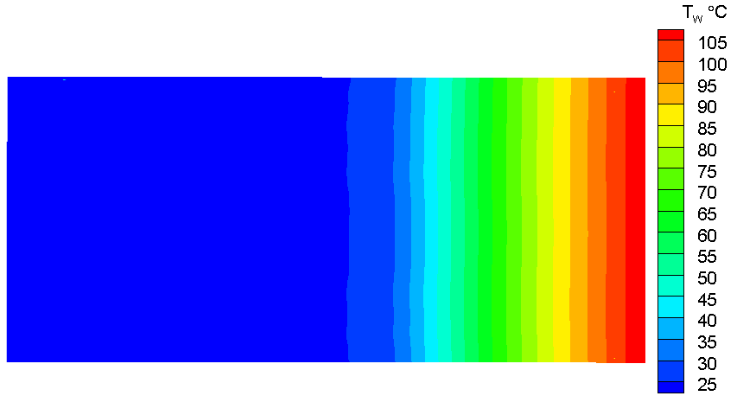

Figure 7-8 Temperature Modified RNG kε Mixing Tube Wall Temperature

The benefit of comparing mixing tube wall temperature contours is they provide evidence of the transfer of energy from the jet to the secondary flow. Looking at the experimental data, the mixing tube wall temperature is representative of the ambient secondary flow for the first 30% of the mixing tube length. Beyond this point the jet has mixed through the secondary flow and the wall temperature rapidly increases. One immediate observation is that the k-ω turbulence model predicts an increase in wall temperature immediately after the rounded inlet ($z/L_{MT} = 0$). This is likely a result of over predicted mixing rates close to the nozzle exit. This conclusion would also explain the higher secondary inlet velocities close to the nozzle seen in Figure 7-3 and the absence of a recirculation zone discussed in Section 7.1.3. The remaining turbulence models all appear to predict the location of mixing tube wall temperature increase further downstream than experimental data. Through qualitative comparison the standard k-ε model appears to provide the best comparison to experimental data followed by the modified RNG k-ε model.

7.1.5 Turbulence Model Selection

In order to select an appropriate turbulence model, a set of quantitative criterion were developed to accompany the qualitative conclusions made throughout Section 7.1. These criteria utilize either a mass or area weighted root mean square error (RMSE) between computational and experimental contours (See Equation 7-1 to Equation 7-6).

$$\sigma_{OT} = \frac{\overline{RSME(T)}_{MW}}{T_C} \tag{7-1}$$

$$\sigma_{OV} = \frac{\overline{RSME(w)}_{MW}}{w_C} \tag{7-2}$$

$$\sigma_{\phi} = \frac{\dot{m}_{3,CFD} - \dot{m}_{3,EXP}}{\dot{m}_{3,EXP}} \tag{7-3}$$

$$\sigma_{SV} = \frac{\overline{RSME(w_S)}_{MW}}{w_C} \tag{7-4}$$

$$\sigma_{WP} = \frac{\overline{RSME(P_W)}_{AW}}{q_C} \tag{7-5}$$

$$\sigma_{WT} = \frac{\overline{RSME(T_W)}_{AW}}{T_C} \tag{7-6}$$

The performance criteria were rated based on the magnitude of their error (shown as bracketed values, 1 = Best, 6 = Worst) and summarized in a decision matrix. Using equal weighting for each variable the score for each turbulence model is shown in Table 7-2 (Lowest Total Score is Best).

Table 7-2 Turbulence Model Decision Matrix

Turbulence Model	σ_{OT} (%)	σ_{OV} (%)	σ_{Φ} (%)	σ_{SV} (%)	σ_{WP} (%)	σ_{WT} (%)	Score
Modified RNG k-ε	4.7 (2)	1.9 (1)	+1.3 (2)	1.02 (2)	1.07 (4)	1.22 (1)	12
Standard k-ε	5.3 (4)	2.3 (3)	+0.7 (1)	0.78 (1)	0.83 (2)	1.56 (2)	13
RNG k-ε	6.8 (5)	3.9 (6)	-4.8 (6)	1.19 (5)	1.13 (5)	1.78 (3)	30
Realizable k-ε	7.6 (6)	2.8 (5)	-4.1 (5)	1.14 (4)	1.06 (3)	2.96 (6)	29
k-ω	3.4 (1)	2.5 (4)	-2.2 (3)	1.50 (6)	0.77 (1)	2.53 (5)	20
k-ω SST	5.0 (3)	2.0 (2)	-2.7 (4)	1.07 (3)	1.40 (6)	2.13 (4)	22

Based on the qualitative observations discussed in Section 7.1 and the scoring shown in Table 7-2 the author chose the modified RNG k-ε turbulence model for subsequent simulations.

7.2 Nozzle Outlet Spray Sampling

A comparison of spray dynamics for the 4H experimental and computational cases was performed and displayed in Figure 7-9 to Figure 7-12.

Figure 7-9 4H Experimental Droplet Interaction

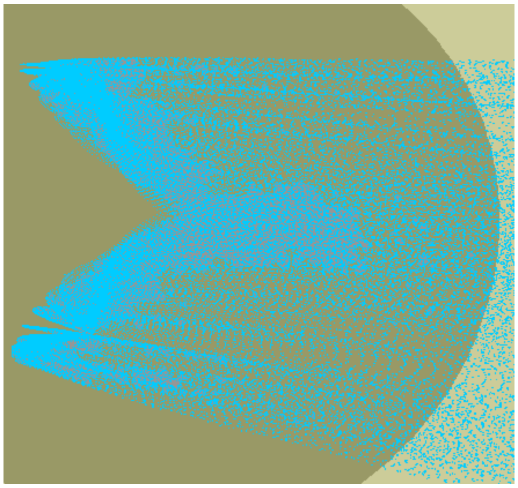

Figure 7-10 4H Computational Droplet Interaction

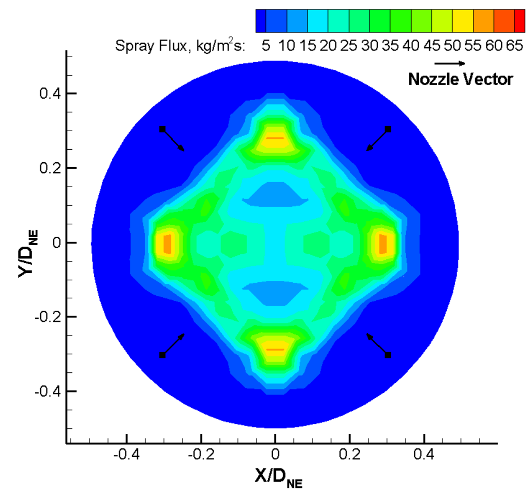

Figure 7-11 4H Experimental Nozzle Outlet Spray Flux Contour

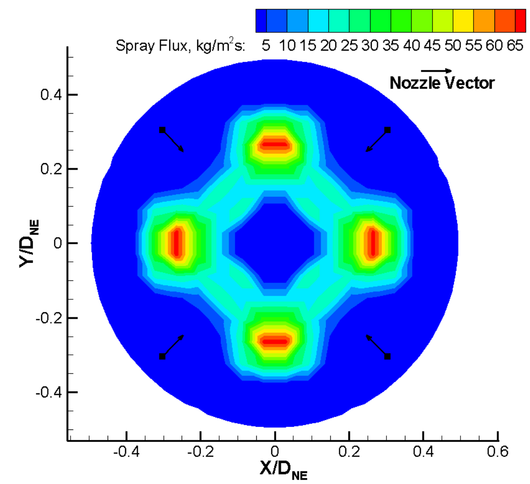

Figure 7-12 4H Computational Nozzle Outlet Spray Flux Contour

It can be seen in the comparison of spray interaction that the experimental case shows droplets closer to the nozzle centerline. This is seen as a reduction in the axial length at which first symmetry interaction occurs (compare Figure 7-9 and Figure 7-10). This is thought to be a result of the hollow cone spray injection model used for the computational case (discussed in Section 4.4.4). It's likely that the experimental injection is not an entirely hollow cone. This hypothesis would also explain the non-zero centerline spray flux seen in the experimental case. Although the hollow cone spray model used for the computational case produced a higher peak spray flux at the symmetry plane, the integrated mass flow was significantly lower (See Table 7-3)

Table 7-3 Nozzle Outlet Spray Mass Flow Comparison

Case	Input Mass Flow (kg/s)	Experimental Collected Mass Flow (kg/s)	Computational Collected Mass Flow (kg/s)	Difference (%)
4H	0.198	0.208 +/- 0.010 (4.8%)	0.193	7.2

The comparison shows that the assumption of negligible evaporation between the injection and sampling plane used in Section 5.2.1 was likely invalid. This leads the author to believe that the errors that were previously calculated in Table 5-6 are underestimated and that their magnitude is better represented in Table 7-3. Through qualitative comparison of patternation characteristics it is seen that the experimental and computational results are quite similar. For this reason, the author decided that subsequent spray sampling data was warranted.

7.3 Mixing Tube Outlet Spray Sampling

After the validation of the sampling probe, mixing tube outlet spray flux was sampled for two of the four spray cases (4L and 4H). These cases were chosen because they were the only cases that used four spray nozzles, and therefore, were the only cases that had two symmetry planes. This allowed the very time consuming manual sampling time to be cut in half. A comparison of experimental and computational spray flux contours for the 4L and 4H cases are shown in .

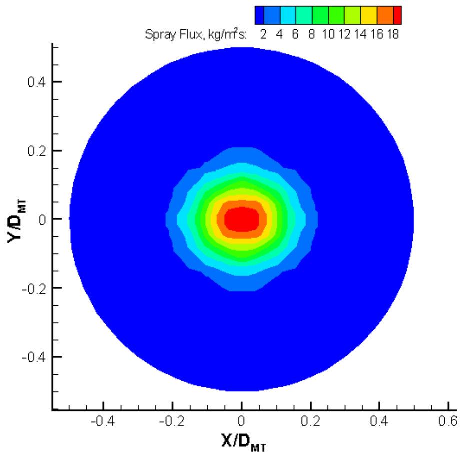

Figure 7-13 4L Experimental Mixing Tube Outlet Spray Flux Contour

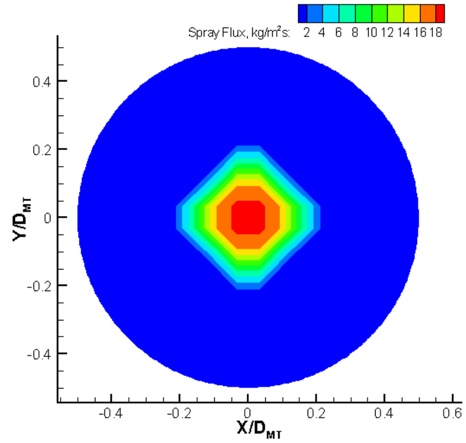

Figure 7-14 4L Computational Mixing Tube Outlet Spray Flux Contour

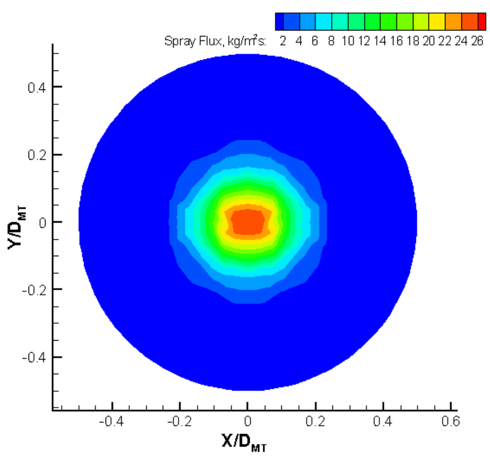

Figure 7-15 4H Experimental Mixing Tube Outlet Spray Flux Contour

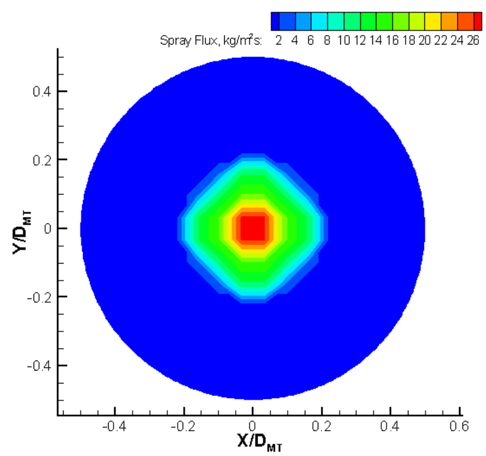

Figure 7-16 4H Computational Mixing Tube Outlet Spray Flux Contour

Qualitatively, it appears that there is good agreement between experimental and computational results, both in spray flux magnitude and position. In both the 4H and 4L case the experimental results display a relatively circular profile, while the computational results display a diamond shaped profile. This is thought to be a result of the hollow cone model used for the computational spray injection as discussed in Section 4.4.4. The experimental injection is likely not a perfect hollow cone which results in more evenly distributed contour. In order to quantitatively compare these cases, a scalar integration was performed and the resulting mass flows are shown in Table 7-4.

Table 7-4 Mixing Tube Outlet Spray Mass Flow Comparison

Method	Mass Ratio Z (%)	Input Mass Flow (kg/s)	Collected Mass Flow (kg/s)	Evaporated Mass Flow (%)	Collected Mass Flow Difference (%)
Experimental	11	0.146	0.108 +/- 0.006 (5.6%)	26	5.6
Computational			0.114	22	
Experimental	15	0.198	0.164 +/- 0.008 (4.9%)	17	3.0
Computational			0.159	20	

7.4 Mixing Tube Outlet Total Pressure Contours

Following the total pressure data collection procedure discussed in Section 3.10 the total pressure contours for all spray cases are compared to their computational equivalents in Figure 7-17 to Figure 7-24. Each total pressure measurement was normalized by the total pressure upstream of the nozzle in order to display the contribution of the spray flow.

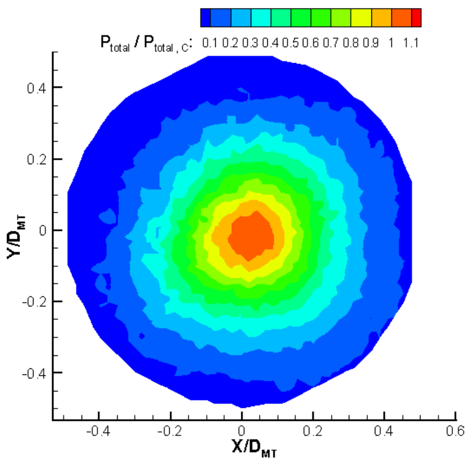

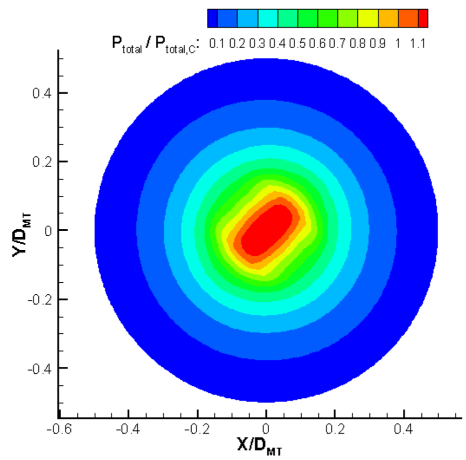

Figure 7-17 2L Experimental Mixing Tube Outlet Total Pressure Contour

Figure 7-18 2L Computational Mixing Tube Outlet Total Pressure Contour

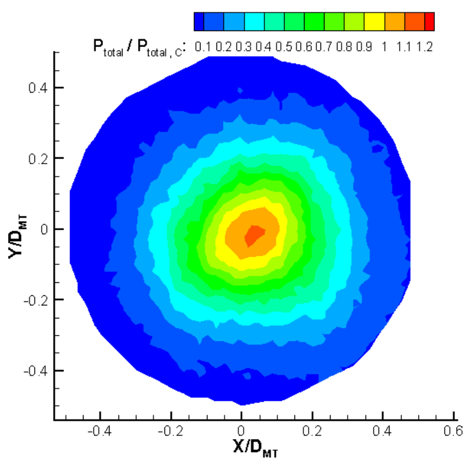

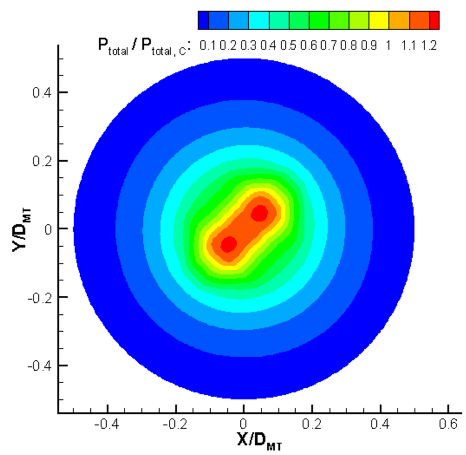

Figure 7-19 2H Experimental Mixing Tube Outlet Total Pressure Contour

Figure 7-20 2H Computational Mixing Tube Outlet Total Pressure Contour

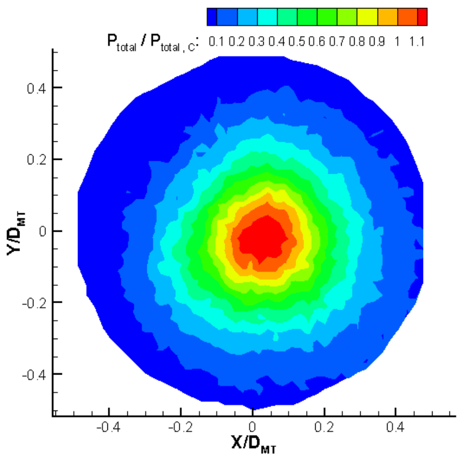

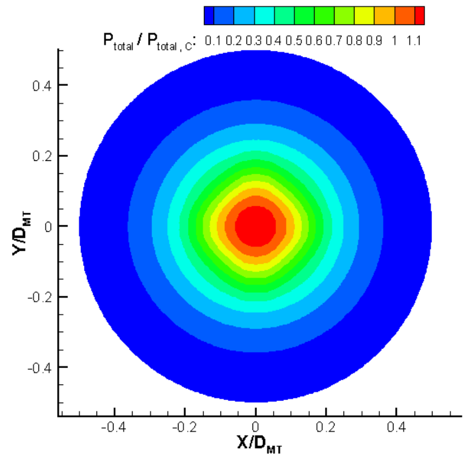

Figure 7-21 4L Experimental Mixing Tube Outlet Total Pressure Contour

Figure 7-22 4L Computational Mixing Tube Outlet Total Pressure Contour

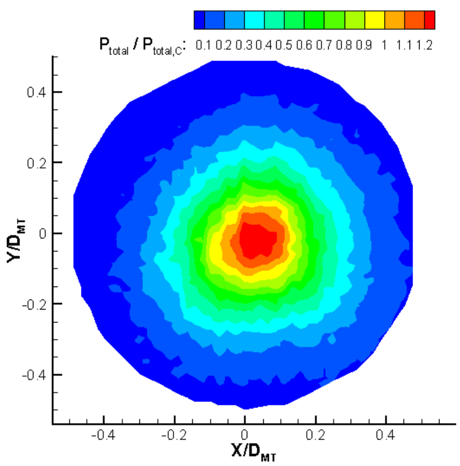

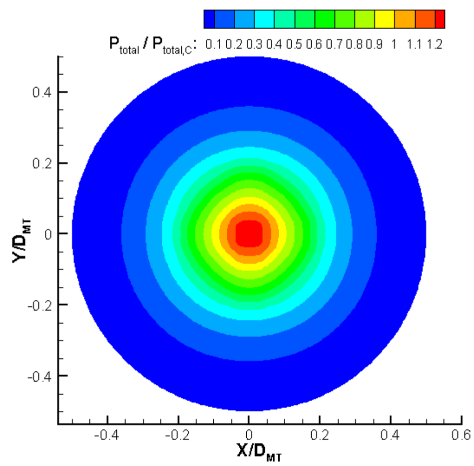

Figure 7-23 4H Experimental Mixing Tube Outlet Total Pressure Contour

Figure 7-24 4H Experimental Mixing Tube Outlet Total Pressure Contour

Because the experimental instrumentation used to collect the total pressure data allowed for the collection of the droplets, the measurement will be indicative of the mixture density (continuous phase and droplets) and not just the continuous phase density. This required the author to account for the contributions of the discrete phase in the computational cases. This was done by calculating an equivalent pressure change produced by an isentropic deceleration of the droplets using Equation 7-7 which was based off of a pressure correction term presented in [17].

$$\Delta P_{total} = B \cdot \Phi_d \cdot w_d \qquad \textbf{7-7}$$

The “B” factor in the equation accounts for the fact that the discrete phase will not transfer all of its momentum to the continuous phase before impacting the instrument’s inner walls. The value of this factor was set to 0.5 for this research, as suggested in literature [17], for situations where not all of the momentum is exchanged to the continuous phase. This factor is a constant because particle drag force is proportional to particle momentum. The product of the remaining variables in Equation 7-7 represent the momentum flux of the discrete phase entering the instrument’s sampling area. Looking at the spray cases with only two spray nozzles operating (2L and 2H) the change in total pressure caused by the discrete phase is located at points on the symmetry plane (Line 45° clockwise from vertical). This causes an unphysical spike in total pressure which is a result of the discrete phase passing the same point on the plane every time step which doesn’t occur experimentally. For the cases where four spray nozzles were operating (4L and 4H) the total pressure plots showed very good qualitative agreement between experimental and computational results in both the core and secondary flow regions. In order to quantitatively compare experimental and computational contours, an outlet total pressure contour error was used (See Equation 7-8).

$$\sigma_{OTP} = \frac{\overline{RSME(P_{total})}_{MW}}{P_{total,C}} \qquad \textbf{7-8}$$

The contour error was calculated separately for the region with spray flow ($r/r_{MT} < 0.4$), and the region without spray flow ($r/r_{MT} > 0.4$). These values were summarized for all spray cases and the no spray case in Table 7-5.

Table 7-5 Outlet Total Pressure Contour Error

Case	σ_{OTP} (%) ($r/r_{MT} < 0.4$)	σ_{OTP} (%) ($r/r_{MT} < 0.4$)
No Spray	2.8	2.4
2L	10.1	2.6
2H	11.4	2.0
4L	5.8	3.5
4H	5.5	3.1

The results of total pressure contour error show that in the spray region, the cases with two nozzles operating shown large discrepancies between experimental and computational contours. This result could indicate that for these cases, Equation 7-7 is over estimating the exchange of momentum from the discrete phase to the continuous phase, resulting in an over calculated total pressure change. The cases with four spray nozzles operating display approximately half the error in the spray region as those with two spray nozzle operating. One key observation is that for the 4H case, the total pressure contour (Figure 7-24) doesn't display the spikes that are seen in the 2H case (Figure 7-20). Since the spray injection characteristics are identical for both cases, the author believes that this phenomenon is a result of the different continuous phase flow fields altering the particle trajectories. In looking at the no spray region, the contour error is approximately the same for the no spray case as for the spray cases. This leads the author to believe that the contour error is mainly a result of the turbulence models inability to accurately predict the continuous phase flow field as discussed in Section 7.1.

7.5 Mixing Tube Outlet Temperature Contours

Following the data collection procedure discussed in Section 3.5.3, and using the gas temperature probe described in Section 3.9, the outlet temperature contours for all spray cases were produced and compared to their computational equivalents (See Figure 7-25 to Figure 7-32).

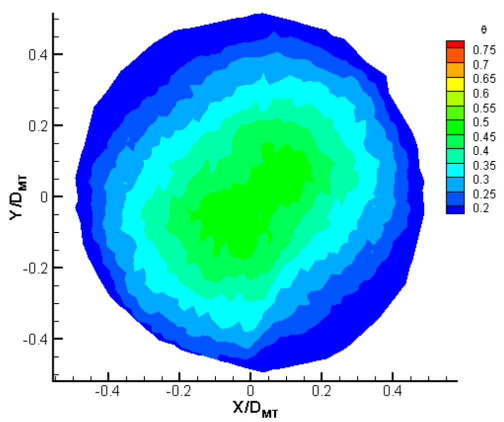

Figure 7-25 2L Experimental Mixing Tube Outlet Temperature Contour

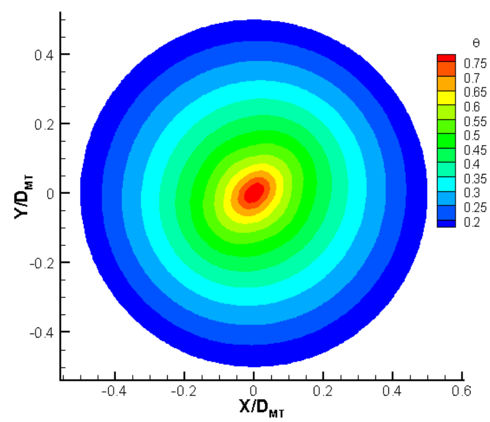

Figure 7-26 2L Computational Mixing Tube Outlet Temperature Contour

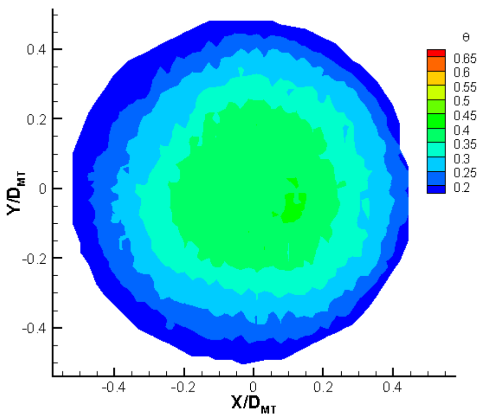

Figure 7-27 2H Experimental Mixing Tube Outlet Temperature Contour

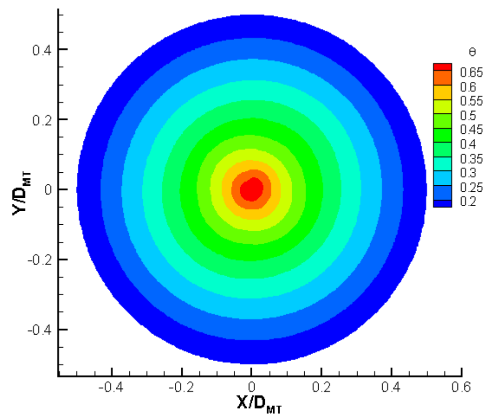

Figure 7-28 2H Computational Mixing Tube Outlet Temperature Contour

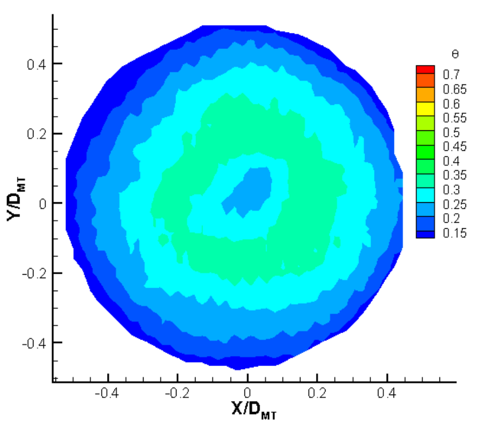

Figure 7-29 4L Experimental Mixing Tube Outlet Temperature Contour

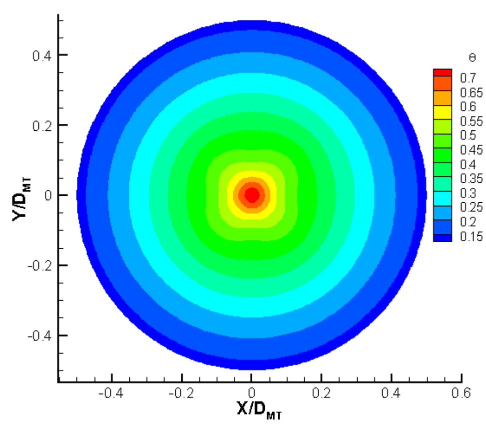

Figure 7-30 4L Computational Mixing Tube Outlet Temperature Contour

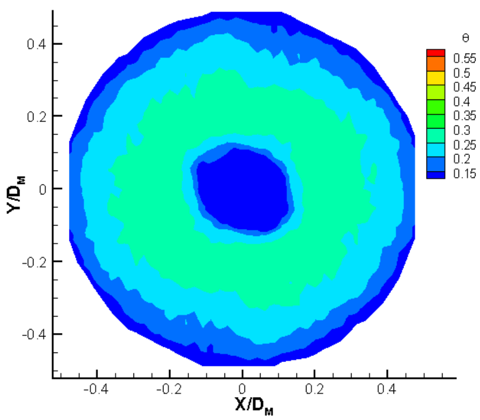

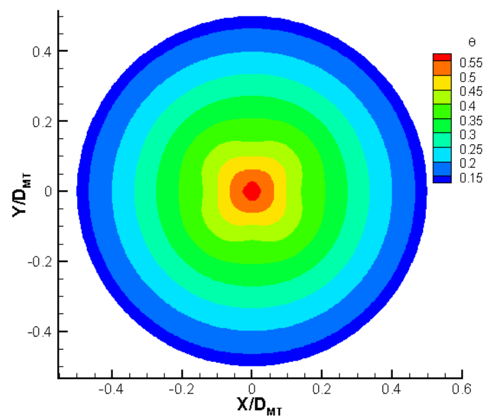

Figure 7-31 4H Experimental Mixing Tube Outlet Temperature Contour

Figure 7-32 4H Computational Mixing Tube Outlet Temperature Contour

Qualitatively comparing the experimental and computational results, it appears that there is good agreement in the outer region of the contour where there is no spray flow ($r/r_{MT} > 0.4$). In all cases, the peak core temperature is not accurately measured by the probe. This claim is made due to the imbalance of energy between the inlet and outlet of the mixing tube for the experimental cases. Even for the lowest mass ratio case (2L, Mass Ratio Z=5%) the experimental core temperature measurement is 33% lower than that calculated computationally. This measurement error is expected because the diameter of the separating disc (1.8 cm) shown in Figure 3-22 is approximately the same size as the high temperature core. Even if the temperature measurement was unaffected by the spray, it would still average out the peak temperature through mixing. The error in the region where there is spray flow ($r/r_{MT} < 0.4$) appears to be increasing with the mass ratio. For the highest mass ratio case (4H, Mass Ratio Z=15%), the entire core region of the flow displays a measurement which is representative of the discrete phase temperature (See Figure 7-33).

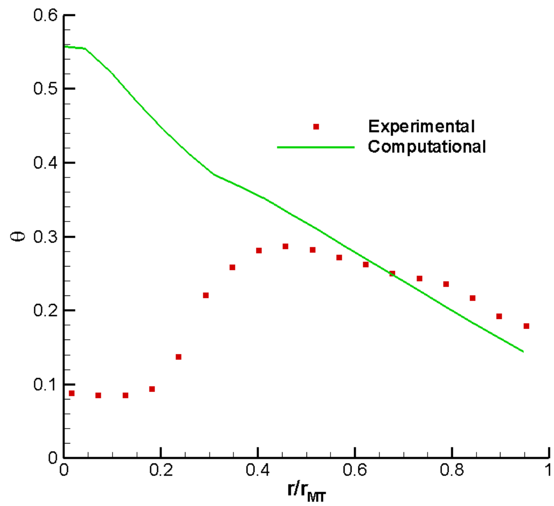

Figure 7-33 4H Temperature Profile Comparison

These results agree with the hypothesis of temperature probe limitations discussed in Section 3.9. It is apparent through comparison of experimental and computational outlet temperature contours that the gas temperature probe is not well suited for the magnitude of spray flux experienced in these cases. In order to quantitatively compare the experimental and computational data the outlet temperature contour error was calculated each spray case using Equation 7-1 and summarized in Table 7-6.

Table 7-6 Outlet Temperature Contour Error

Case	σ_{OT} (%) $(r/r_{MT} < 0.4)$	σ_{OT} (%) $(r/r_{MT} > 0.4)$
No Spray	5.4	7.4
2L	14.6	3.4
2H	15.0	1.5
4L	21.8	1.9
4H	22.8	2.3

As seen in the qualitative comparison, the contour error increased in the spray flow region ($r/r_{MT} < 0.4$) with increases in mass ratio. Interestingly, an opposite effect occurred for the region with no spray flow. Upon the introduction of spray flow, the core flow experiences secondary, non-isothermal shear layers caused by momentum and energy exchange with the continuous phase. The increased mixing caused by these secondary shear layers was thought to be the cause of the profile error improvement.

7.6 Mixing Tube Wall Pressure Contours

Mixing tube wall pressure data was collected for a no spray case and all four spray cases shown in Table 5-5. These results were plotted and compared to their computational equivalents in Figure 7-34.

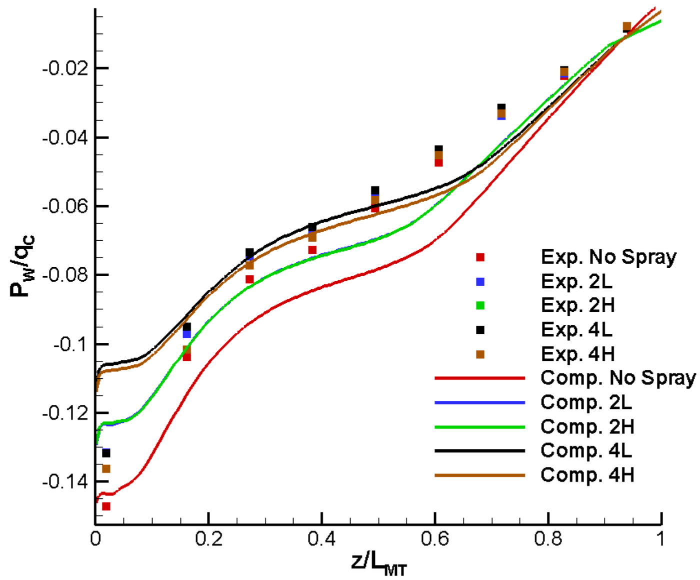

Figure 7-34 Mixing Tube Wall Pressure Comparison

The experimental data suggests that the introduction of spray has minor effects on the mixing tube wall pressure contour. The largest discrepancies lie in the first couple of data points after the bell mouth inlet ($z/L_{MT} = 0$). Through qualitative comparison it appears that for the cases where two nozzles are operating (2L & 2H) there is the best agreement with experimental data. For the cases with four nozzles operating (4L & 4H) the discrepancy between the first points after the bell mouth inlet are relatively large. The deviation in computational contours between cases leads the author to believe that the turbulence model is incorrectly accounting for the interaction mechanics between the droplets and continuous phase. The fact that there is better agreement for certain nozzle configurations and mass ratios is thought to be a coincidence and in no way an indication of improved model accuracy. In order to quantitatively compare experimental and computational results, mixing tube wall pressure contour errors were calculated and summarized in Table 7-7.

Table 7-7 Mixing Tube Wall Pressure Contour Error

Case	σ_{WP} (%)
No Spray	1.07
2L	0.74
2H	0.72
4L	0.73
4H	0.83

As seen through qualitative comparison, all spray cases display less contour error than the no spray case. Although it was stated that this may be coincidental, the author believes that this reduction in error still provides confidence in the other results presented throughout Chapter 7.

7.7 Mixing Tube Wall Temperature Contours

Mixing tube wall temperature data was collected for a no spray case and all four spray cases shown in Table 5-5. These results were plotted and compared to their computational equivalents in Figure 7-35.

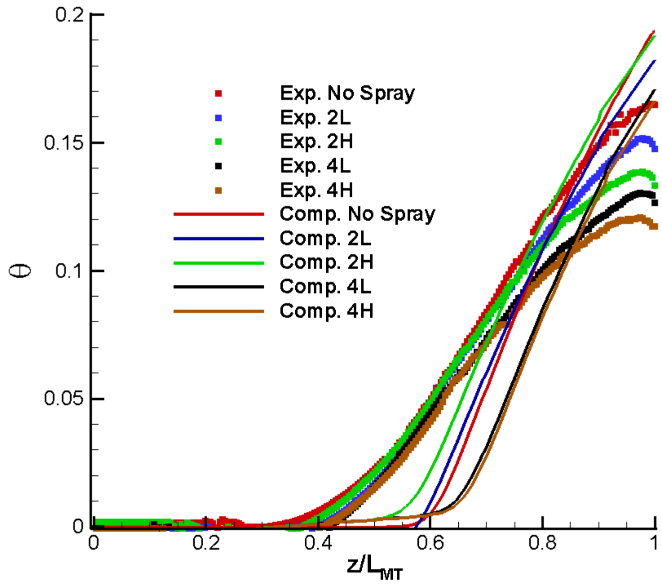

Figure 7-35 Mixing Tube Wall Temperature Contour Error

It should be noted that each line of mixing tube temperature was taken in phase with the spray injection location. Through qualitative comparison it is seen that for all computational cases the rate of jet spread to the wall is under predicted. In comparing the experimental data, the contours of mixing tube wall temperature display very similar values until approximately 60% of the mixing tube length. At this point, they deviate and show maximum values which are indicative of their respective mass ratios. In looking at the computational results, the maximum temperatures for the cases where two nozzles are operating (2L & 2H) show counterintuitive values. In the case where the mass ratio is larger (4H) the maximum mixing tube temperature is larger than for the lower mass ratio case (4L). This is thought to be a result of the different injection velocities between cases. Since the 4H case has a higher injection velocity, the particles will have deeper core penetration, resulting in less cooling in the shear layer. In the real case, the increased relative velocity likely increases particle breakup and decreases the core penetration. Since the same particle distribution was used for both computational cases, this phenomenon is not correctly modeled. In order to quantitatively compare experimental and computational results, mixing tube wall temperature contour errors were calculated and summarized in Table 7-8.

Table 7-8 Mixing Tube Wall Temperature Contour Error

Case	σ_{WT} (%)
No Spray	1.22
2L	1.09
2H	1.37
4L	1.65
4H	1.66

These results show that for all spray cases, except the 2L case, the contour error is larger than that of the no spray case. As previously discussed in Section 7.1.4, accurately predicting this contour is very difficult considering all of the factors that contribute to its error. These include; jet mixing, inlet flow separation, particle evaporation percentage, etc. For these reasons the author feels that the increases in contour error observed will not have detrimental effects on the other results presented in Chapter 7.

7.8 Back Pressure Coefficient

One main objective of this research was to determine the effects or spray flow on air-air ejector performance. One way of quantifying this is with a comparison of back pressure coefficients. The back pressure coefficients for all experimental and computational cases were summarized in Table 7-9.

Table 7-9 Back Pressure Coefficient Comparison

Case	Mass Ratio Z (%)	Experimental C_{bp}	Computational C_{bp}	% Difference
No Spray	0	0.717	0.721	0.6
2L	5	0.729	0.724	0.7
2H	7	0.733	0.726	1.0
4L	11	0.735	0.727	1.1
4H	15	0.748	0.733	2.0

It is shown in Table 7-9 that as the mass ratio increases, the percent difference between experimental and computational back pressure coefficient increases as well. This can be expected since any feature of the computational spray that is being modeled incorrectly will exacerbate the error in back pressure calculation.

It was discovered through performing an ideal analytical 1D solution for the nozzle control volume (See Appendix A.9 for program) that there are two counteracting variables that affect the back pressure coefficient. The first is the percent momentum exchange between the discrete and continuous phase and the other is the evaporated spray mass. Because the continuous phase is accelerating through the nozzle, there will be a relative velocity between the phases as they cross the nozzle exit plane. This means that the only a percentage of the total momentum that will be exchanged has done so by the nozzle exit. The larger this percentage is, the higher the back pressure must be to drive the flow, assuming that the mass flow is constant. There are many factors that determine the magnitude of this percentage, these include: relative velocity (We), relative phase densities (Oh), droplet diameter distribution, etc. The counteracting variable is the evaporated spray mass. As the spray flow evaporates, it cools the continuous phase and the mixture density increases. This results in a reduced jet velocity and dynamic pressure, which results in a lower back pressure. The same factors apply for determining the evaporated spray mass because they account for residence time and evaporation rates. A contour plot was created using the ideal 1D analytical solution provided in Appendix A.9 in order to display the effects of these variables on the back pressure coefficient (See Figure 7-36) This solution was produced using the 4H case (mass ratio Z=15%).

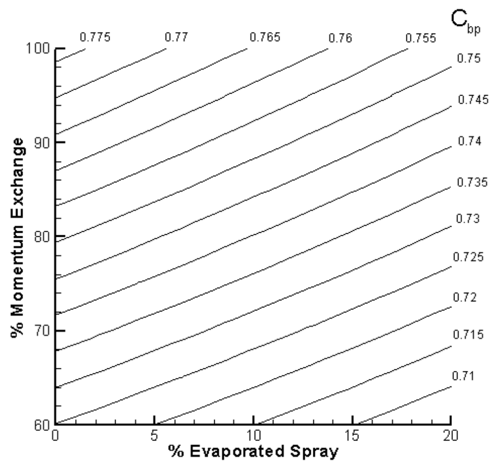

Figure 7-36 4H Analytical Back Pressure Coefficient

One interesting observation from Figure 7-36 is that for an isothermal case (% Evaporated Spray = 0) the backpressure coefficient will always be higher than for a case where flow is being cooled. This observation would suggest that in order to decrease backpressure, one should place the spray nozzles upstream to increase the evaporation time. Using the percent evaporated spray for the 4H computational case (2.5%), one can find graphically, using the C_{bp} found in Table 7-9, that the percent momentum exchange is approximately 66%. The computational data suggests that this value is actually closer to 55%. The discrepancy between the analytical and computational values could be the result of many factors, the main one being that the analytical solution is ideal, and doesn't account for total pressure losses in the device. The experimental data shows higher C_{bp} values than computational for all spray flow cases. Once again, these discrepancies could be partially due to losses experienced in the experimental case, but are likely a result of an inaccurately modeled discrete phase.

Chapter 8
Conclusions

8.1 CFD for Design

Through comparison of experimental and computational results the author concludes that Fluent 6.3.26 can be used as a design tool to simulate the evaporative spray cooling of gas turbine exhaust ejectors. This conclusion is made following the accuracy of computationally predicted spray sampling contours. Although large discrepancies were shown by other comparison methods the author has shown that they were a result of invalid experimental data collection.

8.2 Secondary Traverse

It was found through a mass balance that the error incurred from the axisymmetrical assumption, magnitude of pressure transducer uncertainty, and inaccurate velocity measurements close to the bell mouth inlet resulted in a 5% mass flow error. However, the velocity contour provided a valuable metric for comparing experimental and computational data.

8.3 Mixing Tube Outlet Traverse

By performing a balance of mass, momentum, and energy it was found that the secondary mass flow could be very accurately calculated by taking the difference between the mixing tube outlet mass flow and the nozzle mass flow. This was important for instilling confidence in the experimentally collected continuous phase data.

8.4 Modified Turbulence Model

Through a comprehensive analysis comparing the performance of commercial RANS turbulence models to experimental data it was found that the prediction of centerline decay was significantly under predicted. Following a suggested modification proposed in literature [7] the author wrote a user defined function to account for the increased turbulent viscosity in the mixing layer. By comparing several performance criteria (See Section 7.1) it was determined that the modification outperformed the commercial models.

8.5 Perfect Mixer Model

For both the single phase and spray flow cases, the perfect mixer model was found to over predict the total pumping of air by approximately 20% when compared to experimental data. This was thought to be a result of invalid assumptions required to solve the perfect mixer solution (I.E. no inlet flow separation). The general trends of the results did however give insight into the effects of evaporative spray cooling on air-air ejector performance.

8.6 Droplet Breakup

It was found in preliminary comparison between experimental and computational results that the commercial droplet breakup models available for Fluent 6.3.26 did a poor job for the Weber number regime encountered in this research. For this reason the droplet size distribution should be defined using empirical data which correlates the Sauter mean diameter to the Weber number

8.7 Nozzle Outlet Spray Sampling

It was found that the assumption of negligible evaporation between the injection point and the nozzle outlet plane was invalid. This conclusion was made following the data discussed in

Section 5.2.1, Section 7.2, and Section 7.8. When collecting spray flux data, the location of the selected symmetry plane was important. An effort should be made to locate this plane in a region of low spray mass flux in order to minimize the associated error. Using an iterative method for defining the sampling grid was found to significantly reduce the sampling time for contours where large portion have no spray flow. Through comparison with computational data in section 7.2 it is apparent that the spray sampling probe produces valuable spray flux patternation profiles which give insight into the accuracy of the computational spray model mechanics.

8.8 Mixing Tube Outlet Spray Sampling

By comparing with computational data, the mixing tube outlet collected spray mass flow was measured for the 4L and 4H case within 3.0% and 5.6% respectively. Considering the simplicity of the instrumentation used to obtain this data, this method is very useful for determining the liquid state spray flow crossing a plane. Furthermore, knowing the continuous phase mass flows, one can compute a mass weighted average mixing tube temperature using only this data.

8.9 Mixing Tube Outlet Temperature

Looking at the comparison of experimental and computational data in Section 8.9 it is apparent that the gas temperature instrument used in this research gives inaccurate measurements at even the lowest mass ratio case (2L, mass ratio Z=5%). This was thought to be a result of the following sources of error: localized cooling of the air contributed by the presence of the probe, the increased residence time associated with the recirculation, and the secondary droplet breakup caused by the presence of the separating disc.

8.10 Mixing Tube Outlet Total Pressure

It was found in preliminary data collection that the seven-hole probe ports got clogged with water for all spray cases causing it to give inaccurate measurements. The solution to this problem was to design a large total pressure probe (See Section 3.10). Looking at the results in Section 7.4 it is seen that by using a momentum correction term to account for the spray flux, the computational mixing tube outlet total pressure contour error was approximately 6% (See Table 7-5). It was found that this instrument provided valuable data for contour comparisons, but conclusive velocity measurements could not be inferred due the lack of information about the spray size distribution, mixture density, and phase temperatures.

8.11 Back Pressure Coefficient

It was found in Section 7.8 that the occurrence of spray evaporation in the flow nozzle acted to reduce the back pressure coefficient by reducing the dynamic pressure of the jet. For this reason there is less of a back pressure penalty for a case with evaporation than for an isothermal case.

8.12 Full Scale Comparison

It was found that for a full scale simulation the cooling effectiveness was increased due to the increased droplet surface area and residence time. The evaporated spray mass flow was increased by 5% resulting in a 17% reduction in mass weighted average outlet temperature. For the full scale case, the injection velocity was less significant which resulted in less core penetration. This meant that the droplets didn’t experience the same temperature differentials as in the 1/8th scale model.

Chapter 9
Recommendations

9.1 CFD for Design

It was previously concluded that the methodology shown in this research is valid for simulation of evaporative spray cooling for gas turbine exhaust ejectors. This conclusion relied heavily on the prediction of particle breakup. It is recommended that when using CFD for design purposes that particle breakup be modeled using empirical data rather than commercially available breakup models. The considerations associated with continuous phase flow modeling were thought to have far less of an impact on the overall ejector performance.

9.2 Spray Flow Sampling

Due to the time consuming experimental procedure, a limited number of spray sampling traverses were performed using symmetry assumptions that produced experimental error. It is recommended for future work that the sampling procedure be automated. This would significantly reduce the data collection time and eliminate the need for making symmetry assumptions that incur experimental error.

In order to further validate the accuracy of the spray sampling probe, additional tests should be performed. These would include an isothermal case, cases with higher percentages of evaporated mass flow, cases with lower velocities, etc.

9.3 Spray Injection Location

It was found in Section 7.8 that it was desirable to have as much evaporation occur before the exit of the flow nozzle as possible in order to reduce the back pressure coefficient. It is recommended that as a design feature, the location of the spray nozzles be placed as far upstream of the flow nozzle as possible. This recommendation should only be used for applications where the flow nozzle area reduction is fairly small (I.E. the velocity change between the upstream and jet is small). This is because by locating the nozzles in a lower velocity region, the Weber number will be reduced along with droplet breakup.

For the full scale case, in order to make sure that the droplets reside in the hottest part of the flow, the spray injection location should be placed closer to the centerline than the $1/8^{th}$ scale model.

9.4 Gas Temperature Measurement

It was found that the gas temperature measurement probe used in this research produced invalid measurements for even the lowest mass ratio case (2L, mass ratio Z = 5%). Some recommended modifications for the probe design are as follows: the size of the separating disc should be reduced in order to obtain the measurement resolution required to produce an accurate contour, an effort should be made to make the probe adiabatic in order reduce the temperature loss incurred from its presence. This could be done by coating it with a ceramic or another material with low conductivity. The separating disc should be modified in order to reduce the secondary breakup caused by its presence. This could be done by making it have a conical leading face.

9.5 Turbulence Model

For the modeling of non-isothermal jets it was found in this research and in literature that commercial RANS based turbulence models poorly predict the centerline decay. The author recommends that the turbulent viscosity term be modified as suggested by Abdol-Hamid et al. [7] and shown in Appendix B.7.

References

[1] Blevins, Robert “Applied Fluid Dynamics Hanbook”, *Van Nostrand Reinhold Company Inc.* 1984

[2] White, Frank M. “Fluid Mechanics” Sixth Edition. *McGraw-Hill Companies, Inc* 2008.

[3] Uygun, Murat. Onbaşioğlu, Seyhan. Avci, Suat. “Turbulence Modeling for Computational Fluid Dynamics, Part 1 : Conceptual Outlook” *Journal of Aeronautics and Space Technologies* Vol. 1 Num. 4 pp. 19-26, 2004

[4] Versteeg, H.K. Malalasekera, W. “An Introduction to Computational Fluid Dynamics, The Finite Volume Method” 2nd edition *Pearson Education Limited* 2007

[5] Fluent “Fluent 6.3 User’s Guide” *Fluent Inc.* Sept 29 2006

[6] Klinzing, William P. Sparrow, Ephraim M. “Evaluation of Turbulence Models for External Flows” *Numerical Heat Transfer* Part A 55 pp. 205-228, 2009

[7] Abdol-Hamid, S. Khaled, Pau Paul, S. Massey, Steven J. Elmiligui, Alaa, “Temperature Corrected Turbulence Model for High Temperature Jet Flow” *Journal of Fluids Engineering.* Vol. 126 September 2004.

[8] Koh, S.R. Schroder, W. Meinke, M. “Noises Sources in Heated Coaxial Jets” *Congres Francais de Mechanique* 19 pp. 24-28 August 2009

[9] Georgiadis, Nicholas J. DeBonis, James R. “Navier-Stokes Analysis Methods for Turbulent Jet Flows with Application to Aircraft Exhaust Nozzles” *Progress in Aerospace Sciences* 42 pp.377-418 2006

[10] Salim .M. Salim, and S.C. Cheah “Wall y+ Strategy for Dealing with Wall-bounded Turbulent Flows” *Proceedings of the International MultiConference of*

Engineers and Computer Scientists 2009 Vol II IMECS 2009, March 18 - 20, 2009, Hong Kong

[11] Bosques, Jose Ruben Lebron "Effects of External Conditions on Turbulent Boundary Layers" Masters Thesis *Faculty of Rensselaer Polytechnic Institute* 2007

[12] Molochnikov, V.M., Mikheev ,N.I., and Dushina, O.A. , "Simulation of subsonic flows with separation using the FLUENT program package: software applicability study" *Research Center for Power Engineering Problems,Kazan Scientific Center RAS*, Kazan, *February 12, 2009*

[13] Fluent "Flow over a Cylinder" http://www.philonnet.gr/downloads /ansys/flowlab/ cylinder_tutorial.pdf, *Fluent Inc*. [FlowLab 1.2], April 16, 2007

[14] Kim ,Jongdae, Hangan ,Horia, "Numerical simulations of impinging jets with application to downbursts" *Journal of Wind Engineering and Industrial Aerodynamics* 95 (2007) 279–298

[15] Soh, P. A. 1 and Cheah, S. C. "CFD Studies of Rotating Turbulent Pipe Flows and Jet Flows" *Faculty of Engineering The University of Nottingham*, Selangor Malaysia 2008

[16] Crowe, Clayton et al. "Multiphase Flows with Droplets and Particles", *CRC Press LLC.* 1998.

[17] Gill, L.E. Hewitt, G.F. Hitchon, J.W. Lacey, P.M.C "Sampling Probe Studies of the Gas Core in Annular Two Phase Flow – The Effects of Length on Phase and Velocity Distributions" Chemical Engineering Science, Vol. 18, pp. 525-535, 1963

[18] Pilch, M. Erdman, C.A. "Use of Breakup Time Data and Velocity History Data to Predict the Maximum Size of Stable Fragments for Acceleration-Induced Breakup

of a Liquid Droplet" International *Journal of Multiphase Flow* pp.741-757 Nov-Dec 1987

[19] Hsiao, Mingying. Lichter, Seth. Quintero, Luis G. "The Critical Weber Number for Vortex and Jet Formation for Drops Impinging on a Liquid Pool" *Phys. Fluids* 31 Dec. 1988

[20] Belen'kii, B.M. Evseev, G.A. "Breakup of Drops in the Gas Behind a Shock Wave" *Izvestiya Akademii Nauk SSSR*, Translation, pp.163-165. Mar-Apr 1974

[21] Krzeczkowski, Stefan A. "Measurement of Liquid Droplet Disintegration Mechanisms" *International Journal of Multiphase Flow* Vol. 6 pp.227-239. 1980

[22] Wierzba, A. "Deformation and Breakup of Liquid Drops in a Gas Stream at Nearly Critical Weber Numbers" *Experiments in Fluids* 9 pp. 59-64. 1990

[23] Ng, C.L. Sankarakrishnan, R. Sallam K.A. "Bag Breakup of Non-Turbulent Liquid Jets in Crossflow" International *Journal of Multiphase Flow* 34 pp. 241-259. 2008

[24] Hsiang, L.P. Faeth, G.M. "Near Limit Drop Deformation and Secondary Breakup" International Journal of Multiphase Flow Vol. 18. No. 5 pp.635-652, 1992

[25] Taylor, G.I. "The Shape and Acceleration of a Drop in a High Speed Air Stream" *Technical Report, Scientific Papers of G.I. Taylor* 1963

[26] Varga, Christopher M., Lasheras, Juan C., Hopfinger, Emil J. "Atomization of a Small Diameter Liquid Jet by a High Speed Gas Stream" *Department of Mechanical and Aerospace Engineering, University of California*. 2003

[27] Reitz, R.D. "Mechanisms of Atomization Processes in High-Pressure Vaporization Sprays" *Atomization and Spray Technology* pp. 309-337. 1987

[28] Shuen, J.S. Yang, Virog. Hsiao, C.C. "Combustion of Liquid-Fuel Droplets in Supercritical Conditions" *Combustion and Flame* 89 pp. 299-319 1992

[29] Castanet, G. Delconte, A. Lemoine, F Mees, Loïc. Gréhan, G. "Evaluation of Temperature Gradients Within Combusting Droplets in Linear Stream Using Two Colors Laser-Induced Fluorescence" *Experiments in Fluids* 39 pp 431-440 2005

[30] Brown, Wilbur K. Wohletz, Kenneth H. "Derivation of the Weibull Distribution Based on Physical Principals and its Connection to the Rossin-Rammler and Log-Normal Distributions" *Journal of Applied Physics* Vol. 78, No.4, pp. 2758-2763, August 15th 1995.

[31] Schleicher, Eckhard. Jose da Silva, Marco. Hampel, Uwe. "New Developments in Fast Needle Probe Sensors for Multiphase Flow Measurements" *Institute of Safety Research* Annual Report, 2005

[32] Prasser, H.M. Böttger, A. Zschau, J. Gocht, T. "Needle Shaped Conductivity Probes with Integrated Micro-Thermocouple and Their Application in Rapid Condensation Experiments with Non-Condensable Gases" *Kerntechnik 68* pp. 114-120, 2003

[33] Wang, Xiaohua. Zhu, Chao. "Concentric Evaporating Spray Jets in Dilute Gas-Solid Pipe Flows" *Powder Technology* 129 pp.59-71 2003

[34] Buchanan, Scott. J. "Analysis of Heating and Vaporization of Feed Droplets in Fluidized Catalytic Cracking Riser" *Industrial & Engineering Chemistry Research* 33 pp.3104-3111, 1994

[35] Wang, Yuzhang. Li, Yixing. Weng, Shilie. Su, Ming "Experimental Investigation on Humidifying Performance of Counter Flow Spray Saturator for Humid Air Turbine Cycle" *Energy Conservation and Management* 48 pp. 756-763, 2007

[36] Li, Yixing. Wang, Yuzhang. Weng, Shilie. Wang, Yonghong " Development of a New Temperature Measurement System For Gas-Liquid Flow in Spraying Field" *Experimental Thermal and Fluid Science* 31 pp.917-924, 2007

[37] Abbiss, J.B. Chubb, T.W. Pike, E.R. "Laser Doppler Anemometry" *Optics and Laser Technology*, December 1974

[38] Bach, Fr.-W. Möhwald, K. Engl, L. Dröβler, B. Hartz, K. "Particle Image Velocimetry in Thermal Spraying" *Advanced Engineering Materials,* 8, No.7, 2006

[39] Heitor, M.V. Whitelaw, J.H. "Velocity, Temperature, and Species Characteristics for the Flow in a Gas Turbine Combustor" Combustion and Flame 64: pp 1-32, 1986

[40] Kennedy, I.M. Kent J.H. "Measurement of a Conserved Scalar in Turbulent Jet Diffusion Flames" *Colloquium on Turbulent-Combustion Interactions* 2006

[41] Zahng, G.J. Ishii, M. "Isokinetic Sampling Probe and Image Processing System for Droplet Size Measurement in Two-Phase Flow" International Journal of Heat and Mass Transfer. Vol 38, No. 11, pp. 2019-2027, 1995

[42] Dussourd, J.L. Shapiro, A.H. "A Deceleration Probe for Measuring Stagnation Pressure and Velocity of a Particle-Laden Gas Stream" *Heat Transfer and Fluid Mechanics Institute*, 1955

[43] Mizutani, Yukio. Yasuma, Genshi. Katsuki, Masashi "Stabilization of Spray Flames in a High Temperature Stream" *Symposium on Combustion* Vol. 16, Issue 1, pp. 631-638, 1977

[44] Lee, A. Law, C.K. "Gasification and Shell Characteristics in Slurry Droplet Burning" *Combustion and Flame* 85 pp 77-93 1991

[45] Devore, Jay L. "Probability and Statistics for Engineering and the Sciences" Seventh Edition, Thompson Learning Inc. 2008

[46] Incorpera, Frank P. Dewitt, David P. Bergman, Theodore L. Lavine, Adrienne S. "Fundamentals of Heat and Mass Transfer" Sixth Edition *John Wiley & Sons* 2007

[47] Birk, A.M. "HGWT info and Procedures" *Queens Internal Document* May 2010

[48] Chen, Qi "Performance of Air-Air Ejectors with Multi-Ring Entraining Diffusers" *PHD Thesis, Faculty of Mechanical Engineering, Queens University*, January 2008

[49] BETE "P66 Spray Nozzle Specification Sheet" BETE http://www.bete.com/pdfs/BETE_P-metric.pdf 2007

[50] Omega, "K-Type Thermocouple Specification Sheet" http://www.omega.com / temperature/Z/pdf/z204-206.pdf. 2005

[51] Omega, "PX Series Pressure Transducer Specification Sheets" http://www.omega.com/Pressure/pdf/PX139.pdf. 2010

[52] Omega, "PGC Series Pressure Gauge Specification Sheets" http://www.omega.com/Pressure/pdf/PGC.pdf, 2009

[53] Kilotech "KLE Series Specification Sheet" http://www.kilotech.com /index.php?id=398, 2011

[54] Kilotech "KWS-301 Specification Sheet" http://www.kilotech.com /index.php?id=362, 2011

[55] Gerner, A.A. Maurer, C.L. Gallington, R.W. "Non-Nulling Seven-Hole for High Angle Flow Measurement" *Experiments in Fluids* 2 pp. 95-103. 1984

[56] Crawford, James "Design and Calibration of Seven Hole Probes for Flow Measurement" Msc. Thesis, Department of Mechanical and Materials Engineering, Queens University, 2011

[57] Flir " Thermacam SC1000 Users Manual" http://www.flir.com/uploadedFiles /CVS /Markets/Legacy/Documents/ThermaCAM%20SC1000%20Inframetrics.pdf , 2009

[58] Brennen, Christopher E. "Fundamentals of Multiphase Flows", *Cambridge University Press.* 2005

[59] Richman, J.W. Azad, R.S. "Developing Turbulent Flow in Smooth Pipes" *Advances in Applied Science Research* 28 pp. 419-441 1973

[60] Moffat, Robert "Describing the Uncertainties in Experimental Results" Experimental Thermal and Fluid Science Vol. 1 Issue 1 pp. 3-17 January 1988

[61] Gray, Donald D. "A First Course in Fluid Dynamics for Civil Engineers", *Water Resources Publications.* 2000

[62] Ouyang, Shan. Yeasmin, Hasina "A Pressurized Drop-Tube Furnace for Coal Reactivity Studies" *Review of Scientific Instrumentation* Vol. 69 Num. 8, August 1998

[63] Southard, John,"Flow Past a Sphere II: Stokes' Law, The Bernoulli Equation, Turbulence, Boundary Layers, Flow Seperation" *An Introduction to Fluid Motions, Sediment Transport, and Current-Generated Sedimentary Structures,* Pg. 73, 2008, MIT OpenCourseWare

[64] Vyas, B.D., Kar, S. Study of Entrainment and Mixing Process for an Air to Air Jet Ejector. *2nd Symposium on Jet Pumps and Ejectors and Gas Lift Techniques,* 1975

Appendix A

Experimental

A.1 Mixing Tube Alignment

Alignment of the mixing tube with respect to wind tunnel axis was done using a laser pointer system. A 6.4 mm thick aluminum plate was modified to be bolted to the test section flange (See Section 3.6). A 19.1 mm hole was drilled and reamed in the center of the plate and a drill bushing was press fit in to be representative of the wind tunnel axis. The laser pointer was placed in the drill bushing, and the centerline was established by the laser beam. Two T-brackets were designed to be placed on the inlet and outlet face of the mixing tube. The inlet T-bracket had a small hole in its center for which the laser beam was required to pass through. The outlet T-bracket had a target point at its center which the laser beam was required to hit. The mixing tubes height and orientation were adjusted until these two requirements were met (See Figure A-1).

Figure A-1 Mixing Tube Alignment Rig

All device alignment was done while the wind tunnel was turned off. The magnitude of misalignment after the effect of thermal expansion was determined to be approximately +/- 1°. This value was determined by taking measurements of the distance between four nozzle flange quadrant points and four mixing tube inlet quadrant points.

A.2 Uncertainty Analysis

The uncertainty of the experimental instrumentation used in this research is summarized in Table 3-4. In this section Engineering Equation Solver was used to propagate measurement uncertainties using the partial derivative method [60].Throughout this analysis the uncertainty in pressure measurement for the seven-hole probe is taken as the root sum square of the calibration uncertainty and transducer uncertainty.

A.2.1 Inlet Traverse

The uncertainty in seven-hole probe z-wise velocity measurement was calculated and displayed for one sample point assuming a human alignment error of 2º (See Figure A-2).

Variable±Uncertainty	% of uncertainty
ρ = 0.513±0.002 [kg/m^3]	
P_{Static} = 5000±135 [Pa]	6.89 %
T = 450± 9 [C]	93.11 %

Variable±Uncertainty	% of uncertainty
V = 85.9±1.0 [m/s]	
q = 1893±44 [Pa]	95.77 %
ρ = 0.513±0.002 [kg/m^3]	4.23 %

Variable±Uncertainty	% of uncertainty
w = 85.8±1.0 [m/s]	
θ = 2±2 [deg]	1.06 %
V = 85.9±1.0 [m/s]	98.94 %

Figure A-2 Inlet Traverse Z-Wise Velocity Uncertainty

Using the uncertainty in Z-wise velocity and density for all acquired points, the uncertainty for the integrated mass flow was calculated to be 1.32 +/- 0.02 kg/s. This calculation assumes negligible error in the cross-sectional area of the inlet and the "K" factor because the mass flow was compared to a nozzle outlet traverse.

A.2.2 Nozzle Exit Traverse

The uncertainty in the Z-wise velocity was calculated and displayed for one sampled point in Figure A-5 assuming a human alignment uncertainty of 2º.

Variable±Uncertainty	% of uncertainty
ρ = 0.488±0.006 [kg/m^3]	
P_{static} = 10±20 [Pa]	0.03 %
T = 450±9 [C]	99.97 %

Variable±Uncertainty	% of uncertainty
V = 166±2 [m/s]	
q = 6684±154 [Pa]	66.39 %
ρ = 0.488±0.008 [kg/m^3]	33.61 %

Variable±Uncertainty	% of uncertainty
w = 166±2 [m/s]	
θ = 2±2 [deg]	0.74 %
V = 166±2 [m/s]	99.26 %

Figure A-3 Nozzle Exit Traverse Velocity Uncertainty

Using the uncertainty in Z-wise velocity and density for all acquired points, the uncertainty in the integrated mass flow was calculated to be 1.49 +/- 0.03.

A.2.3 Secondary Traverse

The uncertainty in the secondary velocity normal to the frustum face (w_s) was calculated and displayed for one sampled point in Figure A-4 assuming a human alignment uncertainty of 2º.

Variable±Uncertainty	% of uncertainty
ρ = 1.184±0.008 [kg/m^3]	
P_{Static} = -88±22 [Pa]	0.10 %
T = 25±2 [C]	99.90 %

Variable±Uncertainty	% of uncertainty
V = 12.2±1.5 [m/s]	
q = 88±22 [Pa]	99.93 %
ρ = 1.184±0.008 [kg/m^3]	0.07 %

Variable±Uncertainty	% of uncertainty
w_s = 12.2±1.5 [m/s]	
θ = 2±2 [deg]	0.01 %
V = 12.2±1.5 [m/s]	99.99 %

Figure A-4 Secondary Inlet Normal Velocity Uncertainty

Looking at Figure A-4 it is apparent that a significant amount of uncertainty is contributed by the transducer, which is an indication that it was under ranged. Using the uncertainty in velocity normal to the frustum face and density for all acquired points, the uncertainty for the integrated mass flow was calculated to be 1.56 +/- 0.20 kg/s. As seen from this calculation the under ranging of the pressure transducer incurred approximately 13% uncertainty on the secondary mass flow calculation which concurs with the discrepancy found between its values in Table 5-2 and Table 5-3.

A.2.4 Mixing Tube Outlet Traverse

The uncertainty in the Z-wise velocity was calculated and displayed for one sampled point in Figure A-5 assuming a human alignment uncertainty of 2º.

Variable±Uncertainty	% of uncertainty
$\rho = 0.712 \pm 0.003$ [kg/m^3]	
$P_{Static} = 10 \pm 20$ [Pa]	0.24 %
$T = 223 \pm 4$ [C]	99.76 %

Variable±Uncertainty	% of uncertainty
$V = 76.4 \pm 1.3$ [m/s]	
$q = 2080 \pm 68$ [Pa]	98.50 %
$\rho = 0.712 \pm 0.003$ [kg/m^3]	1.50 %

Variable±Uncertainty	% of uncertainty
$w = 76.4 \pm 1.3$ [m/s]	
$\theta = 2 \pm 2$ [deg]	0.54 %
$V = 76.4 \pm 1.3$ [m/s]	99.46 %

Figure A-5 Mixing Tube Outlet Z-wise Velocity Uncertainty

Using the uncertainty in Z-wise velocity and density for all acquired points, the uncertainty in the integrated mass flow was calculated to be 3.00 +/-0.05 kg/s.

A.2.5 Spray Nozzle Input Mass Flow

The sources of uncertainty on the calculation of spray nozzle input mass flow rate were the readability of the pressure gauge (calibration and in situ), the calibration time uncertainty (1s), and the calibration scale uncertainty. These uncertainties were converted to equivalent uncertainties in kg/s for the validation, 2L, 4L, 2H, and 4H cases (See Table A-1) and their root sum square error was calculated.

Table A-1 Spray Nozzle Input Mass Flow Uncertainty

Source	Uncertainty (kg/s)	
	2L, 4L Cases	Validation, 2H, 4H Cases
Pressure Gauge In-Situ Readability	8.9×10^{-4}	6.9×10^{-4}
Pressure Gauge Calibration Readability	8.9×10^{-4}	6.9×10^{-4}
Calibration Time Uncertainty	3.0×10^{-4}	8.1×10^{-4}
Calibration Scale Uncertainty	4.2×10^{-6}	8.3×10^{-6}
Total	1.3×10^{-3}	1.3×10^{-3}

A.2.6 Spray Sampling

The quantifiable sources of uncertainty for the spray sampling were the sampling area, sampling time and the scale readability. These values were converted to equivalent average uncertainties in kg/m^{2}s for the spray flow validation, 4L, and 4H cases and summarized in Table A-2.

Table A-2 Spray Sampling Mass Flux Uncertainty

Source	Uncertainty (kg/m^{2}s)		
	Validation Case	4L Case	4H Case
Sampling Area	0.61	0.53	0.58
Sampling Time	0.22	0.19	0.21
Scale Readability	0.06	0.06	0.06
Total	0.65	0.57	0.62

Using these flux uncertainties, the average uncertainty in collected spray mass flow was calculated for the validation, 4L, and 4H cases and summarized in Table A-3.

Table A-3 Spray Sampling Mass Flow Uncertainty

Case	Collected Mass Flow Rate Uncertainty (kg/s)
Validation	9.9×10^{-3}
4L	6.1×10^{-3}
4H	7.6×10^{-3}

A.3 Spray Nozzle Calibration

The spray nozzle calibration procedure consisted of varying the spray nozzle driving pressure and collecting samples in a ten liter container. The driving pressure was varied in approximately 14 kPa increments between 100 kPa and 300 kPa (Operating range). In order to reduce the relative magnitude of scale error (+/- 0.05g) and sampling time error (1s) a sample of approximately 3 kg was taken for each driving pressure. The mass flow was calculated for each driving pressure by dividing the sample weight by the sampling time. The mass flow was then graphed with respect to driving pressure (See Figure 3-8)

A.4 BETE Nozzle Spray Distribution

Figure A-6 shows the quoted BETE P66 droplet size characteristics for the spray nozzle driving pressure range used in this research

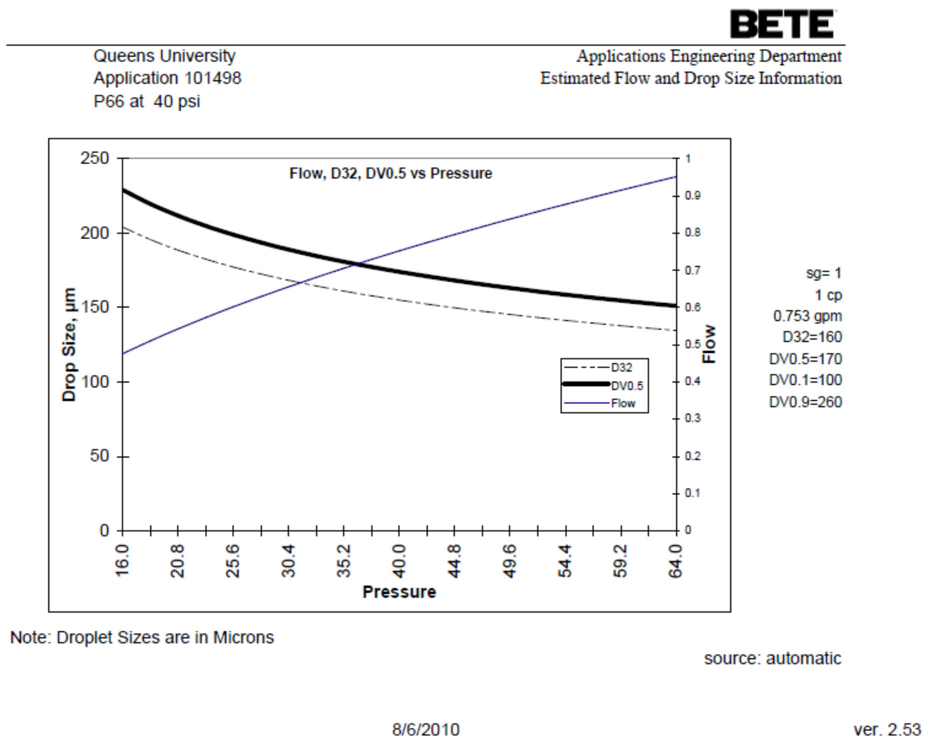

Figure A-6 P66 Spray Characteristics

It should be noted that these values are representative of a nozzle spraying into stagnant atmospheric conditions. For this reason, the Sauter Mean Diameters are much larger than the values used in this research due to the high Weber numbers encountered in the flow nozzle.

A.5 Pressure Transducer Calibration

Pressure transducer calibration was done using a standing water manometer shown in Figure A-7.

Figure A-7 Standing Water Manometer

The water manometer was manually pressurized and attached to a bank of eight tubes in order to calibrate eight transducers simultaneously. The transducer's voltage response was documented for approximately ten even incremental steps through its pressure range. By correlating these voltage outputs to known pressures, a calibration curve was produced using software originally written by Dave Poirier. Every pressure transducer has a slightly different voltage response which is why calibration is important. These calibration curves where then used by the lab view software described in Section 3.3.1 in order to calculate pressure.

A.6 Seven-Hole Probe Calibration

Seven-hole probes provide a cost effective solution for measuring local flow field pressure, velocity magnitude and directionality. This is done by measuring the pressure differential between at least four of the seven pressure ports seen in Figure A-8 (Figures and Equations in this section are from Gerner et al. [55])

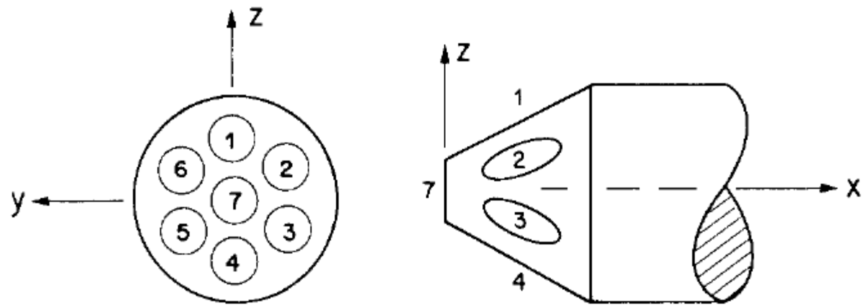

Figure A-8 Seven Hole Probe Port Numbering

The conventions used to describe the directionality of the incident flow vector are shown in Figure A-9.

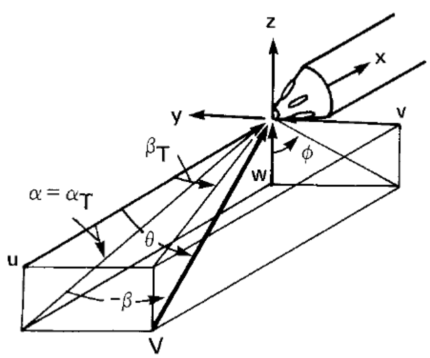

CONVENTIONAL	POLAR	TANGENT
$u = V \cos\alpha \cos\beta$	$u = V \cos\theta$	$\alpha_T = \arctan \frac{w}{u}$
$v = -V \sin\beta$	$v = V \sin\theta \sin\phi$	$\beta_T = \arctan \frac{v}{u}$
$w = V \sin\alpha \cos\beta$	$w = V \sin\theta \cos\phi$	

Figure A-9 Seven Hole Probe Flow Angle Definition

Where: α = pitch, β = yaw, θ = cone, φ = roll

When the probe is oriented with the velocity vector, all seven pressure ports are measuring un-separated flow and are used for calculating the flow variables. For cone angles larger than approximately 30°, the flow on the lee-side of the probe begins to separate [55]. These separated flow measurements are inconsistent and therefore, only the four attached measurements can be used. Depending on the flow angle, there are seven different combinations of used port measurements which requires the definition of angle sectors (See Figure A-10)

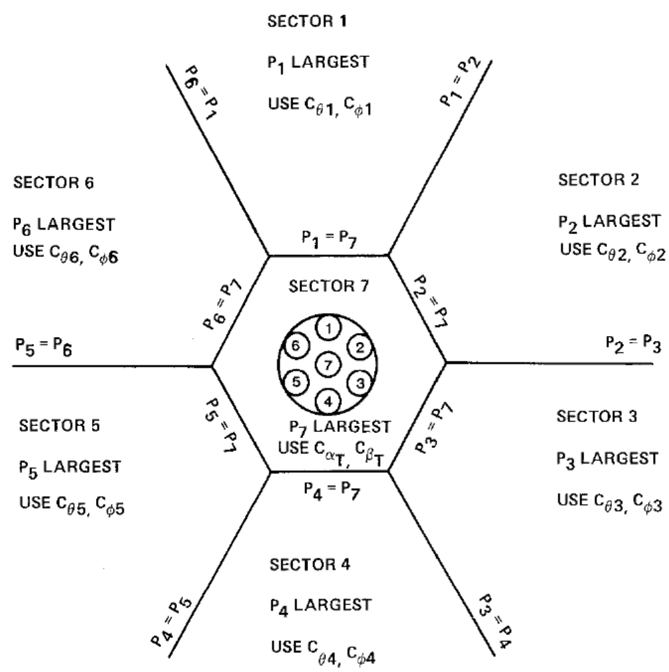

Figure A-10 Seven Hole Probe Angle Sectors

Sector seven is known as the low angle region and is selected if port seven has the highest pressure measurement. For the high angles, the sector is chosen based on the largest peripheral port measurement.

A.6.1 Pressure Coefficients

In order to implicitly solve for flow variables using the differential pressure between ports, non-dimensional pressure coefficients must be defined. This is done by normalizing the pressure differentials by the apparent dynamic pressure (more later) in order to eliminate their dependence on velocity magnitude.

For the low angle region, the flow angle is defined by the pitch and yaw convention. Three pressure coefficients and two conversion coefficients are used to calculate flow directionality (See Equation A-1 to Equation A-5), one to measure total pressure (See Equation A-6), and one to measure dynamic pressure (See Equation A-7).

$$C_{\alpha a} = \frac{P_4 - P_1}{P_7 - \overline{P}_{1-6}} \qquad \textbf{A-1}$$

$$C_{\alpha b} = \frac{P_3 - P_6}{P_7 - \overline{P}_{1-6}} \qquad \textbf{A-2}$$

$$C_{\alpha c} = \frac{P_2 - P_5}{P_7 - \overline{P}_{1-6}} \qquad \textbf{A-3}$$

$$C_{\alpha T} = \frac{1}{3}\left(2C_{\alpha a} + C_{\alpha b} + C_{\alpha c}\right) \qquad \textbf{A-4}$$

$$C_{\beta T} = \frac{1}{\sqrt{3}}\left(C_{\alpha b} + C_{\alpha c}\right) \qquad \textbf{A-5}$$

$$C_o = \frac{P_7 - P_{OL}}{P_7 - \overline{P}_{1-6}} \quad \textbf{A-6}$$

$$C_q = \frac{P_7 - \overline{P}_{1-6}}{P_{OL} - P_{\infty L}} \quad \textbf{A-7}$$

Where: $\overline{P}_{1-6}$ = average of ports 1-6, $P_7 - \overline{P}_{1-6}$ = apparent dynamic pressure, P_{OL} = known reference total pressure, $P_{\infty L}$= known reference static pressure.

For the high angle regions, it is more convenient to define the flow angle by the cone and roll convention. Two pressure coefficients are used to define flow directionality (See Equation A-8 and Equation A-9) one to define total pressure (See Equation A-10) and one to dynamic pressure (See Equation A-11).

$$C_{\theta n} = \frac{P_n - P_7}{P_n - (P_{n-1} + P_{n+1})/2} \quad \textbf{A-8}$$

$$C_{\phi n} = \frac{P_{n-1} - P_{n+1}}{P_n - (P_{n-1} + P_{n+1})/2} \quad \textbf{A-9}$$

$$C_{On} = \frac{P_n - P_{OL}}{P_n - (P_{n-1} + P_{n+1})/2} \quad \textbf{A-10}$$

$$C_{qn} = \frac{P_n - (P_{n-1} + P_{n+1})/2}{P_{OL} - P_{\infty L}} \quad \textbf{A-11}$$

Where: P_n = port of highest pressure

A.6.2 Calibration

Manufacturing limitations make it impossible to create seven-hole probes that are of the exact same geometry. This means that there is a requirement for individual calibration in order to account for geometric effects on the pressure coefficients. The calibration procedure involved rotating the probe through a set of known pitch and yaw angles and measuring the seven port pressure. These values were then used to create fourth order pressure coefficient polynomials for the flow angles (α_T, β_T), total pressure (C_O), and dynamic pressure (C_q) in the form of Equation A-12 (For low angle sector).

$$\begin{aligned} A_i = [&K_1{}^A + K_2{}^A C_{\alpha T} + K_3{}^A C_{\beta T} + K_4{}^A C_{\alpha T}{}^2 + K_5{}^A C_{\alpha T} C_{\beta T} + K_6{}^A C_{\beta T}{}^2 \\ &+ K_7{}^A C_{\alpha T}{}^3 + K_8{}^A C_{\alpha T}{}^2 C_{\beta T} + K_9{}^A C_{\alpha T} C_{\beta T}{}^2 + K_{10}{}^A C_{\beta T}{}^3 + K_{11}{}^A C_{\alpha T}{}^4 + \\ &K_{12}{}^A C_{\alpha T}{}^3 C_{\beta T} + K_{13}{}^A C_{\alpha T}{}^2 C_{\beta T}{}^2 + K_{14}{}^A C_{\alpha T} C_{\beta T}{}^3 + K_5{}^A C_{\beta T}{}^4] \end{aligned} \qquad \textbf{A-12}$$

Where: A_i is one of the flow properties α_T, β_T, C_O, C_q, K is the polynomial coefficients

For the high angle sectors, the angular coefficients $C_{\alpha T}$ and $C_{\beta T}$ are replaced with C_θ and C_{φ}. The value A_i is calculated for each calibration angle and stored in a matrix of the form seen in Equation A-13.

$$\begin{bmatrix} A_1 \\ A_2 \\ \vdots \\ A_m \end{bmatrix} = \begin{bmatrix} 1 & C_{\alpha T1} & C_{\beta T1} & C_{\alpha T1}{}^2 & C_{\alpha T1} C_{\beta T1} & \cdots & \cdots & C_{\beta T1}{}^4 \\ 1 & C_{\alpha T2} & C_{\beta T2} & C_{\alpha T2}{}^2 & C_{\alpha T2} C_{\beta T2} & \cdots & \cdots & C_{\beta T2}{}^4 \\ \vdots & \vdots & \vdots & \vdots & \vdots & & & \vdots \\ 1 & C_{\alpha Tm} & C_{\beta Tm} & C_{\alpha Tm}{}^2 & C_{\alpha Tm} C_{\beta Tm} & \cdots & \cdots & C_{\beta Tm}{}^4 \end{bmatrix} \begin{bmatrix} K_1{}^A \\ K_2{}^A \\ \vdots \\ K_{15}{}^A \end{bmatrix} \qquad \textbf{A-13}$$

Using a Fortran 90 program written by David Poirier, matrix algebra is used to calculate the 15 calibration coefficients for each flow property. In this research, approximately 2000 calibration points were used where the angular increment was 3° and the maximum roll angle was 60°. This calibration grid was chosen following a comprehensive grid sensitivity study performed by James Crawford [56].

Following calibration, these polynomials were used to determine the flow directionality, total pressure, dynamic pressure, and static pressure of arbitrary flow fields. This was done by rearranging Equation A-6 and Equation A-7 for the low angle and Equation A-10 and Equation A-11 for the high angle to solve for total pressure and static pressure.

A.7 Pressure Sampling Sensitivity Study

In order to select an appropriate pressure sampling time for the seven-hole probe, a percent average pressure change was calculated for ten seconds (See Figure A-11).

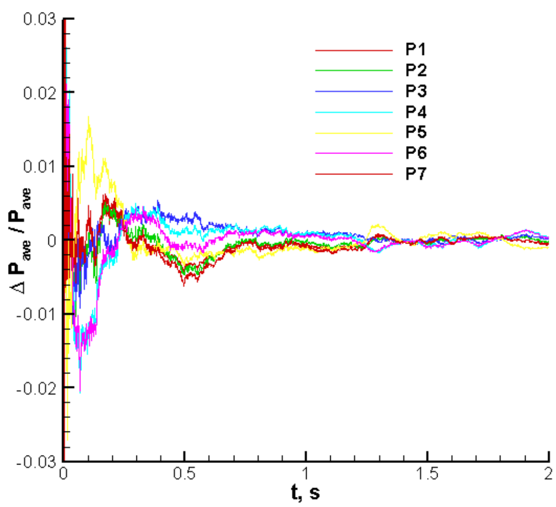

Figure A-11 Percent Average Pressure Change

This data was taken after a rapid change in probe orientation in order to also determine the transient effects on pressure measurements. As seen in Figure A-11 the average pressure changes by less that 0.4% after a sampling time of only 1.5 seconds. Based on these findings, the sampling time used for the duration of this research was two seconds.

A.8 Plane Grid Program

Program Written in “FORTRAN 90” Language

```
PROGRAM OUTLETTRAVERSE
IMPLICIT NONE
!Declare Geometric and Traverse Specifications
REAL*8 :: PIPEDIAMETER = 0.1508125 !Diameter of outlet, value in meters
REAL*8 :: RESOLUTION = 0.001       !X-Y Spacing of traverse, value in meters
!Looping Indices
INTEGER I, J
!Possible Traverse Points
INTEGER*4 NPOINTS
!Store X, Y at each point
REAL*8 X, Y
!Body of Program
NPOINTS = PIPEDIAMETER/RESOLUTION
OPEN(UNIT = 20, FILE = 'xy.txt')
10  FORMAT (F8.5,'     ',F8.5)
DO I = 0, NPOINTS
IF (MOD (I,2) == 0)      THEN
X = - PIPEDIAMETER / 2 + I * RESOLUTION
DO J = 0, NPOINTS
Y = J * RESOLUTION
IF ( (X**2 + (Y - PIPEDIAMETER/2)**2) < ((PIPEDIAMETER/2)**2) ) THEN
WRITE (20, 10) X, Y
END IF
END DO
ELSE
X = - PIPEDIAMETER / 2 + I * RESOLUTION
DO J = 0, NPOINTS
Y = PIPEDIAMETER-(J * RESOLUTION)
IF ( (X**2 + (Y - PIPEDIAMETER/2)**2) < ((PIPEDIAMETER/2)**2) ) THEN
WRITE (20, 10) X, Y
END IF
END DO
END IF
END DO
END PROGRAM OUTLETTRAVERSE
```

A.9 Back Pressure Coefficient Calculator

Program Written in "EES" Language

```
{Boundary Conditions}
T1=470
Ts=15
M1=1.3
Ms=0.198
A1=0.03345061
V1=M1/(rho1a*A1)
M2=rhomix*V2*A2
FZ=51.64
A2p=A1
A2=0.017863417
Vs=2.3
P2=101.599
{Properties}
rho1a=Density(Air,T=T1,P=P1)
rho1s=Density(Water,T=Ts,P=P1)
rho2s=Density(Water,T=99,P=P2)
rho2a=Density(Air,T=T2,P=P2)
rho2h=Density(Steam,T=T2,P=P2)
h1a=Enthalpy(Air,T=T1)
h1s=Enthalpy(Water,T=Ts,P=P1)
h2a=Enthalpy(Air,T=T2)
h2s=Enthalpy(Water,T=99,P=P2)
h2h=Enthalpy(Steam,T=T2,P=P2)
MFa=(M1)/(M1+Ms)
(MFs+MFh)*M2=Ms
{Conservation of Mass}
M1+Ms=M2
{Conservation of Momentum}
P1*1000*A1 + M1*V1 - Ms*Vs = P2*1000*A2p +M2*(MFa+MFh)*V2 +M2*(MFs*percent)*V2 + Fz
{Conservation of Energy}
M1*h1a+Ms*h1s=M2*( (MFa*h2a) +(MFs*h2s)+(MFh*h2h) )
rhomix = 1/ ( (MFa/rho2a) + (MFs/rho2s) + (MFh/rho2h))
V3=V2/0.907
P2Alter=(0.5*rhomix*((V3^2)-(V2^2)))-1000
```

Appendix B

Computational

B.1 Grid Density Sensitivity Study

Two separate grid density sensitivity studies were performed in this research. The first was on the continuous phase solution and the second was on the discrete phase solution.

B.1.1 Continuous Phase

Using the realizable kε model, a grid density study was performed on the fluid domain. The three different mesh densities used in this study included a 0.35, 1.5, and 5 million cell grid. The entire domain was refined between cases, except for wall normal boundary layer mesh density, in order to capture all potential flow feature sensitivities. Some of these include: bell mouth inlet separation, mixing layer resolution, flow reattachment, etc. The effects on mixing tube outlet velocity and temperature are shown in Figure B-1 and Figure B-2 respectively.

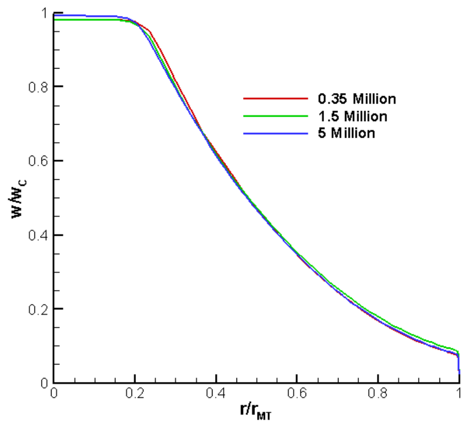

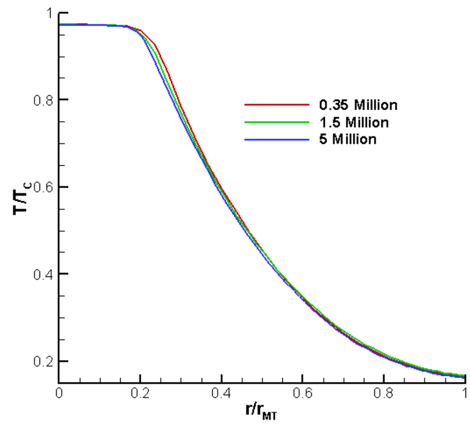

Figure B-1 Continuous Phase Grid Study Velocity Contour

Figure B-2 Continuous Phase Grid Study Velocity Contour

Through qualitative comparison of these two contours it's seen that there is very little change as the mesh density is increased. The only noticeable feature is that there is a slightly wider core region for the 0.35 million grid than the others. The outer regions of the profiles (r/rMT > 0.5) show very good agreement between meshes which leads the author to believe that the bell mouth inlet separation is insensitive to mesh refinement at this level. Because it was anticipated that the discrete phase would require a denser mesh, the 1.5 million cell grid was chosen for subsequent simulations.

B.1.2 Discrete Phase

For the discrete phase sensitivity study, a modified grid was produced with no mixing tube. This was done in order to reduce the simulation time. Once the simulation converged, the mesh was locally refined in the cells with discrete phase source terms not equal to zero. The local refinement function splits each cell into four smaller cells, and was performed twice. The effect of this local refinement on the outlet velocity and temperature profiles is shown in Figure B-3 and Figure B-4 respectively.

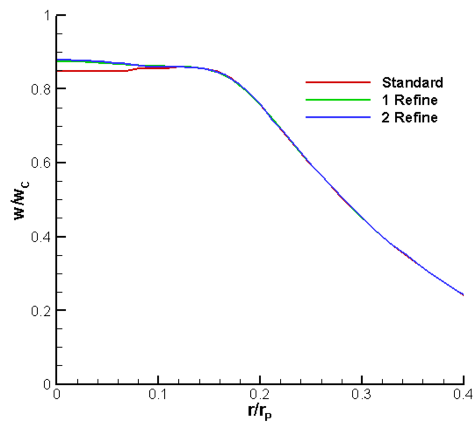

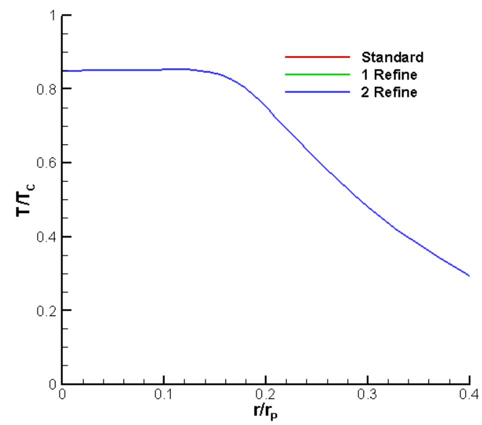

Figure B-3 Discrete Phase Grid Study Velocity Contour

Figure B-4 Discrete Phase Grid Study Temperature Contour

Through qualitative comparison, the only contour that shows any noticeable difference is the velocity. Since this difference only occurs in the core of the flow, this discrepancy is thought to be a result of grid sensitivity on the momentum coupling between the discrete and continuous phase. From these results it was concluded that one level of mesh refinement was sufficient for eliminating grid dependence and was used for subsequent simulations.

B.2 Wall Treatment Sensitivity Study

The effects of near wall treatment were tested for all commercially available models for Fluent 6.3.26. This test was performed because the use of near wall treatments that require the viscous sub-layer (See Section 2.2.2) to be resolved require meshes with significantly more cells than for models where the viscous sub-layer is modeled. In order to determine the location of flow separation and reattachment, the z-wise wall shear stress for each model was summarized in Figure B-5

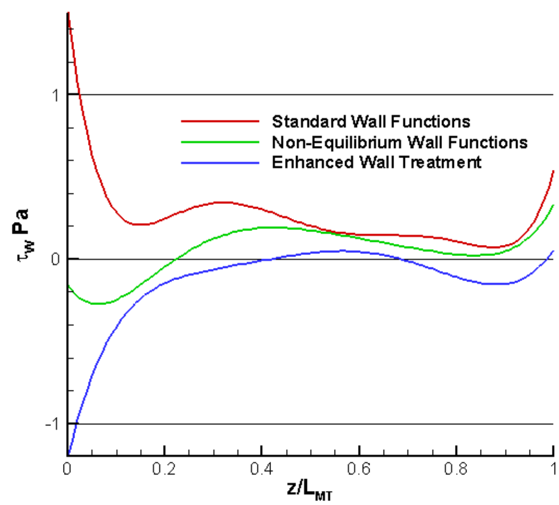

Figure B-5 Mixing Tube Z-Wise Wall Shear Stress

Since the location of flow separation and reattachment are seen graphically as the root of the profile (I.E. where τ_w crosses the zero Pa line) it is apparent that each near wall model predicts radically different secondary flow features. From these results and the literature discussed in Section 2.2.2 the author concluded that the use of the enhanced wall treatment was required for the mixing tube mesh in order to properly capture inlet flow separation.

B.3 Turbulence Intensity Sensitivity Study

Through comparison of experimental and computational data in Section 7.1 it was found that the centerline decay of the jet was under predicted by commercial turbulence models. The author performed a sensitivity study to test the effect of increased turbulence intensity on the jet centerline decay. Two different turbulence intensities were used in this study, the first was 5%, and the other was 20% which is the upper limit of possible values [5]. The mixing tube outlet temperature profiles for these cases are shown in Figure B-6.

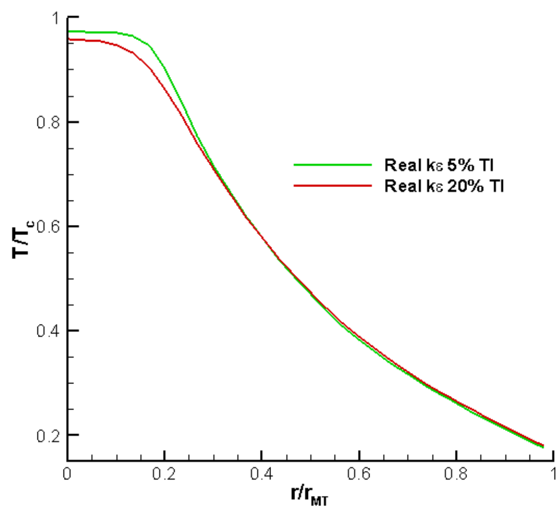

Figure B-6 Turbulence Intensity Study Mixing Tube Outlet Temperature Contour

It is seen in Figure B-6 that by increasing the turbulence intensity defined at the mass flow inlet the centerline decay of the jet was slightly increased, but not as much as was required to match experimental data (See Figure 7-2). This shows that the k-ε turbulence models are quite insensitive to turbulence boundary conditions as discussed in Section 2.2.1. For this reason, a turbulence intensity of 5% was used for the duration of this research.

B.4 Spray Time Step Sensitivity Study

In order to determine the discrete phase models sensitivity to particle time step, four simulations were run with time steps of 2 $x10^{-4}$, 1 $x10^{-4}$, 5 $x10^{-5}$, and 2.5 $x10^{-5}$ seconds. In order to reduce the computational time, a modified mesh with no mixing tube was used. The velocity and temperature profiles at the plenum exit are shown in Figure B-7 and Figure B-8 respectively.

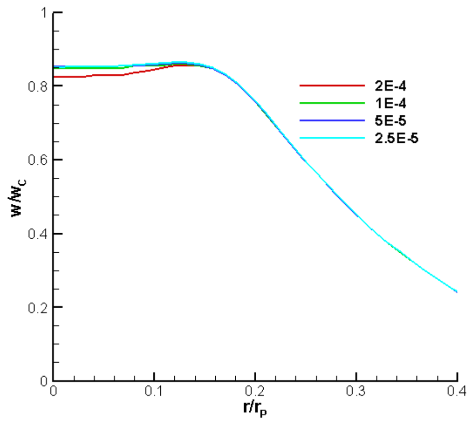

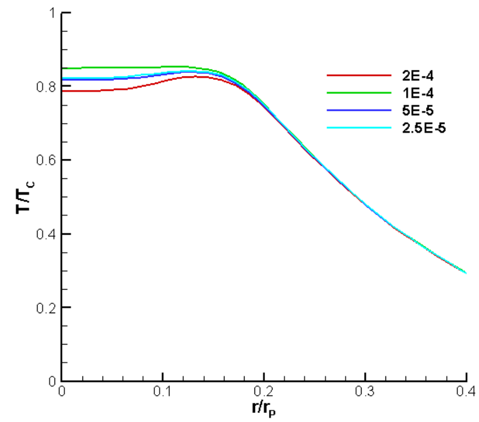

Figure B-7 Time Step Study Velocity Contour

Figure B-8 Time Step Study Temperature Contour

Through qualitative comparison of these profiles, the discrete phase model becomes time step independent at approximately 5 $x10^{-5}$ seconds which was used for the duration of this research. For the injection properties defined in Section 4.4.4 this time step resulted in a total of approximately 1.5 $x10^{5}$ parcels being tracked through the domain. The advancement of these parcels occupied a large portion of the total simulation time and proved to be very computationally expensive. Careful consideration should be used when selecting an appropriate time step based on the computational resources available.

B.5 Inlet Mass Flow Constituents

Program written in Engineering Equation Solver

```
" Program Calculates The Addition of Water Contributed By Combustion"
Tair1=25
Tair2=470
cp[1]=Cp(Air,T=Tair1)
cp[2]=Cp(Air,T=Tair2)
Cpave=(cp[1]+cp[2])/2
CpMol=CpAve*28.97
MdotAir=1.335
```

```
MoldotAir=MdotAir/28.97
Qin=CpMol*MoldotAir*(Tair2-Tair1)
MolReq=Qin/891000 "891 heat of formation for Methane"
AddH20=MolReq*2
KgAddH20=AddH20*18
Omega=KgAddH20/Mdotair
"H20 Uses O2 From Airflow and H from CH4 in methane , Total mass Flow is the Inlet Air And
Methane"
```

B.6 Geometry Building Program

Program written in "Gambit Journal" language

```
/Ejector Radius and Length
$RE=1.1
$LE=10*$RE
/Mixing Tube Radius and Length
$RMIX=2*$RE
$LMIX=4*$RMIX
/ ***** Select Inlet Type *****
/  OPTION1 (1=Flat Inlet) (2=Bell Mouth Inlet)
$OPTION1=1
/Bell Mouth Radius (m)
$BMRAD=0.0508
/Air Properties
$RHOAIR=0.456
$MDOT=75
$AE=3.14159265*$RE^2
$V1=$MDOT/($RHOAIR*$AE)
$V2=120
/Nozzle Radius and Chamfer Angle
$RN=SQRT( ($AE*$V1) / (3.14159265*$V2) )
$LCAM=($RE-$RN)/TAN(20)
$LES=$LE-$LCAM
/ SLICE ANGLE
$SLICEANGLE=360
/Ejector Wall Thickness
$THICK=12.7E-3
$REOW=$RE+$THICK
$RNOW=$RN+$THICK
/Standoff Length
$Standoff=$RE
/Expansion Region Length In Front of Nozzle
$LZ1=$RNOW/2
/Outlet Plenum Radius and Length
$RPLEN=2*$RMIX
```

```
$LPLEN=3*$RPLEN
/Inlet Plenum Offset and Radius
$LIP1=0.125*$LES
$RIP= 1.5*$RMIX
$RDIFEXIT=(TAN($DIFANGLE)*$DIFLENGTH)+$RMIX
/Outlet Plenum Radius and Length for Diffuser option
$RPLEN2=2*$RDIFEXIT
$LPLEN2=2*$RPLEN2
/ Initial Geometry Build
vertex create "A1" coordinates 0 0 0
vertex create "A2" coordinates 0 $RE 0
vertex create "A3" coordinates 0 $REOW ($LES-$LIP1)
vertex create "A4" coordinates 0 0 $LES
vertex create "A5" coordinates 0 $RE $LES
vertex create "A6" coordinates 0 $REOW $LES
vertex create "A7" coordinates 0 0 $LE
vertex create "A8" coordinates 0 $RN $LE
vertex create "A9" coordinates 0 $RNOW $LE
vertex create "A10" coordinates 0 0 ($LE+$LZ1)
vertex create "A11" coordinates 0 $RNOW ($LE+$LZ1)
/ *** INLET TYPE IF STATEMENT ***
/Standard Inlet Geometry Build
IF COND($OPTION1.EQ.1)
$RA=$RMIX-(0.1*$RMIX)
$RMIXOW=$RMIX+$THICK
$RB=(0.1*$RMIX)+ $RMIXOW
$LC=$RB-$RA
vertex create "A12" coordinates 0 0 ($Standoff+$LE+(2*$LZ1))
vertex create "A13" coordinates 0 $RA ($Standoff+$LE+(2*$LZ1))
vertex create "A14" coordinates 0 $RA ($Standoff+$LE-$LC)
vertex create "A15" coordinates 0 $RA $LES
vertex create "A16" coordinates 0 $RIP $LES
vertex create "A17" coordinates 0 $RIP ($LES-$LIP1)
vertex create "A18" coordinates 0 $RMIX ($Standoff+$LE+(2*$LZ1))
vertex create "A19" coordinates 0 $RMIX ($Standoff+$LE)
vertex create "A20" coordinates 0 $RA ($Standoff+$LE)
vertex create "A21" coordinates 0 $RB ($Standoff+$LE-$LC)
vertex create "A22" coordinates 0 $RB ($Standoff+$LE)
vertex create "A23" coordinates 0 $RMIXOW ($Standoff+$LE)
vertex create "A24" coordinates 0 $RIP ($Standoff+$LE-$LC)
vertex create "A26" coordinates 0 $RMIXOW ($Standoff+$LE+(0.5*$LIP1))
vertex create "A27" coordinates 0 $RIP ($Standoff+$LE+(0.5*$LIP1))
vertex create "A28" coordinates 0 $RB ($Standoff+$LE+(0.5*$LIP1))
ELSE
$RA=$RMIX-(0.1*$RMIX)
$RMIXOW=$RMIX+(2*$BMRAD)
$RB=(0.1*$RMIX)+ $RMIXOW
$LC=($RB-$RA)/2
```

```
vertex create "A12" coordinates 0 0 ($Standoff+$LE+(2*$LZ1))
vertex create "A13" coordinates 0 $RA ($Standoff+$LE+(2*$LZ1))
vertex create "A14" coordinates 0 $RA ($Standoff+$LE-$LC)
vertex create "A15" coordinates 0 $RA $LES
vertex create "A16" coordinates 0 $RIP $LES
vertex create "A17" coordinates 0 $RIP ($LES-$LIP1)
vertex create "A18" coordinates 0 $RMIX ($Standoff+$LE+(2*$LZ1))
vertex create "A19" coordinates 0 $RMIX ($Standoff+$LE+$BMRAD)
vertex create "A20" coordinates 0 $RA ($Standoff+$LE+$BMRAD)
vertex create "A21" coordinates 0 $RB ($Standoff+$LE-$LC)
vertex create "A22" coordinates 0 $RB ($Standoff+$LE+$BMRAD)
vertex create "A23" coordinates 0 $RMIXOW ($Standoff+$LE+$BMRAD)
vertex create "A24" coordinates 0 $RIP ($Standoff+$LE-$LC)
vertex create "A26" coordinates 0 $RMIXOW ($Standoff+$LE+(0.5*$LIP1))
vertex create "A27" coordinates 0 $RIP ($Standoff+$LE+(0.5*$LIP1))
vertex create "A28" coordinates 0 $RB ($Standoff+$LE+(0.5*$LIP1))
vertex create "A29" coordinates 0 ($RMIX+$BMRAD) ($Standoff+$LE)
/ Build the Mixing Tube
vertex create "A30" coordinates 0 0 ($Standoff+$LE+$LMIX)
vertex create "A31" coordinates 0 $RMIX ($Standoff+$LE+$LMIX)
edge create "B38" straight "A18" "A31"
edge create "B40" straight "A30" "A12"
/Build Outlet Plenum
vertex create "A34" coordinates 0 $RPLEN ($Standoff+$LE+$LMIX)
vertex create "A35" coordinates 0 $RPLEN ($Standoff+$LE+$LMIX+$LPLEN)
vertex create "A36" coordinates 0 0 ($Standoff+$LE+$LMIX+$LPLEN)
vertex create "A37" coordinates 0 (0.9*$RMIX) ($Standoff+$LE+$LMIX)
vertex create "A38" coordinates 0 (1.1*$RMIX) ($Standoff+$LE+$LMIX)
vertex create "A39" coordinates 0 (0.9*$RMIX) ($Standoff+$LE+$LMIX+(0.2*$RMIX))
vertex create "A40" coordinates 0 (1.1*$RMIX) ($Standoff+$LE+$LMIX+(0.2*$RMIX))
ENDIF
END
```

B.7 Modified Turbulence Model Program

Program Written in “C+” Language

```
#include "udf.h"
DEFINE_TURBULENT_VISCOSITY(user_mu_t,c,t)
{
double u = C_U(c,t);
double v = C_V(c,t);
double w = C_W(c,t);
double V;
double c_mu = 0.0845;
```

```
double mu_t;
double mu_t_RNG;
double mu_t_MOD;
double mu_free;
double mu_t_2L;
double k = C_K(c,t);
double d = C_D(c,t);
double T = C_T(c,t);
double rho = C_R(c,t);
double gradT;
double gradt0 = C_T_G(c,t)[0];
double gradt1 = C_T_G(c,t)[1];
double gradt2 = C_T_G(c,t)[2];
double TG;
double CT;
double Lu;
double y;
double A;
double Rey;
double Rey_star = 200;
double A_mu = 200;
double Cl_star;
double lam_ep;
double prof = 14;
double prof2 = 0.5;
/* This Section Calculates the Turbulent Viscosity to Mimic RNG */
Cl_star = prof * 0.42 * pow(c_mu,(-3/4));
y = C_WALL_DIST(c,t);
Rey = rho * y * (pow(k,0.5))/ C_MU_L(c,t);
Lu = C_WALL_DIST(c,t) * Cl_star * ( 1 - (exp((-Rey/(A_mu)))));
A =  pow(SQR(0.15*Rey_star),0.5)/ tanh(0.98);
lam_ep = 0.5 * (1 + (tanh((Rey-Rey_star)/(A*prof2))));
mu_free = c_mu*rho*SQR(k)/d;
mu_t_2L = rho*c_mu*Lu*(pow(k,0.5));
mu_t_RNG = (lam_ep*mu_free) + ((1-lam_ep)*mu_t_2L);
/* This Section Applies A Modification Based On The Magnitude Of The Temperature Gradient
*/
gradT = pow( (SQR(gradt0) + SQR(gradt1) + SQR(gradt2)) , 0.5);
TG = 0.31 * gradT * ( (pow(k,1.5)) /d ) / (T);
CT = 1 + ((TG*TG*TG)/0.041);
mu_t_MOD = CT * mu_t_RNG;
/* This Section Fixes Boundary Error ( Reversed Flow On Pressure Boundaries ) */
V = pow((SQR(u) + SQR(v) + SQR(w)),0.5);
if (V < 10)
mu_t = mu_t_RNG + ( (mu_t_MOD-mu_t_RNG) * pow((V/10),4) );
else
{
mu_t=mu_t_MOD;
```

```
}
/* This Section Eliminates The Turbulent Viscosity Spike At The Nozzle Exit */
if (gradT > 50000)
mu_t = mu_t_RNG + ( (mu_t_MOD-mu_t_RNG) * pow((50000/gradT),6) );
else
{
mu_t=mu_t_MOD;
}
/* This Section Limits Turbulent Viscosity For Divergence Issues */
if (mu_t > 0.4)
mu_t=0.4;
else
{
mu_t=mu_t;
}
return mu_t;
}
```

B.8 Spray Flux Contour Program

Program written In “FORTRAN 90” language

```
PROGRAM SprayProgram
REAL :: Increment,Diameter
REAL :: Grid(100,100)
REAL :: x,y,mdot,Xpos,Ypos,r,negXpos,negYpos
INTEGER :: ERRORCODE,nx,ny,i,j,timesteps
800 FORMAT(ES11.4E2,ES11.4E2,ES11.4E2)
900 FORMAT(F10.5,'   ',F10.5,'',F10.5)
OPEN(1, FILE="sample.txt")
OPEN(2, FILE="Results.DAT")
Increment=0.009
i=0
j=0
timesteps=40
Diameter=0.1524
READ (1,800,iostat=errorcode) x,y,mdot
DO WHILE ( errorcode .GE. 0 )
nx=ANINT((x/Increment)-0.5)
ny=ANINT((y/Increment)-0.5)
Grid(nx+1,ny+1)= Grid(nx+1,ny+1) + mdot
ny=0
nx=0
mdot=0
READ (1,800,iostat=errorcode) x,y,mdot
END DO
```

```
Grid(:,:) = Grid(:,:)/((Increment**2)*Timesteps)
DO WHILE (i<100)
i=i+1
DO WHILE(j<100)
j=j+1
Xpos=((i-1)*INCREMENT)+(INCREMENT/2)
Ypos=((j-1)*INCREMENT)+(INCREMENT/2)
 negXpos=-1*Xpos
negYpos=-1*Ypos
r=SQRT((Xpos**2)+(Ypos**2))
IF (ABS(r) < (Diameter/2)) THEN
WRITE(2,900) Xpos, Ypos, GRID(i,j)
WRITE(2,900) negXpos, Ypos, GRID(i,j)
WRITE(2,900) Xpos, negYpos, GRID(i,j)
WRITE(2,900) negXpos, negYpos, GRID(i,j)
ENDIF
Xpos=0
 Ypos=0
END DO
j=0
END DO
END
```

B.9 1D Analytical Ejector Solution

Program written in Engineering Equation Solver

```
{ Known Parameters }
K=1.4
T_1= 500 [C]
T_02 = 25 [C]
V_1 =  160 [m/s]
M_1= 1.3 [kg/s]
P_02 = 101.325 [KPa]
P_3 = 101.325 [KPa]
P_2 = P_1
A_2=A_3-A_1
AR=A_3/A_1
PumpingRatio=M_3/M_1
KELoss= (M_3 * ((V_3^2)/2)) - (M_1* ((V_1^2)/2)) - (M_2 * ((V_2^2)/2))
{Densities}
rho_i=Density(Air,T=T_i,P=P_i)
rho_1=Density(Air,T=T_1,P=P_1)
rho_2=Density(Air,T=T_2,P=P_2)
rho_3=Density(Air,T=T_3,P=P_3)
{Mass Flow}
```

```
M_1= rho_1 * A_1 * V_1
M_2= rho_2 * A_2 * V_2
M_3= rho_3 * A_3 * V_3
{Pressure2}
P_02 = P_2 + ((rho_2 * (V_2^2))/2000)
{StagTempEquation}
(P_02/P_2) = ( (T_02 +273) / (T_2+273) ) ^ (K/(K-1))
{Conservation Mass}
M_1 + M_2 = M_3
{Conservation Momentum}
(P_1*1000 * A_3) - (P_3 * 1000*A_3) = (M_3 * V_3) - (M_1 * V_1) - (M_2 * V_2)
{Enthalpy}
H_1=Enthalpy(Air,T=T_1)
H_2=Enthalpy(Air,T=T_2)
H_3=Enthalpy(Air,T=T_3)
{Conservation Energy}
((H_1+((V_1^2)/2000))*M_1) + ((H_2+((V_2^2)/2000))*M_2) = ((H_3+((V_3^2)/2000))*M_3)
{Bernoulli for BackPressure}
P_i + (0.5*rho_i*(V_i^2))/1000 = P_1 + (0.5*rho_1*((V_1^2)-(V_i^2)))/1000
A_i = A_1*2
V_i = (rho_1*A_1*V_1)/(rho_i*A_i)
T_i +(V_i^2)/2000*Cp(Air,T=T_i)  = T_1 + (V_1^2)/2000*Cp(Air,T=T_1)
CBP=((P_i-101.325)*1000)/(0.5*0.456*(117^2))
```